

Cover Page



Universiteit Leiden



The handle <http://hdl.handle.net/1887/74441> holds various files of this Leiden University dissertation.

**Author:** Hoang, D.N.

**Title:** Cosmic particle acceleration by shocks and turbulence in merging galaxy clusters

**Issue Date:** 2019-06-26

# **Cosmic particle acceleration by shocks and turbulence in merging galaxy clusters**

Duy N. Hoang

©2019 Duy N. Hoang

ISBN:

Cover: (Background) A wide-field radio image of the Sausage cluster as observed with the Low Frequency Array (LOFAR) with High-Band Antenna operating at frequency of 143 MHz with a bandwidth of 64 MHz. (Foreground): An enlarged LOFAR radio image of the Sausage cluster on top of a Chandra X-ray image.

# **Cosmic particle acceleration by shocks and turbulence in merging galaxy clusters**

Proefschrift

ter verkrijging van  
de graad van Doctor aan de Universiteit Leiden,  
op gezag van Rector Magnificus prof. mr. C. J. J. M. Stolker,  
volgens besluit van het College voor Promoties  
te verdedigen op woensdag 26 juni 2019  
klokke 13:45 uur

door

Duy N. Hoang

geboren te Vietnam  
in 1981

Promotiecommissie

Promotor:	Prof. Dr. Huub Röttgering	Leiden University
Promotoren:	Dr. Timothy Shimwell	Netherlands Institute for Radio Astronomy/ Leiden University
	Dr. Reinout van Weeren	Leiden University
Overige leden:	Prof. Dr. Henk Hoekstra	Leiden University
	Prof. Dr. Jelle Kaastra	Netherlands Institute of Space Science/ Leiden University
	Prof. Dr. George Miley	Leiden University
	Prof. Dr. Paul Ho	Academia Sinica
	Dr. Huib Intema	Leiden University/ Curtin Institute of Radio Astronomy
	Dr. Hiroki Akamatsu	Netherlands Institute of Space Science
	Dr. Aurora Simionescu	Netherlands Institute of Space Science

For my parents!



# Contents

1	Introduction	1
1.1	Large-scale structure in the Universe . . . . .	1
1.2	Galaxy clusters . . . . .	2
1.3	Extended radio emission in galaxy clusters . . . . .	4
1.4	Advances in observations of the ICM . . . . .	9
1.5	This thesis . . . . .	11
1.6	Future prospects . . . . .	14
2	LOFAR observations of CIZA J2242.8+5301	15
2.1	Introduction . . . . .	16
2.2	The galaxy cluster CIZA J2242.8+5301 . . . . .	17
2.3	Observations and data reduction . . . . .	19
2.3.1	LOFAR HBA data . . . . .	19
2.3.2	GMRT, WSRT radio, Suzaku and Chandra X-ray data	24
2.3.3	Imaging and flux scale of radio intensity images . . . . .	24
2.3.4	Spectral index maps . . . . .	25
2.4	Results . . . . .	28
2.4.1	Northern relic . . . . .	29
2.4.2	Southern relic . . . . .	34
2.4.3	Eastern relics . . . . .	35
2.4.4	Radio halo . . . . .	36
2.4.5	Tailed radio galaxies . . . . .	38
2.5	Discussion . . . . .	39
2.5.1	Radio spectrum derived Mach numbers . . . . .	40
2.5.2	Particle acceleration efficiency . . . . .	44
2.5.3	The radio halo . . . . .	46
2.5.4	A newly detected eastern shock wave? . . . . .	50
2.6	Conclusions . . . . .	52



Appendices . . . . .	54
A    Integrated fluxes for the radio relics and halo . . . . .	54
B    Spectral index error maps . . . . .	54
C    Eastern region of RS . . . . .	54
3 Radio observations of Abell 1240 . . . . .	57
3.1 Introduction . . . . .	58
3.2 Observations and data reduction . . . . .	61
3.2.1 LOFAR 143 MHz . . . . .	61
3.2.2 GMRT 612 MHz . . . . .	63
3.2.3 VLA 3 GHz . . . . .	64
3.2.4 Continuum imaging . . . . .	65
3.2.5 Spectral index measurements . . . . .	65
3.2.6 Polarization measurements . . . . .	67
3.2.7 Chandra X-ray data . . . . .	68
3.3 Results . . . . .	68
3.3.1 The double radio relics . . . . .	69
3.3.2 A connection with Abell 1237 . . . . .	75
3.4 Discussion . . . . .	76
3.4.1 Radio relics . . . . .	76
3.4.2 Radio halo and cluster mass . . . . .	84
3.5 Conclusions . . . . .	89
4 Radio observations of Abell 520 . . . . .	93
4.1 Introduction . . . . .	95
4.2 The galaxy cluster Abell 520 . . . . .	96
4.3 Observations and data reduction . . . . .	97
4.3.1 LOFAR 145 MHz . . . . .	97
4.3.2 GMRT 323 MHz . . . . .	99
4.3.3 VLA 1.5 GHz . . . . .	99
4.3.4 Continuum imaging and spectrum mapping . . . . .	100
4.3.5 Chandra . . . . .	102
4.4 Results . . . . .	102
4.4.1 The radio halo . . . . .	102
4.4.2 The SW region of the radio halo . . . . .	106
4.4.3 The NE region of the radio halo . . . . .	106
4.5 Discussion . . . . .	110
4.5.1 The radio halo . . . . .	110
4.5.2 The SW radio edge . . . . .	113
4.5.3 The NE radio edge . . . . .	116

4.6	Conclusions . . . . .	117
5	Characterizing the radio emission from Abell 2146 . . . . .	121
5.1	Introduction . . . . .	122
5.2	The galaxy cluster Abell 2146 . . . . .	124
5.3	Observations and data reduction . . . . .	125
5.3.1	LOFAR 144 MHz . . . . .	125
5.3.2	GMRT 238 and 612 MHz . . . . .	127
5.3.3	VLA 1.5 GHz . . . . .	127
5.3.4	Spectral measurements . . . . .	128
5.4	Results and discussion . . . . .	128
5.4.1	The radio galaxies . . . . .	128
5.4.2	The NW extended emission . . . . .	131
5.4.3	The radio bridge . . . . .	135
5.4.4	The SE extended emission . . . . .	136
5.5	Conclusions . . . . .	139
	Bibliography . . . . .	142
	Nederlandse samenvatting . . . . .	153
	Curriculum Vitae . . . . .	159
	List of publications . . . . .	161
	Acknowledgements . . . . .	163



# 1 | Introduction

## 1.1 Large-scale structure in the Universe

Some of the most important observations in modern astronomy include those that revealed the accelerating expansion of the Universe, the Cosmic Microwave Background (CMB) radiation, the abundance of light elements (i.e. H, He, Li, and their isotopes), and the structure of the distribution of baryonic matter on large scales. These observations are currently best explained in the framework of the standard model of ‘Big Bang’ cosmology, or the  $\Lambda$ CDM (Lambda Cold Dark Matter) model. In this  $\Lambda$ CDM model, the Universe has been expanding after an explosion (known as the Big Bang)  $13.80 \pm 0.02$  billion years ago (e.g. Planck Collaboration et al. 2016, see Fig. 1.1). Shortly after the Big Bang ( $\sim 10^{-36}$  s), the Universe went through a period of rapid expansion, commonly known as cosmic inflation (Guth 1981). During inflation ( $\sim 10^{-32}$  s), the Universe is believed to have exponentially expanded by a factor of more than  $10^{26}$  (e.g. Kolb et al. 1991). Since inflation the Universe has continued to expand, albeit at a slower rate.

In the  $\Lambda$ CDM model, the Universe consists of dark energy, dark matter, and baryonic matter. Dark energy and dark matter account for most of the total matter-energy content in the Universe with 68.5% and 26.5%, respectively. Baryonic matter that is visible to our telescopes contributes only 5.0% to the total matter-energy budget of the Universe (e.g. Planck Collaboration et al. 2018).

Precise CMB observations have revealed that the Universe on large scales is extremely homogeneous. The CMB radiation has a spectrum consistent with that of a black body at a temperature of  $T_{\text{CMB}} = 2.725$  K (e.g. Fixsen et al. 2009). However, on smaller scales there are tiny fluctuations (i.e.  $\sim 1$  part per  $10^5$ ) in the CMB temperature (e.g. Smoot et al. 1992). These tiny variations in the temperature are thought to correspond to the quantum fluctuations of matter density that are present immediately after

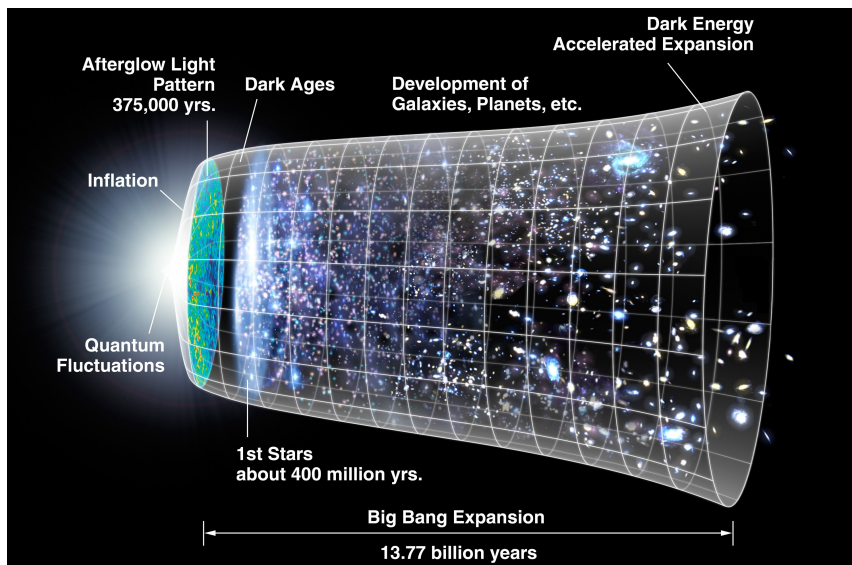


Figure 1.1: An artist impression of the time-line of the Universe (Image credit: NASA/WMAP Science Team)

the Big Bang. These are the primordial fluctuations that are the seeds for structure formation, as towards the regions of slightly higher matter density, dark matter hierarchically collapses under its own gravity and forms haloes of cold dark matter. These high dense regions accrete more matter and eventually in these regions the structures such as clouds of gas, stars, galaxies, and clusters of galaxies form.

## 1.2 Galaxy clusters

Galaxy clusters are the largest gravitationally bound structure in the Universe. They consist of hundreds to thousands of galaxies over volumes of up to  $\sim 100 \text{ Mpc}^3$  (e.g. see Fig. 1.2). The total mass of galaxy clusters ranges from between  $\sim 10^{14}$  and  $\sim 10^{15}$  solar masses. Most of the matter in galaxy clusters is dark matter ( $\sim 80\%$  of the total mass) which appears to only interact with baryonic matter ( $\sim 20\%$ ) through gravitational force. The nature of dark matter is still poorly understood, but it is thought to consist of an as yet undiscovered subatomic particle (e.g. weakly-interacting massive particles, gravitationally-interacting massive particles). Baryonic matter in galaxy clusters is found mostly in the form of super hot plasma ( $\sim 16\%$ ) in

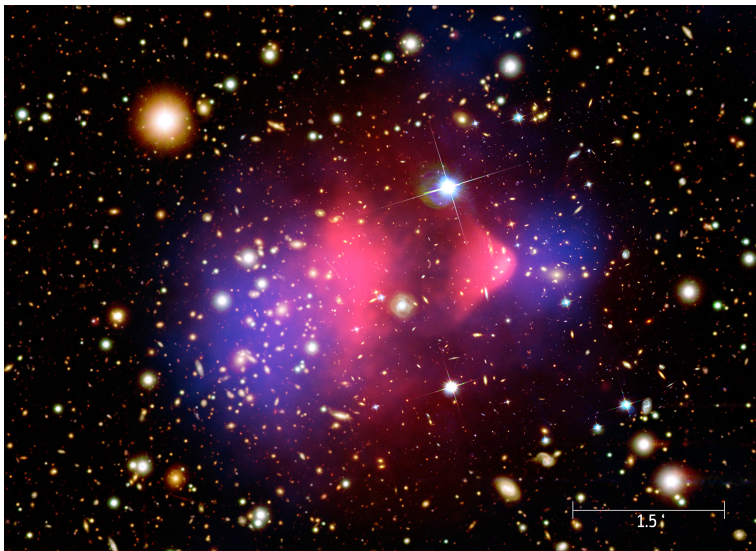


Figure 1.2: The Bullet cluster. An optical HST (Hubble Space Telescope) composite image of the Bullet cluster overlaid with the X-ray emission (pink, Chandra) and the mass distribution derived from weak-lensing data (blue). (Image credit: NASA/CXC/M. Weiss)

the intra-cluster medium (ICM) with a much smaller fraction in stars, cold gas and dust ( $\sim 4\%$ ). Observations have shown that hot plasma in the ICM has a low density ( $\sim 10^{-3}\text{cm}^{-3}$ ) and very high temperature ( $\sim 10^7\text{K}$ ).

In the hierarchical structure formation framework, galaxy clusters grow through a sequence of mergers of smaller clusters/groups (e.g. Sarazin 2002) or by the continuous accretion of matter along intergalactic filaments (e.g. Giovannini et al. 2010). Mergers of massive clusters are the most energetic events in the Universe since the Big Bang, and release up to  $\sim 10^{64}$  ergs into the ICM on time scales of a few billion years. This energy heats up the ICM plasma to sufficiently high temperatures ( $\sim 10^7\text{K}$ ) for it to emit X-ray radiation. The mergers also generate shock waves and turbulence in the ICM and this leads to the (re-)acceleration of particles in the ICM to relativistic speeds.

The evolution of cluster galaxies is strongly affected by their interaction with the ICM and other galaxies in the clusters (e.g. morphological transformation, star formation rate). Galaxies that are moving in the ICM experience tidal forces (namely galaxy harassment; Moore et al. 1996) which are caused by the gravitational potential of the clusters in which they reside

or by encounters with other high-speed galaxies. As shown in simulations by Moore et al. (1998), tidal forces distort the morphology of small disc galaxies which later transform to spheroidal galaxies. The morphological transformation from spiral galaxies to elliptical and S0 ones might also occur through a process called galaxy strangulation, in which the interstellar medium (ISM) of the in-falling galaxies are removed by the tidal forces generated by the cluster potential well (Larson et al. 1980). The star formation rate is often estimated through the observed intensity of the H-alpha and neutral hydrogen spectral lines that are emitted during the formation of stars. Dense gas environments of the ICM seem to decrease the rate of star formation in cluster galaxies as compared to that in the field counterparts of the same redshift (e.g. Dressler 1980; Goto et al. 2003; Balogh et al. 2002; Kodama et al. 2004; Cayatte et al. 1990). This decrease might be due to the ram pressure stripping of the ISM gas from the host galaxies (e.g. Gunn & Gott, J. Richard 1972; Fumagalli et al. 2014; Gavazzi et al. 2001; Oosterloo & van Gorkom 2005). This effect has been indicated through N-body/hydrodynamical simulations (e.g. Steinhauser et al. 2012). In the simulations, strong ram pressure in high particle density number environments can pull out a significant amount of gas from the host galaxies resulting in fewer stars being formed. However, weak ram pressure can compress the gas in the ISM and increase the rate of star formation. The compression of the ISM in rich-gas galaxies can also occur by the passage of shock waves induced by cluster mergers, leading to the formation of dense clouds and triggering the formation of stars (e.g. Stroe et al. 2015a).

### 1.3 Extended radio emission in galaxy clusters

Extensive observational campaigns have now detected many extended radio sources in the central and peripheral regions of galaxy clusters (e.g. see Govoni & Feretti 2004; Feretti et al. 2012; Brunetti & Jones 2014, for recent reviews). These extended sources are not obviously associated with individual cluster galaxies, but are related to the large-scale non-thermal components (i.e. relativistic particles and magnetic fields) in the ICM. Under the assumption of equipartition, the magnetic field strength in the ICM is estimated to be  $\sim 1\mu\text{G}$ . However, the strength and structure of magnetic fields in galaxy clusters have not been fully understood. Currently cluster magnetic fields can be studied with (i) radio observations and equipartition assumptions (e.g. Miley 1980; Thierbach et al. 2003), (ii) a combination of radio (i.e. synchrotron emission) and hard X-ray (i.e. Inverse Compton

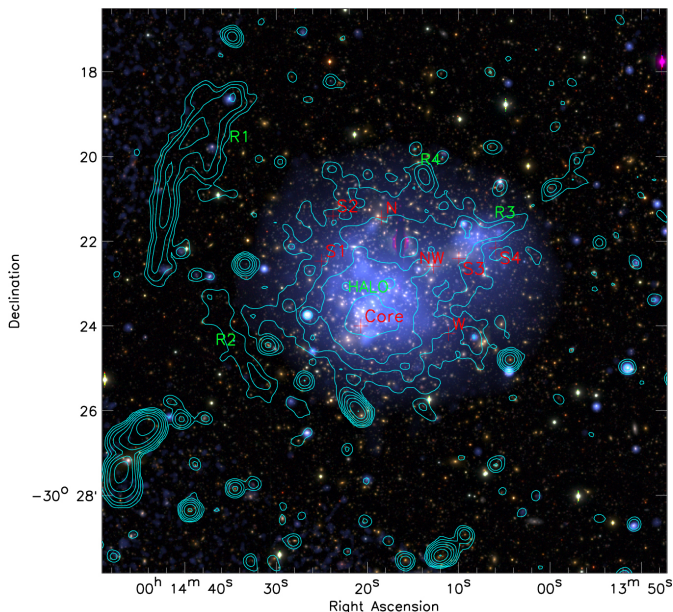


Figure 1.3: Radio contours overlaid on the optical and X-ray images of merging galaxy cluster Abell 2744 (Pearce et al. 2017). Radio sources (including the halo and relic R1) are labelled (Image credit: C. J. J. Pearce)

emission) observations (e.g. Finoguenov et al. 2010), or (iii) Faraday rotation of polarized radio sources that reside within or behind galaxy clusters (e.g. Clarke et al. 2001; Brentjens & de Bruyn 2005).

The extended synchrotron radio sources are observed to have low surface brightness ( $\sim 1\mu\text{Jy arcsec}^{-2}$  at 1.4 GHz) and steep spectra<sup>1</sup> ( $\alpha \lesssim -1$ ). Depending on their properties (i.e. morphology, location with respect to the cluster centre, polarization, spectrum), the extended sources have been classified as radio haloes, mini-haloes or relics.

## Radio haloes

Radio haloes are huge, usually diffuse ( $\sim \text{Mpc}$ ) sources that are observed in the central regions of merging galaxy clusters (see, e.g., Fig. 1.3). These synchrotron radio sources have steep ( $\alpha \lesssim -1$ ) spectra and are unpolarized. Radio haloes are mostly found in galaxy clusters that are massive and have a disturbed X-ray morphology. The morphology of radio haloes are typically

---

<sup>1</sup> $S \propto \nu^\alpha$



similar to that of the cluster X-ray emission. The surface brightness in the radio and X-ray bands are spatially well correlated (e.g. Govoni et al. 2001a,b; Feretti et al. 2001; Venturi et al. 2013; Rajpurohit et al. 2018), implying a relationship between non-thermal and thermal components in the ICM. Furthermore, the power of radio haloes is proportional to the X-ray luminosity and temperature, and mass of their host clusters (e.g. Liang et al. 2000; Cassano et al. 2006, 2013).

Due to the short radiative lifetime ( $\ll 10^8$  years) of the relativistic electrons in the  $\mu\text{G}$  magnetized ICM, the Mpc size of radio haloes implies that the radio emitting cosmic ray electrons in haloes must be locally (re-)accelerated (Jaffe 1977). The exact mechanism that governs the acceleration of relativistic particles in radio haloes has not been fully understood. Currently, the main models for the formation of radio haloes are:

- the primary model that proposes that the generation of cosmic ray electrons in radio haloes happens through Fermi-II turbulent re-acceleration during cluster mergers (e.g. Brunetti et al. 2001; Petrosian 2001; Fujita et al. 2003; Cassano & Brunetti 2005; Brunetti & Lazarian 2007, 2016; Pinzke et al. 2017), and
- the secondary model that proposes that the relativistic electrons in radio haloes are the secondary products of the hadronic collisions between cosmic ray protons and thermal protons in the ICM (e.g. Dennison 1980; Blasi & Colafrancesco 1999; Dolag & Enßlin 2000; Miniati et al. 2001; Pfrommer & Enßlin 2004; Pfrommer 2008; Keshet & Loeb 2010; Enßlin et al. 2011). The secondary model predicted that  $\gamma$ -rays should also be generated as one of the products of the hadronic collisions. However, upper limits for the  $\gamma$ -ray flux set by the Fermi-LAT observations challenge the validity of the secondary hadronic model for the emission mechanism in radio haloes (e.g. Jeltama & Profumo 2011; Brunetti et al. 2012; Zandanel et al. 2014; Ackermann et al. 2010, 2016).

### Mini-haloes

Similarly to radio haloes, mini-haloes are generally extended, steep spectrum, unpolarized sources located in the central regions of clusters. However, mini-haloes are smaller in size ( $\lesssim 500$  kpc) and have significantly higher surface brightness ( $\sim 50$  times) than radio haloes (e.g. Govoni & Feretti 2004; Cassano et al. 2008). Mini-haloes are typically found in non-merging galaxy clusters that host cool cores and a powerful radio galaxy

(e.g. brightest cluster galaxy; BCG) in their centre. The origin of mini-haloes remains uncertain. In the same way as for radio haloes, it has been proposed that the radio emitting cosmic ray electrons in mini-haloes originate from (i) a pre-existing population of relativistic electrons (e.g. from the central BCGs) that are re-accelerated through Fermi-like processes by magnetohydrodynamical turbulence (e.g. due to the cooling flow of inward gas in the core region; Gitti et al. 2002) or (ii) the secondary particles that are generated via inelastic hadronic collisions between cosmic ray protons and thermal protons in the core region (e.g. Miniati et al. 2001; Keshet & Loeb 2010; Zandanel et al. 2014).

### Radio relics

Radio relics are extended ( $\sim$  Mpc), elongated, steep spectrum sources that are usually observed in the peripheral regions of galaxy clusters (see, e.g., Fig. 1.3). Some radio relics are observed to be highly polarized at high frequencies (i.e. up to  $\sim 70\%$ ) and the magnetic field vectors are parallel to the major axes of the relics (e.g. van Weeren et al. 2010; Bonafede et al. 2009; Kale et al. 2012). Radio relics are generally thought to be associated with shock waves that are generated by cluster mergers or gas accretion from intergalactic filaments (e.g. Enßlin et al. 1998; Brown & Rudnick 2011). There is observational evidence supporting the connection between merger shocks and radio relics in clusters: (i) the elongated morphology of radio relics is co-spatial with X-ray detected shocks, (ii) the steepening of the radio spectral index in the region behind shocks due to synchrotron and inverse-Compton energy losses, and (iii) the strongly polarized emission detected in some relics. The Mach numbers of merger shocks derived from X-ray data are low, typically  $\mathcal{M} \lesssim 3$ . However, the efficiency in which particles are accelerated by shocks is still unknown, and these low Mach number shocks may be incapable of producing the bright radio relics. A possible solution is that shocks re-accelerate a pre-existing population of mildly relativistic particles, instead of those from the thermal pool (e.g. Markevitch et al. 2005; Kang & Ryu 2011; Kang et al. 2012).

### Open questions

Shocks and turbulence in the ICM, induced by cluster mergers, present a unique environment (i.e. large scale, low particle number density, weak magnetic fields, low-Mach-number shocks, high energy) for studies of particle acceleration at cosmic scales. Despite the ongoing improvement in our

understanding of the extended radio sources in galaxy clusters, some of the main questions in the field remain to be answered, including:

- What is the origin of the cosmic rays in extended radio sources of galaxy clusters? How are the cosmic rays accelerated?
- How is the magnetic field in the ICM generated/amplified? What is the strength and topology of the ICM magnetic field? How do magnetic fields in the ICM evolve over cosmic time?

Radio haloes and relics are more luminous at low frequencies due to their steep spectrum ( $\alpha \lesssim -1$ ). Therefore, observations to study the properties of these non-thermal components (i.e. relativistic particles and magnetic field) are best conducted at low frequencies. In addition, accurate spectral and polarimetric properties of extended emission are crucial to understand the particle acceleration mechanisms in these sources.

Wide-frequency integrated spectra of radio haloes and relics provide clues on the origin of cosmic ray electrons in these sources. For relics, the simple diffusive shock acceleration model predicts single-power-law spectra if the cosmic ray electrons are accelerated directly from the thermal pool in the ICM. However, the detection of curve/break spectra with wide frequency observations implies that the cosmic ray electrons in relics might be re-accelerated by the passage of shock waves from a population of mildly relativistic electrons, that are fossils of active galactic nuclei activities or previous cluster mergers. For radio haloes, the primary and secondary models can also be differentiated using multi-frequency observations as the former model predicts curve integrated spectra for haloes, while the spectra of radio haloes in the latter model are single power law functions.

Additionally, the spatial distribution of spectral energy of the extended radio sources is a helpful tool to understand the emission mechanisms in radio haloes and relics. For example, the spectral gradient across the width of radio relics is one of the key observables to associate them with the shocks detected by X-ray observations (e.g. van Weeren et al. 2010). The evolution of magnetic field strength in radio relics can also be studied using the high-resolution spectral gradients across the relics (e.g. Donnert et al. 2016).

Hence, whilst radio haloes and relics are best discovered and morphologically characterized at low frequencies with high angular resolutions, radio observations at a wide range of frequencies and/or polarizations are also required to understand the physical mechanisms of their formation.

## 1.4 Advances in observations of the ICM

Our detailed understanding of galaxy clusters through observations of thermal plasma in the ICM has been significantly improved during the last decades, thanks to the advancements in X-ray telescopes. Physical processes in plasma physics such as diffusive shock acceleration, turbulence and cooling flows in the extreme hot plasma of the ICM have been studied in detail with recent X-ray missions, e.g. Chandra X-ray Observatory (CXO), the European Space Agency's (ESA) X-ray Multi-Mirror Mission (XMM-Newton), Suzaku (ASTRO-EII) and ROSAT. The developments are expected to continue with new state-of-the-art X-ray satellites. eROSITA is scheduled for launch in 2019; Arcus is expected to be in orbit in 2023; the International X-ray Observatory (IXO) is planned to be launched in 2021; the Advanced Telescope for High Energy Astrophysics (ATHENA) is scheduled for launch in the early 2030s.

Chandra orbits at altitudes of up to 130,000 km above the Earth's surface and contains the Advanced CCD Imaging Spectrometer (ACIS) and the High Resolution Camera (HRC). Chandra was designed to observe the X-ray emission from extreme hot plasma in supernova, active galactic nuclei (AGN) and clusters of galaxies. It can resolve structure of extended sources with a resolution of 0.5 arc sec and is sensitive to X-rays in the medium energy range from 0.1 to 10 keV (e.g. 1 keV corresponds to  $11.6 \times 10^6$  K). The Suzaku satellite orbiting Earth at an altitude of 500 km holds soft and hard X-ray telescopes. It collects photons across a wide energy range from 0.3 up to 600 keV. The main scientific aims of Suzaku were to study hot plasma in galaxy clusters and AGNs. Suzaku ended its mission in 2015 after 10 years of scientific operation.

In addition to the thermal plasma in the ICM, galaxy clusters also host large-scale non-thermal components (i.e. relativistic cosmic rays and magnetic fields). Studies of the non-thermal emission are often carried out with radio observations at high frequencies ( $\gtrsim 1.4$  GHz). However, in the last few decades, there has been significant movement towards the low-frequency regime. For instance, the forthcoming Square Kilometre Array (SKA; Schilizzi 2005) will operate at a frequency range from 50 MHz to 14 GHz. The total collecting area of SKA will be about one square kilometre once it is complete in  $\sim 2020$ . A number of pathfinder radio telescopes have already been constructed, including the Australian Square Kilometre Array Pathfinder (ASKAP; Johnston 2007) working at frequencies from 700 MHz to 1.8 GHz (Johnston et al. 2007) and the Karoo Array Telescope

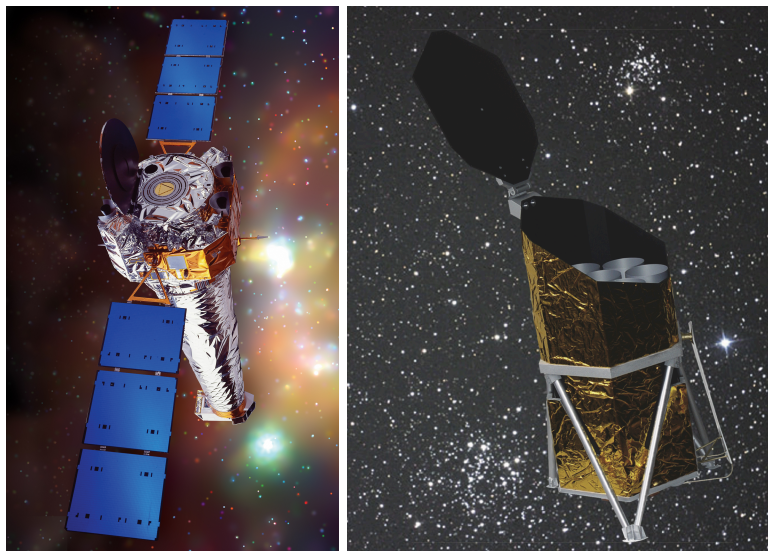


Figure 1.4: Artist's impression of X-ray satellites Chandra (left) and eRosita (right). (Image credit: NASA/CXC/NGST; MPE)

operating at 1 - 10 GHz band (MeerKAT). Some radio interferometers that are specifically designed for low frequencies are the Long Wavelength Array (LWA; Taylor 2006), the Murchison Wide-field Array (MWA; Lonsdale et al. 2009), the LOw Frequency Array (LOFAR; Haarlem et al. 2013), and the Giant Metrewave Radio Telescope (GMRT; Swarup et al. 1991).

LOFAR (Fig. 1.5) is a new-generation radio telescope operating at low frequencies between 10 and 240 MHz. LOFAR exploits the novel phased-array technique in which the antenna primary beam is formed electronically, instead of mechanically steering the antennas or the detector. LOFAR consists of stations located in the Netherlands and across a number of other European countries. Each station is made of a number of dipoles which operate at 10 – 90 MHz for Low Band Array (LBA) and 110 – 240 MHz for High Band Array (HBA). There are currently 38 Dutch (core and remote) stations extending up to 80 km and 13 international stations in other European countries extending up to 1200 km. LOFAR observations with the full Dutch stations resolve extended sources to a few arc sec and a few tens of arc sec with HBA and LBA, respectively. Additional international stations provides sub-arc sec resolution for both HBA and LBA.

Significant sensitive observations in the low frequency radio regime would deepen our understanding of the non-thermal emission in galaxy



Figure 1.5: The layout of LOFAR stations across European countries (left) and its core stations (right) near Exloo, Netherlands. (Image credit: LOFAR/ASTRON)

clusters. However, there are technological challenges relating to data reduction. During the calibration of the interferometric data, additional effects including distortions of the signals relating to ionosphere or instruments need to be taken into account. The distortions delay the signals propagating towards antennas and can result in errors in the position or morphology of the observed sources. Moreover, since the field of view at low frequencies is larger than that at high frequencies, a simple correction for the entire field of view as done for high-frequency radio data is not sufficient. Therefore, new techniques have been developed. The common technique to correct for instrumental effects on small fields of view is self-calibration (Pearson & Readhead 1984). For large fields of view, multiple corrections across the fields of view are necessary, especially at low frequencies where the ionosphere has greater effects on the signals from different directions of the sky. Recent advanced techniques being developed for calibrating low-frequency interferometric data include field-based calibration (Cotton et al. 2004), Source Peeling and Atmospheric Modeling (SPAM; Intema et al. 2009, 2017), SAGECal (Yatawatta et al. 2013; Kazemi et al. 2011), and facet calibration (van Weeren et al. 2016a; Williams et al. 2016). In addition, imaging techniques have also been developed to account for geometrical effects for the wide-field images, including w-projection (Cornwell et al. 2008) and A-projection (Bhatnagar et al. 2008).

## 1.5 This thesis

The aims of this thesis are (i) to characterize the properties of radio haloes and relics in merging galaxy clusters, (ii) to better understand the particle acceleration mechanisms in these sources, and (iii) to obtain a detailed

picture of the dynamical states of their host galaxy clusters. To minimize the complications imposed by projection effects, the galaxy clusters studied in this thesis are all undergoing mergers that are occurring on/close to the plane of the sky. These clusters are CIZA J2242.8+5301 (namely the ‘Sausage’ cluster), Abell 1240, Abell 520, and Abell 2146.

In Chapter 2, new LOFAR observations of the prominent Sausage cluster ( $z = 0.192$ ) at 145 MHz are presented. The LOFAR data were combined with the existing multi-frequency radio data from GMRT, Westerbork Synthesis Radio Telescope (WSRT) and Very Large Array (VLA) to study the spectral properties of the extended radio sources (i.e. radio halo and relics) in the cluster. In addition, archival Chandra and Suzaku X-ray data were also used to study the relation between non-thermal and thermal components in the ICM. This study reveals that (i) the shape and spectral properties of the northern and southern relics are consistent with the picture that the relics are associated with the X-ray detected shocks, which is in line with previous studies (van Weeren et al. 2010; Stroe et al. 2013); (ii) the shock Mach numbers derived from the radio data for the relics are consistent with those derived from X-ray data in literature (Akamatsu et al. 2015), supporting the shock (re-)acceleration scenario of the relics; (iii) the radio surface brightness in the northern relic can be explained by the diffusive shock re-acceleration of fossil electrons in the ICM, however the possibility of direct acceleration of thermal electrons cannot be ruled out due to the sensitivity of the current data; (iv) the spectrum of the radio halo in the Sausage cluster remains a straight power law in the region between the northern and southern relics ( $\sim 1 \text{ Mpc}^2$ ), implying a large region of turbulence induced by the on-going merger.

In Chapter 3, a study of the galaxy cluster Abell 1240 ( $z = 0.1948$ ) using multi-frequency radio observations (LOFAR at 144 MHz, GMRT at 612 MHz and VLA, at 3 GHz) is presented. Abell 1240 hosts double radio relics which are thought to trace merger shocks on opposite sides of the cluster centre. This study confirms that the spectral index of the relic emission steepens towards the cluster centre and that the electric field vectors of the polarized emission in the relics are roughly perpendicular to their major axes, in agreement with the findings of Bonafede et al. (2009). The spectral and polarization properties of the relics are consistent with the scenario that the radio-emitting particles are (re-)accelerated by shocks, however there are only hints of such shocks in Chandra X-ray observations.

In Chapter 4, the particle acceleration mechanisms associated with the formation of the extended radio emission in merging galaxy cluster Abell

520 ( $z = 0.201$ ) are discussed using multi-frequency radio observations (LOFAR at 145 MHz, GMRT at 323 MHz, and VLA at 1.5 GHz). The SW region of the extended radio emission roughly follows an X-ray bow shock and is likely to be related to it. Also there is a steepening of the radio spectral index behind the shock. This implies that the extended radio emission could be a superposition of a radio halo in the centre and a relic in the SW. Diffusive shock (re-)acceleration could be the mechanism by which cosmic ray electrons gain their energy at the shock. Since no extended radio emission is found in front of the bow shock, as predicted by the adiabatic shock compression model, the acceleration mechanism where the magnetic field is compressed by the shock is unlikely in this case.

In Chapter 5, extended radio emission in the merging galaxy cluster Abell 2146 ( $z = 0.232$ ) is discussed using new LOFAR 144 MHz and archival VLA 1.5 GHz data. The observations confirm the existence of the extended radio emission in the SE and NW regions of the cluster, behind X-ray detected shocks. A bridge of faint emission connecting the SE and NW emission is detected with the LOFAR 144 MHz observations, but it is not apparent in the VLA 1.5 GHz images. There is a spectral steepening in the NW extended emission towards the cluster centre. The spectral index in the outer region of the NW emission is flatter than (or inconsistent with) the value predicted by the diffusive shock acceleration model in the case where the relativistic electrons in the NW extended emission are accelerated by the NW shock. The mismatch could be explained if the shock re-accelerates a population of pre-existing fossil electrons rather than those from the thermal pool. The edge of the SE radio emission roughly follows the SE bow shock, implying a possible connection between the two. Assuming diffusive shock acceleration, this shock-radio emission connection is supported by the agreement between the radio and X-ray derived Mach numbers for the SE shock. However, it is still unclear if the SE emission is a single radio halo or a superposition of a halo and a relic. In both cases, the power for the radio halo is close to the value expected for a cluster mass of Abell 2146. Finally, the extended radio emission in the NW and SE of Abell 2146 can be best explained by the re-acceleration of fossil plasma (i.e. for the NW emission) or by the acceleration of thermal electrons (i.e. for the SE emission) by the outward propagating shocks and turbulence in the on-going cluster merger.



## 1.6 Future prospects

Our understanding of the origin and evolution of extended radio emission in galaxy clusters has been significantly improved with the increasing capabilities of modern radio telescopes (e.g. GMRT, LOFAR, JVLA, MWA). However, to obtain a precise picture of the physical processes, future studies will need to expand the observing frequency towards both low ( $\lesssim 100$  MHz) and high ( $\gtrsim 10$  GHz) frequencies. For instance, the turbulence re-acceleration model predicts the existence of a large number of ultra-steep spectrum radio haloes that are significantly brighter at low frequencies (e.g. Cassano et al. 2010). As predicted by the diffuse shock re-acceleration model for the formation of radio relics, many more relics become visible at low frequencies due to their steep spectra. A combination of low- and high-frequency ( $\gtrsim 10$  GHz) observations will provide information on the spectral curvature. This is crucial to distinguish between the various mechanisms in which radio-emitting relativistic particles in haloes and relics gain their energy. Moreover, in combination with polarization observations the properties of magnetic field (i.e. strength and topology) can also be better understood.

Deep radio observations at high resolutions ( $\lesssim 5$  arcsec) will also be key to study the morphology and spectral energy distribution of the extended sources in galaxy clusters. This will provide spatially resolved spectral measurements that allow for detailed comparisons between theoretical models and the observational data. In particular, shock-related (re-)acceleration models for the formation of radio relics predict the location of the particle (re-)acceleration. To study the properties of non-thermal components (i.e. magnetic field and cosmic ray particles) in the downstream region, high-resolution observations are required (e.g. Donnert et al. 2016).

To obtain a complete picture of the physical processes in cluster mergers, multi-wavelength studies using  $\gamma$ -rays, X-ray, optical, radio, and Sunyaev-Zel'dovich effect observations will be necessary. Such combined studies are important to make connections between the physical processes and to better understand the matter-energy transformation mechanisms in galaxy clusters.

# 2 | Deep LOFAR observations of the merging galaxy cluster CIZA J2242.8+5301

## Abstract

Previous studies have shown that CIZA J2242.8+5301 (the ‘Sausage’ cluster,  $z = 0.192$ ) is a massive merging galaxy cluster that hosts a radio halo and multiple relics. In this paper we present deep, high fidelity, low-frequency images made with the LOw-Frequency Array (LOFAR) between 115.5 and 179 MHz. These images, with a noise of  $140 \mu\text{Jy}/\text{beam}$  and a resolution of  $\theta_{\text{beam}} = 7.3'' \times 5.3''$ , are an order of magnitude more sensitive and five times higher resolution than previous low-frequency images of this cluster. We combined the LOFAR data with the existing GMRT (153, 323, 608 MHz) and WSRT (1.2, 1.4, 1.7, 2.3 GHz) data to study the spectral properties of the radio emission from the cluster. Assuming diffusive shock acceleration (DSA), we found Mach numbers of  $\mathcal{M}_n = 2.7_{-0.3}^{+0.6}$  and  $\mathcal{M}_s = 1.9_{-0.2}^{+0.3}$  for the northern and southern shocks. The derived Mach number for the northern shock requires an acceleration efficiency of several percent to accelerate electrons from the thermal pool, which is challenging for DSA. Using the radio data, we characterised the eastern relic as a shock wave propagating outwards with a Mach number of  $\mathcal{M}_e = 2.4_{-0.3}^{+0.5}$ , which is in agreement with  $\mathcal{M}_e^X = 2.5_{-0.2}^{+0.6}$  that we derived from Suzaku data. The eastern shock is likely to be associated with the major cluster merger. The radio halo was measured with a flux of  $346 \pm 64 \text{ mJy}$  at 145 MHz. Across the halo, we observed a spectral index that remains approximately constant ( $\alpha_{145 \text{ MHz}-2.3 \text{ GHz}}^{\text{across } \sim 1 \text{ Mpc}^2} = -1.01 \pm 0.10$ ) after the steepening in the post-shock region of the northern relic. This suggests a generation of post-shock turbulence that re-energises aged electrons.

D. N. Hoang, T. W. Shimwell, A. Stroe, et al.,  
MNRAS, 471, 1107 (2017)

## 2.1 Introduction

Diffuse Mpc-scale synchrotron emission has been observed in a number of galaxy clusters, revealing the prevalence of non-thermal components in the intra-cluster medium (ICM). This diffuse radio emission is not obviously associated with compact radio sources (e.g. galaxies) and is classified as two groups: radio halos and relics (e.g. see a review by Feretti et al. 2012). Radio halos often have a regular shape, approximately follow the distribution of the X-ray emission, and are apparently unpolarised. Radio relics often have an elongated morphology, are found in the cluster outskirts, and are strongly polarised at high frequencies. In the framework of hierarchical structure formation, galaxy clusters grow through a sequence of mergers of smaller objects (galaxies and sub-clusters). During merging events most of the gravitational energy is converted into thermal energy of the ICM, but a small fraction of it goes into non-thermal energy that includes relativistic electrons and large-scale magnetic fields. Energetic merging events leave observable imprints in the ICM such as giant shock waves, turbulence, and bulk motions whose signatures are observable with radio and X-ray telescopes (e.g. Brunetti & Jones 2014; Bruggen et al. 2012).

The (re-)acceleration mechanisms of relativistic electrons are still disputed for both radio halos and radio relics. There are two prominent models that have been proposed to explain the mechanisms in radio halos. (i) The re-acceleration model asserts that electrons are accelerated by turbulence that is introduced by cluster mergers (e.g. Brunetti et al. 2001; Petrosian 2001). (ii) The secondary acceleration model proposes that the relativistic electrons/positrons are the secondary products of hadronic collisions between relativistic protons and thermal ions present in the ICM (e.g. Dennison 1980; Blasi & Colafrancesco 1999; Dolag & Ensslin 2000). The former model is thought to generate radio emission that is observable for approximately 1 Gyr after major merging events (Brunetti et al. 2009; Miniati 2015). In the latter model the radio emission is sustained over the lifetime of a cluster due to the long lifetime of relativistic protons in the ICM leading to the continuous injection of secondary particles. The secondary model also predicts the existence of  $\gamma$ -rays as one of the products of the decay chain associated with hadronic collisions. But despite numerous studies with the Fermi Gamma-ray Space Telescope (e.g. Jeltama & Profumo 2011; Brunetti et al. 2012; Zandanel & Ando 2014; Ackermann et al. 2016), no firm detection of the  $\gamma$ -rays from the ICM has been challenging this scenario. Still secondary electrons may contribute to the observed emission, for instance

a hybrid model where turbulence re-accelerates both primary particles and their secondaries has also been proposed to explain radio halos (Brunetti et al. 2004; Brunetti & Lazarian 2011b; Pinzke et al. 2017); in this case the expected  $\gamma$ -ray emission is weaker than that expected in purely secondary models.

Radio relics are generally thought to trace shock waves in the cluster outskirts that are propagating away from the cluster after a merging event (e.g. Enßlin et al. 1998; Roettiger et al. 1999). It is also thought that some radio relics might be generated by shocks associated with in-falling matter from cosmic filaments (e.g. Enßlin et al. 1998; Enßlin & Gopal-Krishna 2001; Brown et al. 2011b). Particle acceleration at shocks can be described by the diffusive shock acceleration (DSA) model (e.g. Bell & R. 1978; Drury & O’C Drury 1983; Blandford & Eichler 1987). However shocks in galaxy clusters are weak ( $\text{Mach} \lesssim 5$ ) and in some cases the plausibility of the acceleration of thermal particles in the ICM by DSA is challenged by the observed spectra of radio relics and by the efficiencies that would be required to explain observations (e.g. see Brunetti & Jones 2014 for review, Akamatsu et al. 2015; Vazza et al. 2015; van Weeren et al. 2016c; Botteon et al. 2016a). However, these problems can be mitigated if the shock re-accelerates fossil electrons that have already been accelerated prior to the merging event (e.g. Markevitch et al. 2005; Kang & Ryu 2011; Kang et al. 2012). Obvious candidate sources of fossil electrons are radio galaxies on the outskirts of the relic cluster. Observationally, this re-acceleration mechanism was proposed to explain the radio emission in a few clusters such as Abell 3411-3412 (van Weeren et al. 2013, 2017), PLCKG287.0 +32.9 (Bonafede et al. 2014) and the Bullet cluster 1E 0657–55.8 (Shimwell et al. 2015).

## 2.2 The galaxy cluster CIZA J2242.8+5301

CIZA J2242.8+5301 (hereafter CIZA2242,  $z = 0.192$ ) is a massive galaxy cluster that hosts an excellent example of large-scale particle acceleration. CIZA2242 was originally discovered in the ROSAT All-Sky Survey and was identified as a galaxy cluster undergoing a major merger event by Kocevski et al. (2007). The cluster has since been characterised across a broad range of electromagnetic wavelengths including X-ray, optical and radio, and its properties have been interpreted with the help of simulations.

XMM-Newton X-ray observations (Ogreaan et al. 2013a) confirmed the merging state of the cluster and characterised its disturbed morphology and elongation in the north-south direction. Suzaku observations (Akamatsu

& Kawahara 2013; Akamatsu et al. 2015) detected an ICM temperature jump, indicating the presence of merger shocks in the north and south of the cluster. The Mach numbers of these shocks were estimated as  $\mathcal{M}_n = 2.7_{-0.4}^{+0.7}$  and  $\mathcal{M}_s = 1.7_{-0.3}^{+0.4}$ , respectively. Chandra observations (Ogreaan et al. 2014a) revealed additional discontinuities in the X-ray surface brightness in multiple locations in the cluster outskirts (see Fig. 8 in Ogreaan et al. 2014a). In the optical band, a comprehensive redshift analysis to study the geometry and dynamics of the merging cluster Dawson et al. (2015) found that CIZA2242 consists of two sub-clusters that are at similar redshift but have virtually no difference in the line-of-sight velocity ( $69 \pm 190 \text{ km s}^{-1}$ ) and are separated by a projected distance of  $1.3_{-0.10}^{+0.13}$  Mpc.

Radio observations with the GMRT (at 608 MHz) and WSRT (at 1.2, 1.4, 1.7, and 2.3 GHz) reported two opposite radio relics located at the outskirts (1.5 Mpc from the cluster centre, van Weeren et al. 2010). The northern relic has an arc-like morphology, a size of  $2 \text{ Mpc} \times 55 \text{ kpc}$ , spectral index gradients from  $-0.6$  to  $-2.0$  across the width of the relic and a high degree of polarisation (50 – 60%, VLA 4.9 GHz data). The relics have been interpreted as tracing shock waves propagating outward after a major cluster merger. The injection spectral index of  $-0.6 \pm 0.05$  of the northern relic, that was calculated from the radio observations, corresponds to a Mach number of  $4.6_{-0.9}^{+1.3}$  and is higher than the values derived from X-ray studies (e.g.  $\mathcal{M}_n^X = 2.54_{-0.43}^{+0.64}$  in Ogreaan et al. 2014a). The magnetic field strength was estimated to be within  $5 - 7 \mu\text{G}$  to satisfy the conditions of the spectral ageing, the relic geometry and the ICM temperature. Faint emission connecting the two relics was detected in the WSRT 1.4 GHz map and was interpreted as a radio halo by van Weeren et al. (2010) but was not characterised in detail. Stroe et al. (2013) performed further studies of CIZA2242 using GMRT 153 and 323 MHz data, in combination with the existing data. Integrated spectra for the relics were reported, and by using standard DSA/re-acceleration theory, Stroe et al. (2013) estimated Mach numbers of  $\mathcal{M}_n = 4.58 \pm 1.09$  for the northern radio relic (from the injection index of  $-0.6 \pm 0.05$  which they obtained from colour-colour plots) and  $\mathcal{M}_s = 2.81 \pm 0.19$  for the southern radio relic (derived from the integrated spectral index of  $-1.29 \pm 0.04$  using DSA model). Stroe et al. (2013) found variations in the radio surface brightness on scales of 100 kpc along the length of the northern relic and linked them with the variations in ICM density and temperature (Hoeft et al. 2011). Additionally Stroe et al. (2013) reported relics on the eastern side of the cluster and characterised 5 tailed radio galaxies spread throughout the ICM.

Despite CIZA2242 being an exceptionally well-studied cluster, several questions remain unanswered, such as (i) the discrepancy between the radio and X-ray derived Mach numbers for the northern and southern relics; (ii) the connection between the radio halo and the northern and southern relics; (iii) the spectral properties of the radio halo, southern and eastern relics; (iv) the nature of the eastern relics. In this paper we present LOFAR (Haarlem et al. 2013) observations of CIZA2242 using the High Band Antenna (HBA). With its excellent surface brightness sensitivity coupled with high resolution, LOFAR is well-suited to study objects that host both compact and very diffuse emission, such as CIZA2242. The high density of core stations is essential for the detection of diffuse emission from CIZA2242 which has emission on scales of up to  $17'$ . In this paper we offer new insights into the above questions by exploiting our high spatial resolution, deep LOFAR data in combination with the published GMRT, WSRT, Chandra and Suzaku data (van Weeren et al. 2010; Stroe et al. 2013; Ogorean et al. 2014a; Akamatsu et al. 2015).

Hereafter we assume a flat cosmology with  $\Omega_M = 0.3$ ,  $\Omega_\Lambda = 0.7$ , and  $H_0 = 70 \text{ km s}^{-1} \text{ Mpc}^{-1}$ . In this cosmology, an angular distance of  $1'$  corresponds to a physical size of  $192 \text{ kpc}$  at  $z = 0.192$ . In this paper, we use the convention of  $S \propto \nu^\alpha$  for radio synchrotron spectrum, where  $S$  is the flux density at frequency  $\nu$  and  $\alpha$  is the spectral index.

## 2.3 Observations and data reduction

### 2.3.1 LOFAR HBA data

CIZA2242 was observed with LOFAR during the day for 9.6 hours (8:10 AM to 17:50 PM) on February 21, 2015. The frequency coverage for the target observation was between 115.5 MHz and 179.0 MHz. The calibrator source 3C 196 was observed for 10 minutes after the target observation. Both observations used 14 remote and 46 (split) core stations (see Haarlem et al. 2013 for a description of the stations), the baseline length range is from 42 m to 120 km. A summary of the observations is given in Table 2.1.

To create high spatial resolution, sensitive images with good fidelity direction-independent calibration and direction-dependent calibration were performed. The direction-independent calibration of the target field aims to (i) remove the contamination caused by radio frequency interference (RFI) and the bright sources (e.g. Cassiopeia A, Cygnus A) located in the side lobes, (ii) to correct the clock offset between stations and (iii) to calibrate

Table 2.1: LOFAR HBA observation parameters

Observation IDs	L260393 (CIZA2242), L260397 (3C 196)
Pointing centres	22:42:53.00, +53.01.05.01 (CIZA2242), 08:13:36.07, +48.13.02.58 (3C 196)
Integration time	1 s
Observation date	February 21, 2015
Total on-source time	9.6 hr (CIZA2242), 10 min (3C 196)
Correlations	XX, XY, YX, YY
Frequency range	115.5-179.0 MHz (CIZA2242) 109.7-189.9 MHz (3C 196)
Total bandwidth	63.5 MHz (CIZA2242, usable 56.6 MHz)
Total number of sub-band (SB)	325 (CIZA2242, usable 290 SBs)
Bandwidth per SB	195.3125 kHz
Channels per SB	64
Number of stations	60 (46 split core + 14 remote)

the XX-YY phase of the antennas. For the direction dependent part, we used the recently developed facet calibration scheme that is described in van Weeren et al. (2016a).

Throughout the data reduction process, we used BLACKBOARD SELF-CAL (BBS, Pandey et al. 2009) for calibrating data, LOFAR Default Pre-Processing Pipeline (DPPP) for editing data (flag, average, concatenate), and w-Stacking Clean (WSClean, Offringa et al. 2014), Common Astronomy Software Applications (CASA, McMullin et al. 2007) and AWIMAGER (Tasse et al. 2012) for imaging.

### Direction-independent calibration

- Removal of RFI

The data of CIZA2242 and 3C 196 were flagged to remove RFI contamination with the automatic flagger AOFLAGGER (Offringa et al. 2012). The auto-correlation and the noisy channels at the edge of each subband (first and last two channels) were also removed with DPPP by the Radio Obser-

vatory<sup>1</sup>. The edge channels were removed to avoid calibration difficulties caused by the steep curved bandpass at the edge of subbands.

- Removal of of distant contaminating sources

As with other low-frequency observations, the data were contaminated by emission from strong radio sources dozens of degrees away from the target. This contamination is predominately from several A-team sources: Cassiopeia A (CasA), Cygnus A (CygA), Taurus A (TauA), Hercules A (HerA), Virgo A (VirA), and Jupiter. To remove this contamination, we applied two different techniques depending on the angular separation of the contaminating source and CIZA2242. Our efforts focused on the four high-elevation sources: CasA (12.8 kJy at 152 MHz), CygA (10.5 kJy at 152 MHz), TauA (1.43 kJy at 152 MHz), and HerA (0.835 kJy at 74 MHz) which are approximately 8°, 30°, 79°, and 85° away from CIZA2242 location, respectively (Baars et al. 1977; Gizani et al. 2005). The closest source, CasA, was subtracted from the CIZA2242 data using 'demixing', a technique developed by van der Tol et al. (2007), whereas the other A-team sources were removed based on the amplitude of their simulated visibilities. The former technique solves for direction-dependent gain solutions towards CasA using an input sky model, and subtracts the contribution of CasA from the data using these gain solutions and the input sky model. The sky model we used for CasA was from a high-resolution ( $\sim 10''$ ) image and contains more than 16,000 components with an integrated flux of 30.77 kJy (at 69 MHz, R. van Weeren, priv. comm.). The latter technique simulates visibilities of the A-team sources (CygA, TauA, and HerA) by performing inverse Fourier transforms of their sky models with the station beam applied in BBS and then flags the target data if the simulated visibility amplitudes are larger than a chosen threshold of 5 Jy.

- Amplitude calibration, initial clock-offset and XX-YY phase-offset corrections

Following the procedure that is described in van Weeren et al. (2010), we assumed the flux scale, clock offset and XX-YY phase offset are direction and time independent and can be corrected in the target field if they are derived from a calibrator observation. In this study, 3C 196 was used as a calibrator. First, the XX and YY complex gains were solved for each antenna every 4 s and 1.5259 kHz using a sky model of 3C 196 (V. N. Pandey, priv. comm.). The 3C 196 sky model contains 4 compact Gaussians

---

<sup>1</sup><http://www.lofar.org>



with a total flux of 83.1 Jy, which is consistent with the Scaife & Heald (2012) flux scale. In this calibration, the Rotation Angle  $\beta$  was derived to account for the differential Faraday Rotation effects from the parallel hand amplitudes. The LOFAR station beam was also used during the solve step to separate the beam effects from the complex gain solutions.

For LOFAR, while the core stations use a single clock, the remote stations have separate ones. The clocks are synchronised, but there are still small offsets. These offsets are up to hundreds of nano-seconds. We applied a clock-TEC separation technique to estimate the clock offsets (see van Weeren et al. 2016a for details). The XX-YY phase offsets for each station were calculated by taking the difference of the medians of the XX and YY phase gain solutions taken over the whole 10-minutes observation of 3C 196.

Finally the XX-YY phase offset, the initial clock offset, and the amplitude gains were transferred to the target data. Since the calibrator, 3C 196, is  $\sim 74^\circ$  away from the target field, it has different ionospheric conditions and we did not transfer the TEC solutions to the target.

- Initial phase calibration and the subtraction of all sources in the target field

The target data sets of single subbands were concatenated to blocks of 2-MHz bandwidth to increase S/N ratio in the calibration steps. The blocks were phase calibrated against a wide-field sky model which was extracted from a GMRT 153 MHz image (radius of  $\sim 2^\circ$  and at  $\sim 25''$  resolution, Stroe et al. 2013). Phase solutions for each 2-MHz block were obtained every 8 s, which is fast enough to trace typical ionospheric changes. Note that as we already had a good model of the target field, to reduce processing time we did not perform self-calibration of the field as has been done in other studies that also use the facet calibration scheme (e.g. van Weeren et al. 2016c).

After phase calibration, and to prepare for facet calibration, we subtracted all sources from the field. To do this, we made medium resolution ( $\sim 30''$ ) images of the CIZA2242 field for each 2 MHz block with WSClean (Briggs weighting, robust = 0). The size of these images is set to  $10^\circ \times 10^\circ$  so that it covers the main LOFAR beam. The CLEAN components, together with the direction independent gain solutions in the previous step, were used to subtract sources from the data. Afterwards, to better subtract low-surface brightness emission and remove sources further than  $10^\circ$  away from the location of CIZA2242, we followed the same steps as above. But the data, which were already source subtracted, were imaged at lower resolution ( $2'$ ) over a wide-field area ( $20^\circ \times 20^\circ$ ) that encompassed the second

sidelobe of the LOFAR beam. The low-resolution sky models were subtracted from the medium-resolution subtracted data using the direction-independent gain solutions. The target data sets, which we hereafter refer to as “blank” field datasets, now contain just noise and residuals from the imperfect source subtraction.

### **Direction-dependent calibration**

In principle, we could directly calibrate the antenna gains and correct for the ionospheric distortion in the direction of CIZA2242 by calibrating off a nearby bright source. However, the imperfections in the source subtraction that used direction-independent calibration solutions result in non-negligible residuals in the “blank” field images, especially in regions around bright sources. For this reason, we exploited facet calibration (van Weeren et al. 2016a) to progressively improve the source subtraction in the “blank” data sets, and consequentially, gradually reduce the noise in the “blank” field datasets as the subtraction improves. Below we briefly outline the direction dependent calibration procedure.

The CIZA2242 field was divided into 15 facets covering an area of  $\sim 3^\circ$  in radius. Each facet has its own calibrator consisting of one or more sources that have a total apparent flux in excess of 0.5 Jy (without primary beam correction). The number of facets here is close to that used in another cluster study by Shimwell et al. (2016) (13 facets), but far less than that in Williams et al. (2016) (33 facets) and van Weeren et al. (2016c) (70 facets). In this study we used few facets to reduce the computational time and because we only require high quality images of the cluster region which has radius of  $8'$ , whereas Williams et al. (2016) targeted a  $19 \text{ deg}^2$  wide-field image.

The procedure to calibrate each facet was as follows: Firstly, in the direction of each facet calibrator we performed a self-calibration loop to determine a single TEC and phase solution every 8 – 16 s per station per 8 MHz bandwidth, and a single gain solution every 4-16 mins per station per 2 MHz bandwidth. Secondly, Stokes I images of the entire facet region to which the direction-dependent calibration solutions were applied were made using WSClean. These full-bandwidth (56.6 MHz) images typically had a noise level of  $\sim 150 \mu\text{Jy}/\text{beam}$  and the CLEAN components derived from the imaging form a significantly improved frequency dependent sky model for the region (in comparison to the direction independent sky model). Thirdly, the facet sky models were subtracted from the individual 2-MHz bandwidth data sets using the gains and TEC solutions in the direction

of the facet calibrator that were derived during the self-calibration loop. This subtraction was significantly improved over the direction independent subtraction. This procedure was repeated to successfully calibrate and accurately subtract the sources in 11 facets, including the cluster facet, which was done last. Four of the facets failed as their facet centre is either far away ( $2.0^\circ - 2.7^\circ$ ) from the pointing centre or they had low flux calibrators which prevented us from obtaining stable calibration solutions. These failed facets had very little effect on the quality of the final cluster image as the subtraction of these facet sources using the low and medium resolution sky models with the direction-independent calibration solutions was almost sufficient to remove the artefacts across the cluster region.

### 2.3.2 GMRT, WSRT radio, Suzaku and Chandra X-ray data

In this paper, we used the GMRT 153, 323, 608 MHz and WSRT 1.2, 1.4, 1.7, 2.3 GHz data sets that were originally published by van Weeren et al. (2010) and Stroe et al. (2013). For details on the data reduction procedure, see Stroe et al. (2013). To study the X-ray emission from CIZA2242 we used observations from the Suzaku and Chandra X-ray satellites. We refer to Akamatsu et al. (2015) and Ogorean et al. (2014a) for the data reduction procedure.

### 2.3.3 Imaging and flux scale of radio intensity images

To make the final total intensity image of CIZA2242, we ran the CLEAN task in CASA on the full-bandwidth (56.6 MHz) data that was calibrated in the direction of the target. The imaging was done with multiscale-multifrequency (MS-MFS) CLEAN, multiple Taylor terms ( $n_{\text{terms}} = 2$ ) and W-projection options to take into account of the complex structure, the frequency dependence of the wide-bandwidth data sets and the non-coplanar effects (e.g. see Cornwell et al. 2005, 2008; Rau & Cornwell 2011). The multi-scale sizes used were 0, 3, 7, 25, 60, and 150 times the pixel size, which is approximately a fifth of the synthesised beam; the zero scale is for modelling point sources. The multi-scale CLEAN in CASA has been tested and shown to recover low-level diffuse emission properly, significantly minimise the clean “bowl”, recover flux closer to that of single-dish observations and leave more uniform residuals than classical single-scale CLEAN (Rich et al. 2008). Several images were made using Briggs weighting with different robust parameters to enhance diffuse emission at different scales (see Table 2.2). During imaging we also applied an inner uv cut of  $0.2 k\lambda$ .

to filter out the (possible) emission on scales larger than  $17'$  ( $\sim 3.2$  Mpc), which is approximately the physical size of the cluster. The final image was corrected for the primary beam attenuation (less than 0.5% at the cluster outskirts) by dividing out the real average beam model<sup>2</sup> that was produced using AWIMAGER (Tasse et al. 2012).

The amplitude calibration was performed using the primary calibrator 3C 196 (see Subsec. 2.3.1). To check our LOFAR flux scale, we compared the integrated fluxes of the diffuse emission of the northern relic and two bright point-like sources (source 1,  $\sim 1$  Jy, at RA=22:41:33, Dec=+53.11.06; source 2,  $\sim 0.1$  Jy, at RA=22:43:37, Dec=+53.09.16) in our LOFAR image with the values that are predicted from spectral fitting of the GMRT 153, 323, 608 MHz and WSRT 1.2, 1.4, 1.7, 2.3 GHz data (Stroe et al. 2013). For this comparison, we used identical imaging parameters for the LOFAR, GMRT and WSRT data sets (see the parameters for the  $16'' \times 18''$  images in Table 2.2). The predicted fluxes were found to be  $S_n = 1593 \pm 611$  mJy,  $S_1 = 1081 \pm 124$  mJy and  $S_2 = 119 \pm 3$  mJy for the northern relic, source 1 and 2, respectively. The values that were measured within  $3\sigma_{\text{noise}}$  regions of our LOFAR image were  $S_n = 1637 \pm 37$  mJy,  $S_1 = 1036 \pm 1$  mJy and  $S_2 = 92 \pm 1$  mJy and are in good agreement with the spectral fitting predicted values. This LOFAR flux for the northern relic was only 3% higher than the predicted value, and the fluxes for source 1 and 2 were 4% and 22% lower than the predicted values. Despite of this agreement of the LOFAR, GMRT and WSRT fluxes, throughout this paper, unless otherwise stated, we used a flux scale error of 10% for all LOFAR, GMRT, WSRT images when estimating the spectra of diffuse emission. Similar values have been widely used in literature (e.g. Shimwell et al. 2016; van Weeren et al. 2016c).

### 2.3.4 Spectral index maps

Our high-fidelity LOFAR images have allowed us to map the spectral index distribution with improved resolution. In previous works (van Weeren et al. 2010; Stroe et al. 2013), CIZA2242 was studied with the GMRT and WSRT at seven frequencies from 153 MHz to 2.3 GHz. Our LOFAR 145 MHz data was combined with these published data sets to study spectral characteristics of the cluster. However, these observations were performed with different interferometers each of which has a different uv-coverage, and this results in a bias in the detectable emission and the spectra. To minimise the difference, we (re-)imaged all data sets with the same weighting scheme

---

<sup>2</sup>the square root of the AWIMAGER .avgpb map.

Table 2.2: Imaging parameters

Resolution (Fig.)	7.3" × 5.3" (2.1)	6.5" × 6.5" <sup>a</sup> (2.5 <sup>b</sup> )	12" × 12" <sup>a</sup> (2.15)	16" × 18" <sup>a</sup> (2.8 <sup>b</sup> )	35" × 35" <sup>a</sup> (2.4, 2.12 <sup>b</sup> )
Mode	MFS	MFS	MFS	MFS	MFS
Weighting	Briggs	Uniform	Briggs	Uniform	Briggs
Robust	-0.25	N/A	0.25	N/A	0.5
uv-range (kλ)	≥ 0.2	0.2 – 50 <sup>c</sup>	≥ 0.2	0.2 – 50 <sup>c</sup>	0.2 – 50 <sup>c</sup>
Multi-scales	[0, 3, 7, 60, 150]	[0, 3, 7, 60, 150]	[0, 3, 7, 60, 150]	[0, 3, 7, 60, 150]	[0, 3, 7, 60, 150]
Grid mode	wide-field	wide-field	wide-field	wide-field	wide-field
W-projection	128 <sup>d</sup>	384 <sup>d</sup> , 128 <sup>e</sup>	128 <sup>d</sup>	384 <sup>d</sup> , 128 <sup>e</sup> , 256 <sup>f</sup>	384 <sup>d</sup> , 128 <sup>e</sup> , 256 <sup>f</sup>
N-terms	2 <sup>d</sup>	2 <sup>d</sup> , 1 <sup>e</sup>	2 <sup>d</sup>	2 <sup>d</sup> , 1 <sup>e,f</sup>	2 <sup>d</sup> , 1 <sup>e,f</sup>
Image RMS (μJy/beam)	140 <sup>d</sup>	200 <sup>d</sup> , 37 <sup>e3</sup>	210 <sup>d</sup>	312 <sup>d</sup> , 1358 <sup>e1</sup> , 414 <sup>e2</sup> , 64 <sup>e3</sup> , 70 <sup>f1</sup> , 31 <sup>f2</sup> , 38 <sup>f3</sup> , 43 <sup>f4</sup>	2000 <sup>e1</sup> , 495 <sup>e2</sup> , 177 <sup>e3</sup> , 99 <sup>f1</sup> , 71 <sup>f2</sup> , 73 <sup>f3</sup> , 70 <sup>f4</sup>

Notes: <sup>a</sup>: smoothed, <sup>b</sup>: spectral index map, <sup>c</sup>:  $uv_{\max} = 50$  kλ only used for LOFAR data, <sup>d</sup>: LOFAR, <sup>e</sup>: GMRT (<sup>e1</sup>, <sup>e2</sup> and <sup>e3</sup> are for 153, 323 and 608 MHz, respectively), <sup>f</sup>: WSRT (<sup>f1</sup>, <sup>f2</sup>, <sup>f3</sup> and <sup>f4</sup> are for 1.2, 1.4, 1.7 and 2.3 GHz, respectively)

of visibilities and selected only data with a common inner uv-cut of  $0.2\text{ k}\lambda$ . To make the spectral index maps all images were made using MS-MFS CLEAN (multiscale =  $[0, 3, 7, 25, 60, 150] \times$  pixel sizes and nterms = 1 and 2 for GMRT/WSRT and LOFAR images, respectively). Only those pixels with values  $\geq 3\sigma_{\text{noise}}$  in each of the individual images were used for the spectral index calculation. We note that this  $\geq 3\sigma_{\text{noise}}$  cut-off introduces a selection bias for steep spectrum sources. For example, the sources that were observed with LOFAR at  $\geq 3\sigma_{\text{noise}}$  but were not detected ( $< 3\sigma_{\text{noise}}$ ) with the GMRT/WSRT observations were not included in the spectral index maps. To reveal spectral properties of different spatial scales, we made spectral index maps at  $6.5''$ ,  $18'' \times 16''$  and  $35''$  resolution (see Table 2.2 for a summary of the imaging parameters).

The  $6.5''$ -resolution spectral index map was made with the LOFAR 145 MHz and GMRT 608 MHz data sets. The imaging used uniform weighting for both data sets. In addition a common uv-range was used ( $0.2\text{ k}\lambda$  to  $50\text{ k}\lambda$ ) and a uvtaper of  $6.0''$  was applied to reduce the sidelobes and help with CLEAN convergence. Here, the  $50\text{ k}\lambda$  is the maximum uv distance of the GMRT data set. The native images reach resolution of  $\sim 6''$  ( $5.5'' \times 5.3''$  for the LOFAR 145 MHz,  $5.7'' \times 5.4''$  for the GMRT 608 MHz), which were then convolved with a 2D Gaussian kernel to a common resolution of  $6.5''$ , aligned with respect to the LOFAR image, and regridded to a common pixelisation. To align the images, we fitted compact sources with 2D Gaussian functions to find their locations which were used to estimate the average displacements between the GMRT/WSRT and LOFAR images. The GMRT/WSRT images were then shifted along the RA and DEC axes. The final images were combined to make spectral index maps according to

$$\alpha_{\text{pixel}} = \frac{\ln \frac{S_1}{S_2}}{\ln \frac{\nu_1}{\nu_2}}, \quad (2.1)$$

where  $S_1$  and  $S_2$  are the pixel values of the LOFAR and GMRT maps at the frequency  $\nu_1 = 145\text{ MHz}$  and  $\nu_2 = 608\text{ MHz}$ , respectively. We estimated the spectral index error on each pixel,  $\Delta\alpha_{\text{pixel}}$ , taking into account the image noise  $\sigma_{\text{noise}}$  and the flux scale error of  $f_{\text{err}} = 10\%$

$$\Delta\alpha_{\text{pixel}} = \frac{1}{\ln \frac{\nu_1}{\nu_2}} \sqrt{\left(\frac{\Delta S_1}{S_1}\right)^2 + \left(\frac{\Delta S_2}{S_2}\right)^2}, \quad (2.2)$$

where  $\Delta S_i = \sqrt{(\sigma_{\text{noise}}^i)^2 + (f_{\text{err}} \times S_i)^2}$  are the total errors of  $S_i$ . The spectral index error for a region that covers more than one pixel and has constant

spectral indices is calculated as follows

$$\Delta\alpha_{\text{region}} = \frac{\sqrt{\sum_1^{N_{\text{beams}}} (\overline{\Delta\alpha_{\text{pixels}}})^2}}{N_{\text{beams}}}, \quad (2.3)$$

where  $\overline{\Delta\alpha_{\text{pixels}}}$  is an average of all  $\Delta\alpha_{\text{pixels}}$  in the region of area of  $N_{\text{beams}}$  beam sizes.

The  $18'' \times 16''$ -resolution map was made with the LOFAR 145 MHz, GMRT 153, 323, 608 MHz, and the WSRT 1.2, 1.4, 1.7, 2.3 GHz data sets. The imaging was done with similar settings as used for the  $6.5''$ -resolution map (uniform weighting,  $uv_{\text{min}} = 0.2 \text{ k}\lambda$ ,  $uv_{\text{max}} = 50 \text{ k}\lambda$ ). Here a  $uv_{\text{taper}} = 6''$  is only applied to the LOFAR and GMRT 608 MHz data sets to improve the CLEAN convergence. All eight images were then smoothed to a common resolution of  $18'' \times 16''$ , aligned with respect to the LOFAR image, and regridded. To obtain the eight-frequency spectral index map, we fitted a power-law function to each pixel of the eight images using a weighted least-squares technique. The fitting was done only on pixels that have a signal of  $\geq 3\sigma_{\text{noise}}$  in least four observations. To take into account the uncertainties of the individual maps, the pixels are weighted by the inverse-square of their total pixel errors ( $1/\Delta S_i^2$ ) which includes the individual image noise  $\sigma_{\text{noise}}$  and an error of 10% in the flux scale (Eq. 2.2).

The  $35''$ -resolution map was made in a similar manner to the  $18'' \times 16''$ -resolution spectral index map ( $uv_{\text{min}} = 0.2 \text{ k}\lambda$ , MS-MFS, W-projection). However, instead of using uniform weighting, Briggs weighting (robust = 0.5) was used to increase S/N ratio of the diffuse emission associated with CIZA2242. The outer taper used for each image was set to obtain a spatial resolution of nearly  $30''$ . The images were then convolved with a 2D Gaussian kernel to give images with a common resolution of  $35''$ , aligned with respect to the LOFAR image, and regridded to have the same pixel size. The  $35''$  spectral index and corresponding error maps between 145 MHz and 2.3 GHz were made following the procedure that was used for the  $18'' \times 16''$ -resolution maps, except that the minimum number of detections ( $\geq 2\sigma_{\text{noise}}$ ) was limited to three, rather than four, images.

## 2.4 Results

In Fig. 2.1, we present our deep, high-resolution ( $7.3 \text{ arcsec} \times 5.3 \text{ arcsec}$ ) LOFAR 145 MHz image of CIZA2242. The RMS noise reaches  $140 \mu\text{Jy}/\text{beam}$ , making this image one of the deepest, high-resolution, low-frequency (<

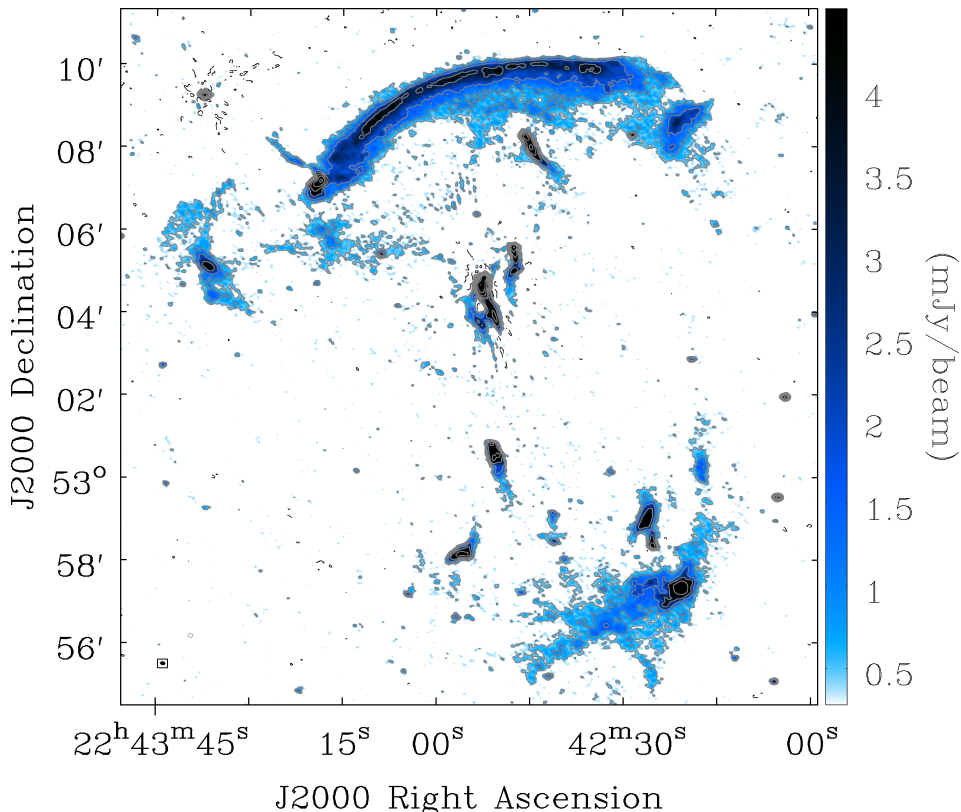


Figure 2.1: LOFAR total intensity high-resolution ( $7.3 \text{ arcsec} \times 5.3 \text{ arcsec}$ , bottom left corner) map of CIZA2242 and its contours levelled at  $[-3, 3, 6, 12, 24, 48, 96, 192, 384] \times \sigma_{\text{noise}}$ ,  $\sigma_{\text{noise}} = 140 \mu\text{Jy}/\text{beam}$ . The negative contours are black dashed lines.

200 MHz) radio images of a galaxy cluster. The labelling convention of Stroe et al. (2013) is adopted and is presented in Fig. 2.2. In Fig. 2.3, we show a low-resolution ( $35 \text{ arcsec}$ ) LOFAR image. The low-resolution contours are plotted over a Chandra X-ray image (smoothed to  $6 \text{ arcsec}$  resolution using a Gaussian kernel, Ogorean et al. 2014a) in Fig. 2.4. In Fig. 2.5, we show our high-resolution ( $6.5 \text{ arcsec}$ ) spectral index map from 145 to 608 MHz.

### 2.4.1 Northern relic

The northern relic (RN) is nicely mapped out in our LOFAR image (Fig. 2.1). Its morphology shows a familiar arc-like feature with a projected linear size of  $1.9 \text{ Mpc} \times 230 \text{ kpc}$  (measured at  $3\sigma_{\text{noise}}$  contours). The length of



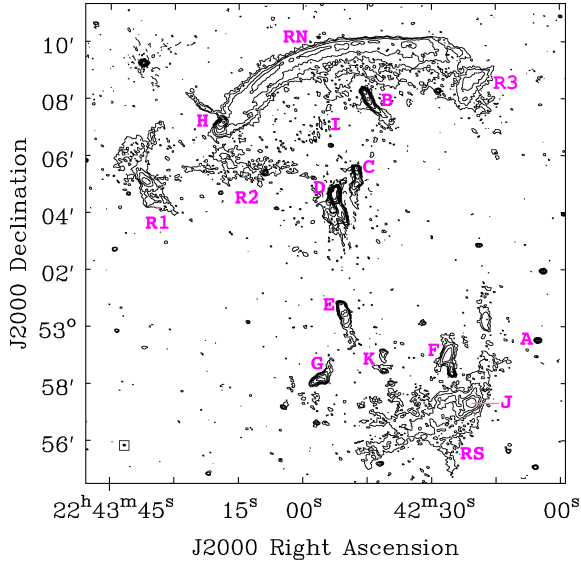


Figure 2.2: Source labels are adapted from Stroe et al. 2013. We label the patchy emission west of RN as R3. The contours are identical to those in Fig. 2.1.

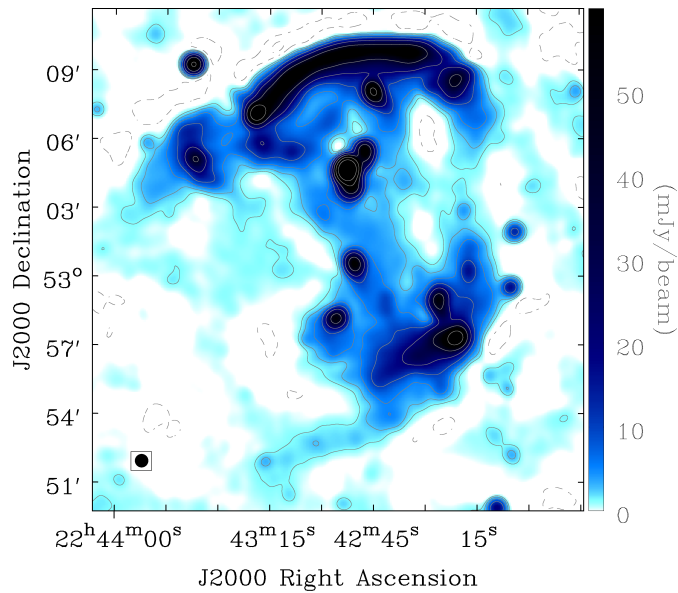


Figure 2.3: LOFAR total intensity low-resolution (35 arcsec, bottom left corner) image of CIZA2242. The radio contour levels are at  $[-6, -3, 3, 6, 12, 24, 48, 96, 192, 384] \times \sigma_{\text{noise}}$  ( $\sigma_{\text{noise}} = 430 \mu\text{Jy}/\text{beam}$ ). The negative contours are dashed lines.

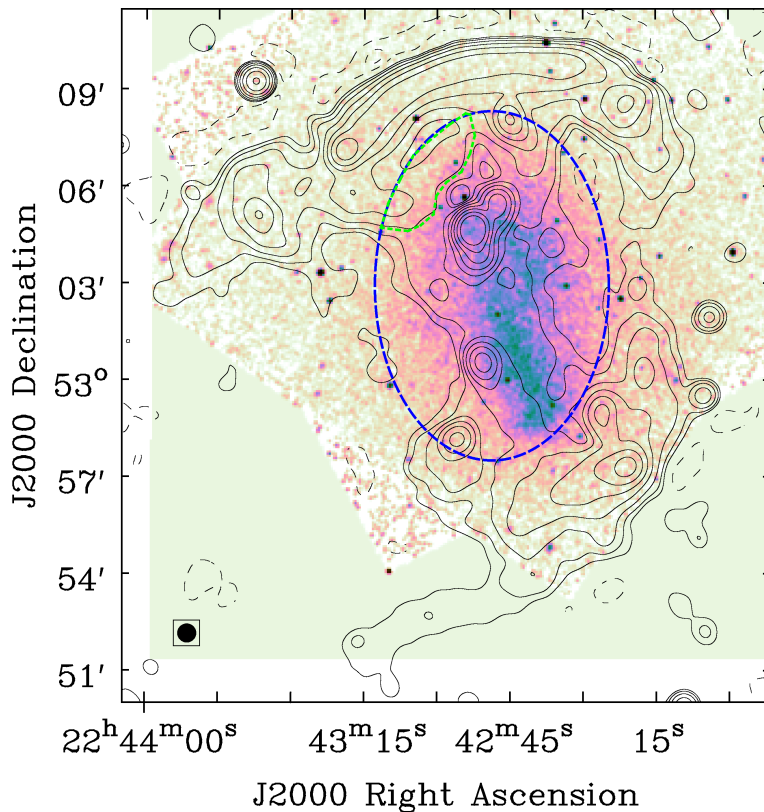


Figure 2.4: LOFAR low-resolution (35 arcsec, bottom left corner) contours of CIZA2242 on top of Chandra X-ray image in the 0.5 – 7.0 keV band (being smoothed to 6 arcsec resolution, Ogrea et al. 2014a). The radio contour levels are identical to those in Fig. 2.3 The blue dashed elliptical region is approximately the halo emission region. The green dotted region is over the source I.

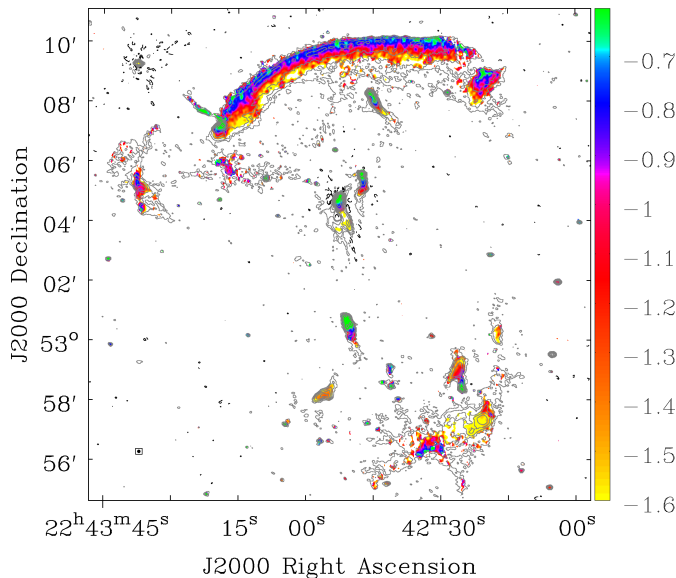


Figure 2.5: A 6.5 arcsec-resolution spectral index map of CIZA2242 from 145 to 608 MHz. The LOFAR contours are identical to those in Fig. 2.1. The corresponding error map is shown in Fig. 17.

RN increases to 2.1 Mpc when measured in the 35 arcsec map (Fig. 2.3). Its surface brightness has a sharp edge on the northern side and a more gradual decline on the southern side with additional diffuse emission north of source B. The integrated flux of RN (including the patchy emission in the west, source R3 in Fig. 2.2) is measured to be  $1548.2 \pm 4.6$  mJy within the  $\geq 3\sigma_{\text{noise}}$  region. The flux increases by 4.6% and 8.3% for the  $\geq 2\sigma_{\text{noise}}$  and  $\geq 1\sigma_{\text{noise}}$  regions, respectively. The spectral index map between 145 and 608 MHz (Fig. 2.5) shows a clear steepening from the north towards the cluster centre, ranging roughly from  $-0.80$  to  $-1.40$ . In Fig. 2.6, we plot the integrated fluxes of RN between 145 MHz and 2.3 GHz which were calculated within the LOFAR  $\geq 3\sigma_{\text{noise}}$  region. The spectral index obtained from a weighted least-squares fitting of a power-law function to the RN fluxes at eight frequencies is  $-1.11 \pm 0.04$ , which is consistent with the previous values of  $-1.08 \pm 0.05$  (van Weeren et al. 2010) and  $-1.06 \pm 0.04$  (Stroe et al. 2013).

Towards the western side of RN, the main relic connects with source R3 via a faint bridge (a  $3\sigma_{\text{noise}}$  detection). Towards the eastern side, RN is attached to source H, which is much brighter than other regions of the relic

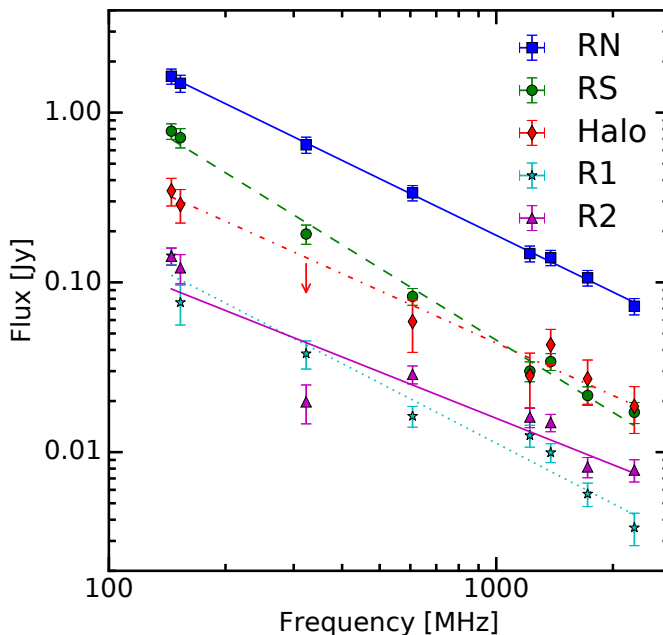


Figure 2.6: Integrated radio spectra of RN, RS, the halo, R1 and R2 from 145 MHz to 2.3 GHz including the LOFAR data points at the lowest frequency 145 MHz. The red downwards pointing arrow is the upper limit derived from the GMRT 323 MHz observations. The substantial scatter around the lines of best fit for the halo, R1 and R2 (e.g. compared with RN and RS) could be caused by the low signal to noise of the detections and the difficulty in precisely imaging large faint diffuse sources. Given the comparatively high surface brightness sensitivity of LOFAR, it is possible that the spectral indices for these sources is artificially steepened. The weighted best-fit integrated spectral indices are listed in Table 2.3. The integrated fluxes for the relics and halo are given in Table 5.

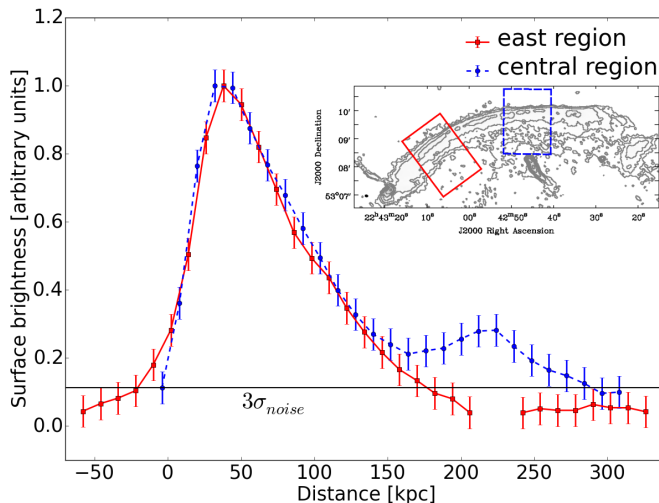


Figure 2.7: Surface brightness profiles (normalised) along the width of RN (in north-south direction) for the central (blue dashed) and east (red solid) regions (overlaid image). The data ( $\geq 1\sigma_{\text{noise}}$ ) is averaged within 4 arcsec along the profile.

(the peak brightness is 30 mJy/beam, compared with a typical brightness 4.5 mJy/beam in RN). The northern emission associated with source H has the expected morphology for an AGN.

In the post-shock central region of RN, an excess of emission was detected at a significance of up to  $6\sigma_{\text{noise}}$  in front of source B. This emission has an arc-like shape with a projected linear size of  $\sim 135 \text{ kpc} \times 500 \text{ kpc}$  within the  $3\sigma_{\text{noise}}$  contours (Fig. 2.1). Interestingly, this feature was not detected in the post-shock eastern region of RN, where no tailed AGN are observed. The excess emission is more visible in the surface brightness profiles along the width of RN for the central and eastern regions in Fig. 2.7. Since the excess emission is located in front of source B and has a shock-like morphology, we speculate that this excess emission could be a bow shock generated by an interaction between the tailed AGN (source B) and the downstream relativistic electrons. We will present further analysis of this speculation in an upcoming paper.

#### 2.4.2 Southern relic

The southern relic (RS) is detected in our LOFAR map in Fig. 2.1 with a peak signal to noise of  $\sim 20$ . The distance between the outer edges of RN and RS is measured to be 2.8 Mpc or 3.2 Mpc in the 6.5 arcsec or 35 arcsec

maps, respectively. The width of RS is wider in the central region with a size of  $\sim 270$  kpc within the  $\geq 3\sigma_{\text{noise}}$  region (Fig. 2.1). Within this central area the region labelled J covers  $\sim 200$  kpc in radius and has substantially higher (threefold) surface brightness than the rest of the relic but no obvious counterpart in the optical data (see Fig. A.1. in Stroe et al. 2013).

The emission in the region of RS includes newly detected faint diffuse emission in the south-east region (Fig. 2.4 or Fig. 17). The size of RS in projection covers a maximum linear distance of  $\sim 1.4$  Mpc as measured within the  $3\sigma_{\text{noise}}$  contours in the 6.5 arcsec map. But its length when measured in the 35 arcsec map in Fig. 2.4 significantly increases to  $\sim 2$  Mpc or  $\sim 3$  Mpc when excluding or including the south-east emission. Within this new south-east region of emission, there are four optical sources which correspond to peaks in the radio emission as shown in Fig. 17. This faint emission could be the result of a collection of compact sources or it could be an in-falling filament at the cluster redshift. Unfortunately, we were unable to constrain the redshifts for the optical sources with the existing optical data. Additionally, faint diffuse emission is observed to extend south-westwards from the central region of RS (Fig. 2.1).

The zoom-in spectral index map of RS (eight frequencies from 145 MHz to 2.3 GHz) that is shown in Fig. 2.8 shows steepening towards the cluster centre. The spectral index drops approximately from  $-0.85$  to  $-1.40$  in the south-east region and from  $-1.35$  to  $-1.70$  in the north-west region. Similar trends are seen in the 145 – 608 MHz spectral index map in Fig. 2.5. The north-west region of RS (Fig. 2.8) is dominated by diffuse emission in region J which has a very steep mean spectral index of  $-2.0$ . The region of flat spectrum in the south-east part (Fig. 2.8, left) has an L shape appearance and a steep spectrum of mean value of  $-0.93 \pm 0.10$ . The west region of RS (Fig. 2.8, left) has an arc-like shape with an average spectral index of  $-1.30 \pm 0.04$  (excluding region J). We estimated the integrated spectral index for RS (within the LOFAR  $\geq 3\sigma_{\text{noise}}$  region, including region J) to be  $-1.41 \pm 0.05$  (Fig. 2.6), which is steeper than the value of  $-1.29 \pm 0.04$  that was reported in Stroe et al. (2013).

### 2.4.3 Eastern relics

East of the cluster centre, slightly south, from RN (Fig. 2.1) are the relics R1 and R2, which were previously identified in Stroe et al. (2013). R1 consists of a thin narrow region. It is  $\sim 630$  kpc long and oriented in the north-south direction. R1 has a bright region in the middle and patchy emission in the north-east. In Fig. 2.8 we show the eight-frequency spectral index distribu-

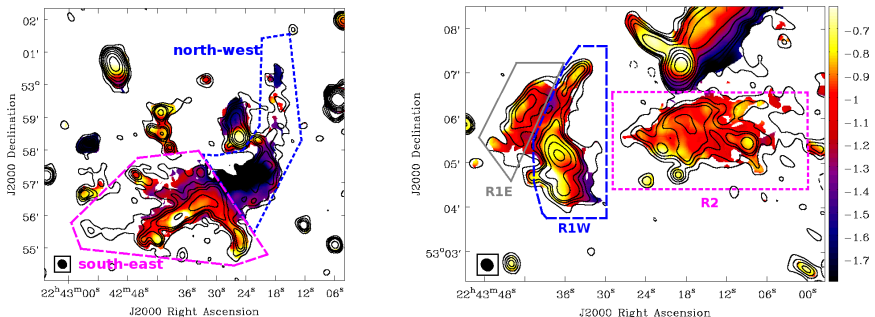


Figure 2.8: Zoom-in mid-resolution ( $18 \text{ arcsec} \times 16 \text{ arcsec}$ ) spectral index maps of RS (left) and the eastern relics (right) from 145 MHz to 2.3 GHz (eight frequencies). The overlaid WSRT 1.4 GHz contours at the same resolution are levelled at  $[3, 6, 9, 12, 24, 48, 96, 192, 384, 768] \times \sigma_{\text{noise}}$  ( $\sigma_{\text{noise}} = 31.2 \mu\text{Jy/beam}$ ).

tion ( $18 \text{ arcsec} \times 16 \text{ arcsec}$ ) of the eastern relics. Based on morphology and spectral index, we divided R1 into two regions: R1E in the north-east and R1W in the north-west (see Fig. 2.8). R1W has an arc-like morphology and shows spectral index steepening from approximately  $-0.70$  to  $-1.40$  towards the centre. The spectral index of R1E drops from approximately  $-0.75$  to  $-1.20$  in the same direction.

R2 has a physical size of  $670 \text{ kpc} \times 270 \text{ kpc}$  with the major axis in the west-east direction (Fig. 2.8, right). Its spectral index between 145 MHz and 2.3 GHz remains approximately constant across its structure with a mean of  $-0.95 \pm 0.08$ .

The integrated fluxes over the  $\geq 3\sigma_{\text{noise}}$  region in the LOFAR  $18 \text{ arcsec} \times 16 \text{ arcsec}$  image after masking out the compact sources were estimated to be  $143.5 \pm 8.3 \text{ mJy}$  and  $142.5 \pm 8.1 \text{ mJy}$  for R1 and R2, respectively. The integrated spectral indices between 145 MHz and 2.3 GHz are  $-1.18 \pm 0.06$  for R1 and  $-0.91 \pm 0.06$  for R2.

#### 2.4.4 Radio halo

The halo was discovered by van Weeren et al. (2010) with WSRT observations at 1.4 GHz. Part of the emission was also seen in the GMRT 153 MHz image that was presented in Stroe et al. (2013). However, its flux and spectral properties have not been well studied. With our deep LOFAR image, we are able to characterise the radio halo as the large number of short baselines give LOFAR excellent sensitivity to cluster-scale emission. In Fig. 2.3, we show a low-resolution ( $35 \text{ arcsec}$ ) image of CIZA2242. The image shows

diffuse emission connecting RN and RS with a significance up to  $9\sigma_{\text{noise}}$  ( $\sigma_{\text{noise}} = 430 \mu\text{Jy}/\text{beam}$ ). The emission covers an area of  $1.8 \text{ Mpc} \times 830 \text{ kpc}$  with its major axis elongated in the north-south direction broadly following the Chandra X-ray emission that was mapped by Ogrea et al. (2014a).

The 145 MHz flux of the radio halo was estimated from the LOFAR data in an elliptical region that was selected to cover the Chandra X-ray emission (Fig. 2.4). However, this region also hosts radio galaxies (i.e. source B, C, D, E, F, G, K) and diffuse emission from source I. We attempted to remove these contaminating sources from the halo flux estimation in two steps. In the first step, models of the radio galaxies were subtracted from the uv data. To obtain the radio galaxy models we created a LOFAR image using parameters that are similar to those used for the high-resolution (6.5 arcsec) image, except the inner uv cut was set to  $0.4 \text{ k}\lambda$  instead of  $0.2 \text{ k}\lambda$  (see Table 2.2 for the imaging parameters). Here the inner uv cut was used to filter out the large-scale emission from the halo to leave only the radio galaxies. The CLEAN components of these radio galaxies were subtracted from the uv data which were then imaged and smoothed to obtain a 35 arcsec image. The radio halo flux  $S_1$  in the  $\geq 3\sigma_{\text{noise}}$  elliptical region (blue dashed in Fig. 2.4), with source I masked, was measured from this 35 arcsec image. In the second step, the radio halo flux  $S_2$  in the source I region (green dotted in Fig. 2.4) was estimated by extrapolating the halo flux  $S_1$  using a scaling factor proportional to ratio of the areas (i.e.  $\text{Area}_{S_2}/\text{Area}_{S_1} = 0.085$ ). We did not subtract source I from the uv data due to it having large-scale diffuse emission which is difficult to disentangle from the halo emission. Finally, the total halo flux ( $S_h = S_1 + S_2$ ) was estimated to be  $S_h^{145 \text{ MHz}} = 346 \pm 64 \text{ mJy}$ . Where we calculated the total error following Cassano et al. (2013) and took into account the flux scale uncertainty (i.e. 10%), image noise over the halo area and source subtraction uncertainty (i.e. 5% of the total flux of the subtracted radio galaxies); additionally, we added an estimate of the uncertainty associated with the extrapolation of the halo flux in the source I region (i.e. assuming 10%). The source subtraction error of 5% was estimated from the ratio of the post source subtraction residuals to the pre source subtraction flux of a nearby compact source (i.e. at RA=22:432:37, Dec=+53.09.16). Another uncertainty in the integrated flux is the area used for the integration. To assess the dependence on this we estimated the integrated radio flux within regions bounded by  $\geq 2\sigma_{\text{noise}}$  and  $\geq 1\sigma_{\text{noise}}$  within the elliptical region. We found the total halo flux at 145 MHz remained approximately stable ( $S_h^{145 \text{ MHz}} = 362 \pm 65 \text{ mJy}$  for  $\geq 2\sigma_{\text{noise}}$  or  $S_h^{145 \text{ MHz}} = 371 \pm 66 \text{ mJy}$  for  $\geq 1\sigma_{\text{noise}}$ ).



Table 2.3: Integrated spectral indices between 145 MHz and 2.3 GHz.

Source	$\alpha_{\text{int}}^a$	$\alpha_{\text{int}}^b$
RN	$-1.11 \pm 0.04$	$-1.06 \pm 0.04$
RS	$-1.41 \pm 0.05$	$-1.29 \pm 0.04$
R1	$-1.18 \pm 0.06^c$	$-0.74 \pm 0.07$
R2	$-0.91 \pm 0.06$	$-0.90 \pm 0.06$
Halo	$-1.03 \pm 0.09^d$	N/A

Notes:  $a$ : a flux scale uncertainty of 10%;  $b$ : Stroe et al. 2013;  $c$ : compact source was masked;  $d$ : compact source subtraction error of 5% and an uncertainty of 10% from the extrapolation of the halo emission in the source I region were added.

Following a similar procedure we estimated the halo flux in the GMRT/WSRT data sets within the same region used for the LOFAR data. Unfortunately, due to the depth of the GMRT/WSRT observations, the halo emission was only partly detected in the GMRT 153, 608 MHz and WSRT 1.2, 1.4, 1.7, 2.3 GHz maps and undetected in the GMRT 323 MHz map. This may induce systematics in the spectral index estimate that deserve sensitive observations at higher frequencies in the future. In this paper we attempt our best following the approaches adopted in previous papers (e.g. van Weeren et al. 2016c; Stroe et al. 2013). First we used a common uv range (i.e. 0.2–50 k $\lambda$ ) and Briggs weighting (robust=0.5) when making the 35 arcsec images (see Subsec. 2.3.4). We also added an absolute flux scale uncertainty of 10% to mitigate the impact on our conclusions due to possible missing flux in some observations. Due to the large uncertainties that are propagated in the above procedure (i.e. flux scale, image noise, source subtraction and extrapolation), we only created source subtracted low-resolution (35 arcsec) images. From these we estimated the inverse-variance weighted integrated spectrum which is plotted in Fig. 2.6. Using the combination of LOFAR, GMRT and WSRT data sets, the integrated spectral index from 145 MHz to 2.3 GHz of the radio halo was estimated to be  $-1.03 \pm 0.09$  and was found to remain approximately constant for different  $\sigma_{\text{noise}}$  cuts on the area of integration (i.e.  $1 - 3\sigma_{\text{noise}}$ ).

#### 2.4.5 Tailed radio galaxies

Our LOFAR maps show that there are at least six tailed radio galaxies in CIZA2242 (i.e. source B, C, D, E, F, G in Fig. 2.1), a remarkably large

number for any cluster. We mentioned in Sec. 2.1 that direct acceleration of thermal electrons by merger shocks is unable to explain the observed spectra and the efficiencies of electron acceleration for a number of relics (e.g. Akamatsu et al. 2015; Vazza et al. 2015; van Weeren et al. 2016c; Botteon et al. 2016a). These problems could be solved with shock re-acceleration of fossil relativistic electrons. Tailed radio galaxies (e.g. Miley et al. 1972) are obvious reservoirs of such electrons, after activity in their nuclei has ceased or become weak. Indeed, some radio tails, such as 3C 129 (e.g. Lane et al. 2002) have Mpc-scale lengths and morphologies that bear striking resemblance to those of relics. Recent studies show evidence for particle re-acceleration of fossil electrons from radio galaxies in the radio relics of PLCKG287.0+32.9 (Bonafede et al. 2014) and Abell 3411-3412 (van Weeren et al. 2017). In the case of CIZA2242 there are bright radio galaxies located at the eastern extremity of RN (i.e. source H) and at the brightest central region of RS (i.e. source J). Whilst it remains unclear whether these radio galaxies are related to RN a scenario where fossil plasma could contribute to the emission in RN was previously discussed in Shimwell et al. (2015).

The combined systematic study of relics and tailed radio galaxies with radio sky surveys (e.g. Norris et al. 2017; Röttgering et al. 2011; Shimwell et al. 2017) may shed light on the role of tailed radio galaxies in the formation of radio relics, in particular in the case that radio relics originate from re-acceleration of fossil relativistic electrons and rather than from the acceleration of thermal plasma.

## 2.5 Discussion

CIZA2242 is one of the best studied merging clusters. In the radio band Stroe et al. (2013) carried out a detailed study of the cluster sources with GMRT/WSRT at frequencies ranging from 153 MHz to 2.3 GHz. Our LOFAR observations have produced higher-sensitivity, deeper images than the existing images at equivalent frequencies. In this section, we only discuss the new results obtained using the LOFAR images. We discuss below the discrepancy in the Mach numbers of RN and RS that were derived from X-ray and radio data, the characteristics of the post shock emission in RN, the eastern relic R1, and the radio halo.

### 2.5.1 Radio spectrum derived Mach numbers

The underlying particle-acceleration physics of shock waves closely relates to the shock Mach number and the observed spectra (e.g. Blandford & Eichler 1987; Donnert et al. 2016; Kang & Ryu 2016):

$$\mathcal{M} = \sqrt{\frac{2\alpha_{\text{inj}} - 3}{2\alpha_{\text{inj}} + 1}}, \quad (2.4)$$

where the injection spectral index  $\alpha_{\text{inj}}$  is related to the power-law energy distribution of relativistic electrons ( $dN(p)/dp \propto p^{-\delta_{\text{inj}}}$ , where  $dN(p)$  is the electron number within momentum range  $p$  and  $p + dp$ ) via the relation  $\alpha_{\text{inj}} = -(\delta_{\text{inj}} - 1)/2$ . For a simple planar shock model (Ginzburg & Syrovatskii 1969) the injection index  $\alpha_{\text{inj}}$  is flatter than the volume-integrated spectral index  $\alpha_{\text{int}}$ ,

$$\alpha_{\text{inj}} = \alpha_{\text{int}} + 0.5. \quad (2.5)$$

However, recent DSA test-particle simulations by Kang (2015a,b) indicate that this approximation (Eq. 2.5) breaks down for spherically expanding shock waves, due to shock compression and the injection electron flux gradually decreasing as the shock speed reduces in time. In the following Subsec. 2.5.1 and 2.5.1 we will estimate Mach numbers for the northern and southern shocks using the injection spectral indices that are measured from integrated spectra and resolved spectral index maps.

#### Mach numbers from integrated spectra

Using LOFAR data, together with existing radio data (van Weeren et al. 2010; Stroe et al. 2013), we measured volume-integrated spectral indices of  $\alpha_{\text{int}}^n = -1.11 \pm 0.04$  for RN and of  $\alpha_{\text{int}}^s = -1.41 \pm 0.05$  for RS. From that we derived injection indices of  $\alpha_{\text{inj}}^n = -0.61 \pm 0.04$  and  $\alpha_{\text{inj}}^s = -0.91 \pm 0.05$  (Eq. 2.5) and Mach numbers of  $\mathcal{M}_n = 4.4_{-0.6}^{+1.1}$  and  $\mathcal{M}_s = 2.4 \pm 0.1$ . For  $\mathcal{M}_n$  our result is consistent with the findings of Stroe et al. (2013) ( $4.58 \pm 1.09$ , using colour-colour plots) and van Weeren et al. (2010) ( $4.6_{-0.9}^{+1.3}$ , using a 0.68 – 2.3 GHz spectral index map). However,  $\mathcal{M}_s$  is significantly smaller than that estimated in Stroe et al. (2013) ( $2.80 \pm 0.19$ ). Furthermore, there remains a discrepancy between the Mach numbers obtained from the integrated spectral index and those derived from X-ray data or spectral age modelling of radio data (Stroe et al. 2014; Akamatsu et al. 2015) (see Table 2.4).

### Mach numbers from spectral index maps

An alternative way to obtain the injection index is to measure it directly from the shock front region in high resolution spectral index maps. Unfortunately, the precise thickness of the region in which the relativistic electrons are (re-)accelerated by the shock is unknown. However, given that the bulk velocity is approximately 905 km/s in the downstream region (Stroe et al. 2014), the travel time for the electrons to cross a distance equivalent to the beam size of 6.5 arcsec (22.5 Myrs) is 4 – 10 times shorter than their estimated lifetime of 90 – 220 Myrs (assuming the relativistic electrons are in the magnetic field  $\sim \mu\text{G}$  and observed at the frequencies 150 – 610 MHz, see e.g. Donnert et al. 2016). Therefore, the shock (re-)accelerated relativistic electrons are not likely to lose a significant amount of their energy along the distance corresponding to the synthesized beam size; and the injection spectral index can be approximated from measurements at the shock front.

From the 6.5 arcsec-resolution spectral index map in Fig. 2.5, we found  $\alpha_{\text{inj}}^n = -0.81 \pm 0.11$  within the shock front regions in Fig. 2.9. This injection index corresponds to  $\mathcal{M}_n = 2.7_{-0.3}^{+0.6}$ , which is consistent with the X-ray and spectral age modelling derived Mach numbers (e.g.  $2.90_{-0.13}^{+0.10}$  in Stroe et al. 2014 and  $2.7_{-0.4}^{+0.7}$  in Akamatsu et al. 2015). A low Mach number like this may also be expected from structure formation simulations which typically have  $2 \lesssim \mathcal{M} \lesssim 4$  for internal shocks (Ryu et al. 2003; Pfrommer et al. 2006; Vazza et al. 2009). For RS, since the shock front location is detected furthest from the cluster centre in the 35 arcsec-resolution image (Fig. 2.12), we estimated the injection index from the lower-resolution map (see Fig. 2.9). We obtained an average value of the injection index of  $\alpha_{\text{inj}}^s = -1.23 \pm 0.22$  for RS. This is equivalent to a shock with Mach number of  $\mathcal{M}_s = 1.9_{-0.2}^{+0.3}$ . Similarly to RN, the Mach number for RS that is measured directly at the shock front location in our resolved spectral index maps is in agreement with those measured with X-ray data whereas the Mach number derived from the integrated spectral index is  $\sim 2\sigma$  higher. (e.g.  $\mathcal{M}_s^X = 1.7_{-0.3}^{+0.4}$  in Akamatsu et al. 2015, see table 2.4). It is noticed in Fig. 2.9 that the spectral indices along the shock front of RS have large variations from a minimum of  $-1.53 \pm 0.08$  (at 1.04 Mpc) to a maximum of  $-0.91 \pm 0.11$  (at 345 kpc), whereas the spectral indices at the shock front in RN remain approximately constant. Additionally, the spectral indices in the eastern side of RS (mean value of  $\bar{\alpha} = -1.04 \pm 0.12$ ) are flatter than those in the western side ( $\bar{\alpha} = -1.43 \pm 0.08$ ). This could imply that the southern shock propagated with different Mach numbers in different areas and that the

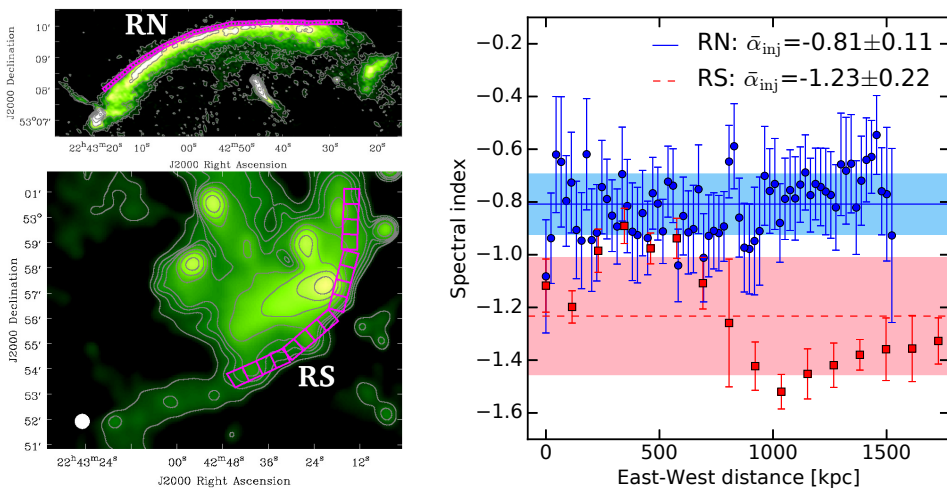


Figure 2.9: Spectral index profiles (right) for the flat spectrum regions of RN (top left) and RS (bottom left). The RN and RS profiles were extracted from the 145–608 MHz spectral index map (Fig. 2.5) and the 145 MHz – 2.3 GHz spectral index maps (Fig. 2.12, eight frequencies). The weighted means for RN ( $\bar{\alpha}_{\text{inj}}^r = -0.81 \pm 0.11$ ) and RS ( $\bar{\alpha}_{\text{inj}}^s = -1.23 \pm 0.22$ ) are plotted as horizontal lines (solid blue for RN and dashed red for RS). The errors of the weighted means are shown by the filled regions of the same colour.

shock travelled with a higher Mach number in the east. Another possibility is that due to the complex morphology of RS the regions, where the spectral indices were extracted, can host electron populations of different spectra along the line of sight.

### Measurement uncertainty

The estimation of the injection indices from the volume-integrated and spatially-resolved spectra both have pros and cons. Firstly, while the accuracy of the former method does not depend on the spatial resolution of the observations nor the orientation of the merger axis, it may be affected by other sources, since the radio-integrated fluxes are calculated within the large volume. This argument was invoked to explain Mach number discrepancies in several other cases (e.g. Ogorean et al. 2014b; Trasatti et al. 2015; Itahana et al. 2015). It is also very likely a contributing factor in the measurements of RS where contaminating radio sources are present. Similarly, for RN the integrated fluxes might be also contaminated in this case by additional compression in the post-shock region that we discussed in Subsec. 2.4.1. To quantify this possible contamination, we estimated

the integrated spectrum of RN masking out the affected compression region (Subsec. 2.4.1). We obtained  $\alpha''_{\text{int}} = -1.08 \pm 0.04$  and  $\mathcal{M}_n = 5.1_{-0.9}^{+2.0}$  which is a higher Mach number than we obtained prior to removing the potentially contaminated region. Therefore, this potential contamination cannot explain the Mach number discrepancy. Secondly, as mentioned earlier, the  $\alpha_{\text{inj}} - \alpha_{\text{int}}$  relation (Eq. 2.5) does not hold for spherically expanding shock waves such as RN and RS (Kang 2015a,b). Therefore, the volume-integrated spectra will not necessarily characterise the large-scale spherical shocks. This reason was used to explain the discrepancy of the radio and X-ray derived Mach numbers in the Toothbrush cluster (van Weeren et al. 2016c). Thirdly, the discrepancy might also come from micro-physics of the dynamics of relativistic particles, including diffusion across magnetic filaments, re-acceleration due to the interaction of CRs with magnetic field perturbations, adiabatic expansion and changes of the magnetic field strength in the downstream region (e.g. Donnert et al. 2016).

The injection indices that are directly estimated from spatially resolved spectral index maps might be less susceptible to contamination from embedded sources. However, for such measurements to be accurate it requires (i) the merger axis to be on/close to the plane of the sky to avoid the mixture of electron populations of different velocities along the line of sight, (ii) highly-resolved spectral index maps to minimise the convolution effect caused by the synthesised beam as this would artificially bias the injection indices, and (iii) precise alignment among the radio maps. In the case of CIZA2242, hydrodynamical binary-merger simulations by van Weeren et al. (2011a) suggested that the merger axis is likely to be close to the plane of the sky (less than  $10^\circ$ ), and this was supported by Kang et al. (2012) who performed DSA simulations. Moreover, the surface brightness along the width of the eastern side of RN (Fig. 2.7, red curve) drops to 10% of the peak value at a distance of  $\sim 130$  kpc from the peak which is consistent with the simulated profiles with a small viewing angle in van Weeren et al. (2011a). This implies that RN satisfies (i). However, due to the complex morphology of RS, the southern shock might be observed at a larger angle than the northern shock. To assess the impact of (ii), we calculated the injection indices at various spatial resolutions for RN. We made spectral index maps between 145 and 608 MHz at resolutions 6.5 arcsec, 15 arcsec, 30 arcsec and 45 arcsec. The injection indices were measured at the shock-front and the sizes of the square regions used to extract the injection index are approximately equal to the beam size of the maps (see Fig. 2.9). We found that although the apparent injection locations are slightly shifted to the North for the lower-resolution

Table 2.4: Spectral indices and Mach numbers for the shock waves.

Source	RN	RS	R1
$\alpha_{\text{inj}}$	$-0.81 \pm 0.11$	$-1.23 \pm 0.22$	$-0.91 \pm 0.14$
$\alpha_{\text{int}}$	$-1.11 \pm 0.04$	$-1.41 \pm 0.05$	$-1.18 \pm 0.06$
$\mathcal{M}_{\text{inj}}$	$2.7^{+0.6}_{-0.3}$	$1.9^{+0.3}_{-0.2}$	$2.4^{+0.5}_{-0.3}$
$\mathcal{M}_{\text{int}}^e$	$4.4^{+1.1}_{-0.6}$	$2.4^{+0.1}_{-0.1}$	$3.5^{+0.7}_{-0.4}$
$\mathcal{M}^X$	$2.7^{+0.7}_{-0.4}{}^a$	$1.7^{+0.4}_{-0.3}{}^a$	$2.5^{+0.6}_{-0.2}$
$\mathcal{M}_{\text{ref}}$	$4.6^{+1.3}_{-0.9}{}^b$ , $4.58^{+1.09}_{-1.09}{}^c$ , $2.90^{+0.10}_{-0.13}{}^d$	$2.80^{+0.19}_{-0.19}{}^c$	N/A

Notes:  $^a$ : Akamatsu et al. (2015),  $^b$ : van Weeren et al. (2010),  $^c$ : Stroe et al. (2013),  $^d$ : Stroe et al. (2014),  $^e$ : using Eq. 2.4 and 2.5.

maps, the values of the injection indices are weakly affected by the spatial resolution (see Fig. 2.10). Assuming a linear relation between  $\alpha_{\text{inj}}$  and resolution  $\theta$ , we found  $\alpha_{\text{inj}}^n = (-0.81 \pm 0.10) + (-0.63 \pm 2.78) \times 10^{-3}\theta[\text{arcsec}]$ , which is consistent with the value of  $\alpha_{\text{inj}}^n = -0.81 \pm 0.11$  that we found in the 6.5 arcsec-resolution map (Fig. 2.9). To account for (iii), we aligned the radio images when making spectral index maps using the procedure described in Subsec. 2.3.4. The GMRT 608 MHz image was shifted a distance of 0.20 arcsec and 0.01 arcsec in RA and Dec axes, respectively. We found a small increase of 1% in the Mach number when aligning the images.

A potential further complication is that X-ray derived Mach numbers also suffer from several systematic errors. As discussed in Akamatsu et al. (2017) (see Sect. 4.3 of their paper), there are three main systematics, which prevents proper Mach number estimation from X-ray observations: (i) the projection effect, (ii) inhomogeneities in the ICM, and (iii) ion-electron non-equilibrium situation after the shock heating. In case of CIZA2242, the first point was already discussed above. Related to point (ii), van Weeren et al. (2011a) revealed that it is less likely to be a large clumping factor because of the smooth shape of the relic. The third point would lead to the underestimation of the Mach numbers from X-ray observations. However, it is difficult to investigate this systematic without better spectra than those from the current X-ray spectrometer. The upcoming Athena satellite can shed new light on this point.

## 2.5.2 Particle acceleration efficiency

The northern relic is known as one of the most luminous radio relics so far. But the low Mach number of  $\mathcal{M}_n = 2.7^{+0.6}_{-0.3}$  for RN (Subsec. 2.5.1) leads us

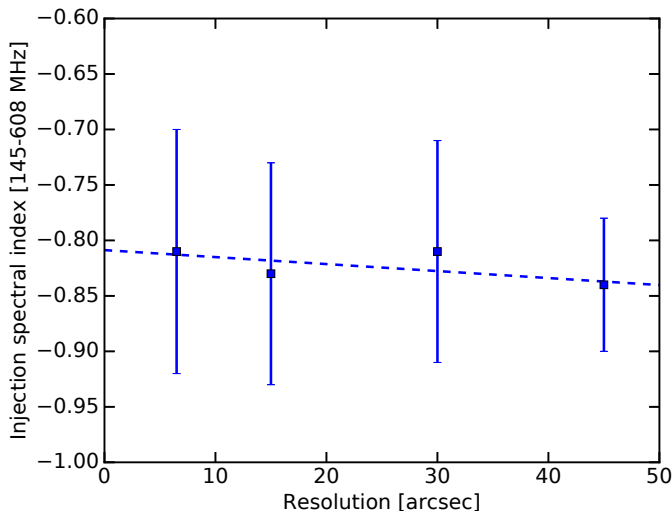


Figure 2.10: Injection spectral indices between 145 and 608 MHz of RN as measured at various spatial resolutions ( $\alpha_{\text{inj}} = -0.81 \pm 0.63 \times 10^{-3} \theta_{[\text{arcsec}]}$ ). The regions where the indices were extracted are similar to those in Fig. 2.9.

to a question of acceleration efficiency that is required to explain such a luminous relic via shock acceleration of thermal electrons. The acceleration efficiency was defined as the fraction of the kinetic energy flux available at the shock that is converted into the supra-thermal and relativistic electrons (van Weeren et al. 2016c),

$$\eta_e = \frac{\epsilon_{e, \text{down}} v_{\text{down}}}{\Delta F_{\text{KE}}}, \quad (2.6)$$

where  $\epsilon_{e, \text{down}}$  and  $v_{\text{down}}$  are the energy density and the velocity of the downstream accelerated electrons, respectively;  $\Delta F_{\text{KE}} = 0.5 \rho_{\text{up}} v_{s, \text{up}}^3 \left(1 - \frac{1}{C^2}\right)$  is the kinetic energy available at the shock; here  $\rho_{\text{up}}$  and  $v_{s, \text{up}}$  are the upstream density and the shock speed, respectively;  $C = \mathcal{M}^2(\gamma+1)/[2+(\gamma-1)\mathcal{M}^2]$ , here  $\gamma$  is the adiabatic index of the gas and  $\mathcal{M}$  is the shock Mach number. Following formula in Botteon et al. (2016b)<sup>3</sup>, in Fig. 2.11 we report the efficiency of particle acceleration by the northern shock as a function of the magnetic field for the Mach number of  $\mathcal{M}_n = 2.7_{-0.3}^{+0.6}$  ( $\alpha_{\text{inj}} = -0.81 \pm 0.11$ ). We plotted the  $1\sigma$  curves where  $\mathcal{M}_n = 2.4$  ( $\alpha_{\text{inj}} = -0.92$ , upper dashed) and  $\mathcal{M}_n = 3.3$  ( $\alpha_{\text{inj}} = -0.70$ , lower dashed), corresponding to the  $1\sigma$  lower and upper boundaries, respectively. The magnetic field range ( $\lesssim 20 \mu\text{G}$ ) was

<sup>3</sup>note that the left-hand side of Eq. 5 in Botteon et al. (2016b) should be  $1/\Psi$ .



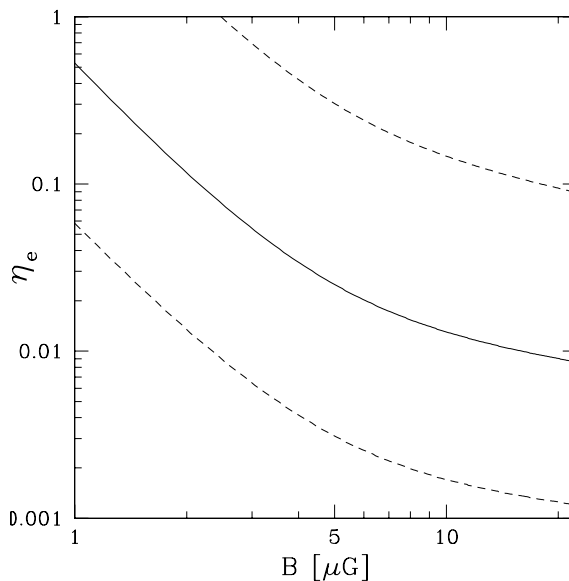


Figure 2.11: Particle acceleration efficiency as a function of magnetic field for the northern relic. The solid curve is estimated for the Mach number of  $\mathcal{M}_n = 2.7$  ( $\alpha_{\text{inj}} = -0.81$ ). The dashed curves are the  $1\sigma$  uncertainties; the upper and lower dashed curves are for the  $\mathcal{M}_n = 2.4$  ( $\alpha_{\text{inj}} = -0.92$ ) and  $\mathcal{M}_n = 3.3$  ( $\alpha_{\text{inj}} = -0.70$ ) limits, respectively.

selected to cover the values,  $5 - 7 \mu\text{G}$ , in van Weeren et al. (2010). The relatively high efficiency of electron acceleration that should be postulated to explain the relic challenges the case of a shock with  $\mathcal{M}_n < 2.7$ . In this case a population of pre-existing relativistic electrons in the upstream region of the shock should be assumed. However, in the DSA framework, it is still possible to accelerate electrons to relativistic energies directly from thermal pools in the case of  $\mathcal{M}_n > 2.7$ . Future works will provide more constraints on this point.

### 2.5.3 The radio halo

#### The spatial spectral variations

In Fig. 2.3 we show our LOFAR detection of the large-scale diffuse emission that connects RN and RS. This was previously reported in the WSRT 1.4 GHz observations and was interpreted as a radio halo by van Weeren et al. (2010). However, its physical characteristics, such as its flux and spectral index, have not been studied. With our deep LOFAR image (Fig. 2.3), we

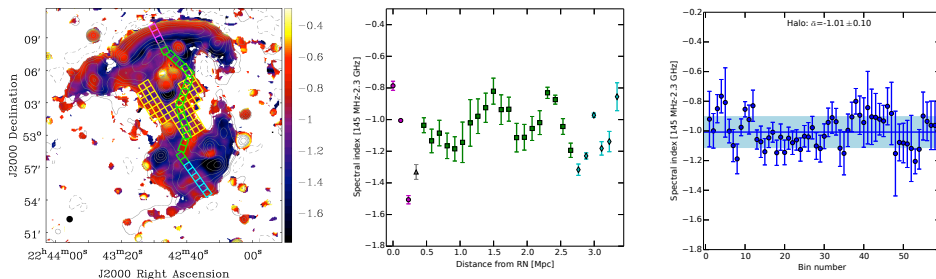


Figure 2.12: Left: A 35 arcsec-resolution spectral index map between 145 MHz and 2.3 GHz (eight frequencies) including the regions where spectral indices were extracted. The square regions have a width of 36 arcsec (115 kpc). In the analysis of the spectral index variations, we did not take into account an absolute flux scale uncertainty of 10% as done for the 6.5 arcsec and 18 arcsec  $\times$  16 arcsec maps in Fig. 2.5 and 2.8, respectively. Middle: Spectral index profile for the square (magenta, gray, green, cyan) regions in the left image. Right: The spectral indices in the square yellow regions over the selected radio halo area where the contamination from radio galaxies is minimised. The inverse-invariance weighted mean of the spectral indices for the halo regions (yellow squares) is  $-1.01 \pm 0.10$ .

estimated the halo size within the  $3\sigma_{\text{noise}}$  region to be  $1.8 \text{ Mpc} \times 830 \text{ kpc}$  and the integrated flux to be  $S_h = 346 \pm 64 \text{ mJy}$  (see Subsec. 2.4.4). The halo size in the north-south direction was measured between the northern and southern relic inner edges. The halo maintains its surface brightness, even in the regions that are least contaminated by the tailed AGNs, such as the regions east of source D or west of source E. The presence of the halo with elongated morphology connecting the north and south relics suggests a connection between the shock waves that are responsible for RN and RS. A comparable example of the morphological connection between radio relic and halo was observed in RX J0603.3+4214 where a giant radio relic at the northern edge of the cluster is connected to an elongated uniform brightness radio halo in the cluster centre (van Weeren et al. 2016c).

We examined a spectral index profile (see Fig. 2.12, middle) across the north and south relics and the radio halo. We found that the spectral index steepens from  $-0.79 \pm 0.09$  at the northern shock front location to  $-1.51 \pm 0.08$  in the post-shock region (230 kpc). It then flattens over a distance of 115 kpc and remains approximately constant with a mean of  $-1.03 \pm 0.12$  over a distance of 2.5 Mpc. This mean spectral index of the halo is  $-1.01 \pm 0.10$  when measured in a  $\sim 1 \text{ Mpc}^2$  region (i.e. yellow squares in Fig. 2.12, left) and is consistent with the integrated spectral index of  $-1.03 \pm 0.09$  that was estimated in Subsec. 2.4.4. Similarly, the spectral index profile across RS

in the south-north direction (i.e. right-left direction in Fig. 2.12, middle) steepens from  $-0.86 \pm 0.08$  at the southern shock front to  $-1.32 \pm 0.05$  over a distance of 575 kpc from the southern shock front (cyan diamonds at  $\sim 2.7$  Mpc in Fig. 2.12, middle). After this steepening, the spectral indices flatten to  $-0.83 \pm 0.05$  over a distance of 460 kpc (i.e. 2.2 – 2.7 Mpc in Fig. 2.12, middle). However, it is possible that the spectral indices across RS and in the southern halo region are strongly effected by contaminating sources (i.e. K, J). Moreover, the spectral index variations in this area are at similar levels to those seen across the halo and therefore cannot be associated with the southern shock with certainty.

The spectral re-flattening of the emission downstream from the northern relic and into the northern part of the halo suggests particles have undergone re-acceleration. It is currently thought that giant radio halos trace turbulent regions in which particles are re-accelerated (see Brunetti & Jones 2014 for review). The fact that in several cases X-ray shocks coincide with edges of radio halos is suggestive of the possibility that these shocks can be sources of turbulence downstream (e.g. Markevitch 2010; Shimwell et al. 2014). More specifically shocks may inject compressive turbulence in the ICM and compressive turbulence is in fact used to model turbulent re-acceleration of electrons in radio halos in several papers (e.g. Brunetti & Lazarian 2007). In the case of CIZA2242 the electrons might be accelerated (or re-accelerated) at the northern shock front and lose energy downstream via radiative losses. However on longer times the shock-generated turbulence might decay to smaller scales and re-accelerate electrons inducing a flattening of the synchrotron spectrum. A similar scenario was invoked to explain the spatial behaviour of the spectral index in the post-shock region of RX J0603.3+4214 and the hole in the radio halo of Abell 2034 (van Weeren et al. 2016c and Shimwell et al. 2016). In RX J0603.3+4214, van Weeren et al. (2016c) also observed spectral steepening in the post-shock region from  $-0.8$  at the shock front edge to  $-2$  at the boundary of the relic and halo, which was followed by an approximately constant spectral index of  $-1.06 \pm 0.06$  across the Mpc-scale halo region. This suggests that in these, and potentially other clusters, we may be observing similar particle (re-)acceleration and ageing scenario.

The spectral indices over the large region of the radio halo, where the contaminating sources (i.e. B, C, D, E, F, G, K, I) are masked, are plotted in Fig. 2.12 (right). Following Cassano et al. (2013), we estimated the raw scatter (see Eq. 5 in Cassano et al. 2013) from the inverse-variance weighted mean to be 0.10. From the weighted mean of the spectral index errors of

0.10 unit that propagates from the image noise, the intrinsic scatter of  $\sqrt{0.10^2 - 0.09^2} = 0.04$  was obtained. The intrinsic scatter is smaller than the typical spectral index errors of  $\Delta\alpha \approx 0.13$  in the halo region (yellow squares in Fig. 2.12, left); hence, the measurements of the spectral indices in the halo region are close to the detection limit of our data. More precise spectral index measurements would therefore be required to study the physics of turbulence in the halo.

### A comparison with radio-thermal correlations

Galaxy clusters statistically branch into two populations (Brunetti et al. 2007, 2009; Rossetti et al. 2011; Cassano et al. 2013; Cuciti et al. 2015; Yuan et al. 2015): dynamically disturbed systems host radio halos whose luminosity correlates with the X-ray luminosity and mass of the hosting systems, whereas in general relaxed systems do not host Mpc-scale halos at the sensitivity level of available observations. To examine whether or not the radio halo of CIZA2242 follows the relationship between radio luminosity and X-ray luminosity and mass of the hosting cluster, in Fig. 2.13 we plot the radio power  $P_{1.4\text{GHz}}$  versus the X-ray luminosity  $L_{500}$  in the 0.1–2.4 keV energy band for a number of clusters that are given in Cassano et al. (2013);  $L_{500}$  is the luminosity within the radius  $R_{500}$  where the ICM matter density is 500 times the critical density of the Universe at redshift  $z$ . The radio power at 1.4 GHz for the CIZA2242 halo was estimated by extrapolating our measurements to be  $P_{1.4\text{GHz}} = (3.5 \pm 1.0) \times 10^{24} \text{ W Hz}^{-1}$  at the cluster redshift  $z = 0.192$  using the LOFAR 145 MHz integrated flux of  $346 \pm 64$  mJy and the integrated spectral index of  $-1.03 \pm 0.09$ . Using the Chandra data (Ogrea et al. 2014a), we measured the X-ray luminosity of  $L_{500} = (7.7 \pm 0.1) \times 10^{44} \text{ erg s}^{-1}$  for the 0.1–2.4 keV energy band within a radius of  $R_{500} = 1.2$  Mpc at  $z = 0.192$ . Fig. 2.13 shows that the CIZA2242 data point closely follows the  $P_{1.4\text{GHz}} - L_{500}$  correlation (i.e.  $P_{1.4\text{GHz}} [10^{24} \text{ W Hz}^{-1}] = 10^{-1.52 \pm 0.20} L_{500}^{2.11 \pm 0.20} [10^{44} \text{ erg s}^{-1}]$ ; BCES bisector best fit in Cassano et al. 2013).

Despite RN being amongst the most prominent radio relics known, the radio halo of CIZA2242 seems typical, with moderate radio power and X-ray luminosity in comparison with other radio halos (Fig. 2.13). Magneto-hydrodynamic simulations of re-acceleration of relativistic electrons via post-shock generated turbulence by Donnert et al. (2013) predict that the integrated spectrum of the halos is flatter in their early phase ( $\lesssim 1$  Gyr) and becomes steeper after  $\sim 1.2$  Gyrs of core passage. With our current data, the radio halo of CIZA2242 has a relatively flat spectral index of  $-1.03 \pm 0.09$

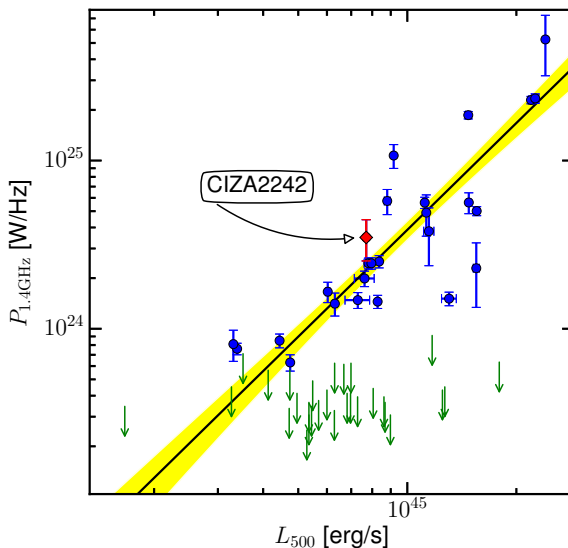


Figure 2.13: The scaling relation of the radio power  $P_{1.4\text{GHz}}$  and X-ray luminosity  $L_{500}$  for radio halos including CIZA2242 (red diamond). The list of the halos and the BCES bisector best fit  $P_{1.4\text{GHz}}[10^{24}\text{WHz}^{-1}] = 10^{-1.52 \pm 0.21} \times L_{500}^{2.11 \pm 0.20} [10^{44}\text{erg s}^{-1}]$  (without CIZA2242) were given in Cassano et al. (2013). The shadowed area is the 95% confidence regions of the best-fit relation.

and is among the flatter spectrum halos known (e.g. Feretti et al. 2012), implying that it has recently formed (e.g. also see our discussion in Subsec. 2.5.3). The early phase of the halo is further supported by binary cluster merger simulations by van Weeren et al. (2011a) which suggested that the cluster is 1 Gyr after core passage.

#### 2.5.4 A newly detected eastern shock wave?

The steepening features in the spectral index of R1, reported in Subsec. 2.4.3, are likely due to the energy losses of relativistic electrons (e.g. synchrotron, IC emission). Additionally, the intensity maps (Fig. 2.1, 2.8 and 2.14, left) show emission with a sharp edge on the eastern side and a more gradual decline towards the western edge. These features are among the typical properties of radio emission associated with a shock wave. We speculate that R1E and R1W trace a complex shock wave that is propagating away from the cluster centre and that this shock (re-)energises two clouds of relic or aged electrons. In this scenario, the spectral steepening is more visible for R1E which implies that the shock wave is more on the plane of the

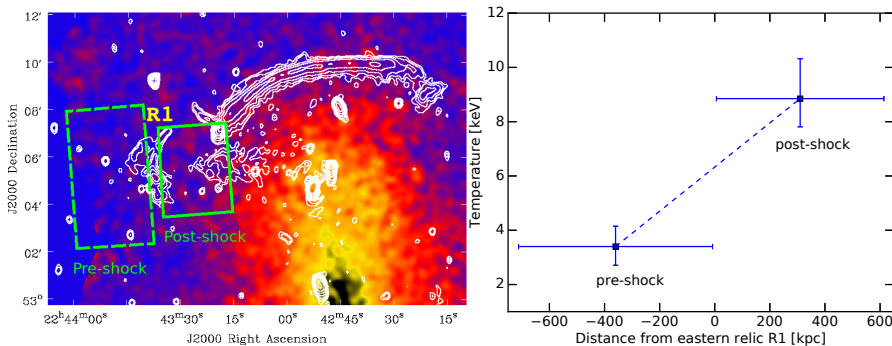


Figure 2.14: Left: Suzaku X-ray image for the north-east region of CIZA2242 overlaid with the WSRT 1.4 GHz contours (the first contour is  $3\sigma_{\text{noise}}$ ,  $\sigma_{\text{noise}} = 30 \mu\text{Jy}/\text{beam}$ , beam size of  $14 \text{ arcsec} \times 11 \text{ arcsec}$ , and the next ones are spaced by 2.) The green rectangles are the pre- and post-shock regions of R1 within which the X-ray temperatures were extracted. Right: X-ray temperature for the corresponding regions in the left image.

sky in this region.. A 12 arcsec resolution map in Fig. 2.15 shows a bridge of low surface brightness (a  $3\sigma_{\text{noise}}$  detection) that connects R1, R2, I, and RN. This suggests the origin of the eastern shock may be closely related to the cluster major merger. On our  $18 \text{ arcsec} \times 16 \text{ arcsec}$  resolution map (Fig. 2.8, right) we measured the injection indices of  $-0.89 \pm 0.08$  for R1E and  $-0.92 \pm 0.12$  for R1W, the average of these injection indices is  $-0.91 \pm 0.14$  which is equivalent to a Mach number of  $2.4^{+0.5}_{-0.3}$ . Our estimation of the integrated spectral index of R1, within the LOFAR  $> 3\sigma_{\text{noise}}$  region, masking out the compact source in the central of R1W, is  $-1.18 \pm 0.06$ . This is equivalent to a shock Mach number of  $3.5^{+0.7}_{-0.4}$ . Similarly to RN and RS, this Mach number is higher than the value that was calculated from the high resolution spectral index map.

To search for imprints of a shock in the X-ray data, we re-analysed the Suzaku data (Akamatsu et al. 2015) in the pre- and post-shock regions of R1 (see Fig. 2.14). We found an average temperature jump from  $kT_{\text{pre}} = 3.5^{+0.8}_{-0.5} \text{ keV}$  to  $kT_{\text{post}} = 9.6^{+1.5}_{-1.1} \text{ keV}$  from the pre- to post-shock region. This temperature jump of 6.1 keV across the eastern relic is 2.4 times higher than a temperature decrease of  $\sim 2.5 \text{ keV}$  over the eastern, slightly south region (i.e. centred at RA=22:43:24, DEC=+52:57.00) that is at a similar radial distance as the eastern relic but is devoid of radio emission (see Fig. 6 and 7 in Akamatsu et al. 2015). Therefore, the high temperature jump (6.1 keV) is likely associated with the eastern relic. This X-ray temperature jump corresponds to a Mach number of  $2.5^{+0.6}_{-0.2}$ , which is consistent with our

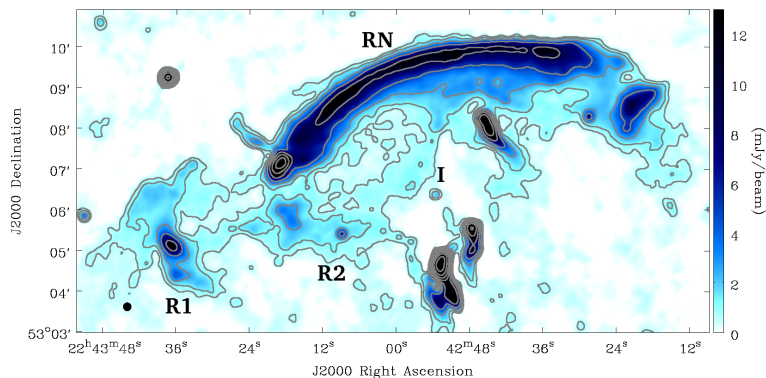


Figure 2.15: A zoom-in northern region of the LOFAR intensity image at 12 arcsec resolution. The first contour is at  $3\sigma_{\text{noise}}$  ( $\sigma_{\text{noise}} = 210 \mu\text{Jy}/\text{beam}$ ); the next ones is spaced by 2.

radio derived Mach numbers. The X-ray detection of a shock wave could be confirmed by measuring the discontinuity of the X-ray surface brightness profile. However, the existing Chandra and XMM-Newton data (Ogrea et al. 2013a, 2014a; Akamatsu et al. 2015) do not have sufficient spatial coverage to detect the surface brightness discontinuity at the location of the eastern relic; and the Suzaku data has a limited spatial resolution of  $2'$  which is insufficient for the surface brightness analysis. Our collection of radio and X-ray measurements provides compelling evidence that R1 is tracing another shock front in CIZA2242 that is propagating eastwards.

## 2.6 Conclusions

We have presented deep, high-fidelity LOFAR 145MHz images of CIZA2242, which have a resolution of  $\sim 5$  arcsec and a sensitivity of  $140 \mu\text{Jy}/\text{beam}$ . The LOFAR data, in combination with the existing GMRT, WSRT, Suzaku and Chandra data were used to create spectral index maps of CIZA2242 at resolutions of 6.5 arcsec,  $18 \text{ arcsec} \times 16 \text{ arcsec}$  and 35 arcsec. Below we summarise our main results.

- To investigate the long-standing discrepancy between X-ray and radio derived Mach numbers, we have measured injection spectral indices of  $-0.81 \pm 0.11$  and  $-1.23 \pm 0.22$  for the northern and southern relics, respectively. These correspond to Mach numbers of  $\mathcal{M}_n = 2.7^{+0.6}_{-0.3}$  and  $\mathcal{M}_s = 1.9^{+0.3}_{-0.2}$ , and are in agreement with the Mach numbers derived

from X-ray data (e.g.  $\mathcal{M}_n = 2.7_{-0.4}^{+0.7}$  and  $\mathcal{M}_s = 1.7_{-0.3}^{+0.4}$  in Akamatsu et al. 2015) and spectral age modelling study of the radio emission (e.g.  $\mathcal{M}_n = 2.9_{-0.13}^{+0.10}$  in Stroe et al. 2014).

- We have confirmed the existence of a radio halo and constrained its integrated flux ( $346 \pm 64$  mJy) and its integrated spectral index ( $-1.03 \pm 0.09$ , between 145 MHz and 2.3 GHz). We measured the radio halo power  $P_{1.4\text{GHz}} = (3.5 \pm 1.0) \times 10^{24} \text{ W Hz}^{-1}$  and the X-ray luminosity  $L_{500} = (7.7 \pm 0.1) \times 10^{44} \text{ erg s}^{-1}$ , which is close to the value expected from the  $P_{1.4\text{GHz}}-L_{500}$  correlation. We have discussed a possible connection between the northern and southern relics and the halo, and have speculated that the formation of the halo may be driven by turbulence generated by the passing shock waves.
- In the radio source R1, in the north eastern region of the cluster, we found spectral steepening towards the cluster centre. A temperature jump from  $3.5_{-0.5}^{+0.8}$  keV to  $9.6_{-1.1}^{+1.5}$  keV was also detected at the location of the eastern relic R1 by re-analysing the existing Suzaku X-ray data. We suggest that R1 is an eastern relic that traces a shock wave that is propagating eastwards and (re-)energises the ICM electrons. We estimated an injection spectral index of  $-0.91 \pm 0.14$  and a Mach number of  $\mathcal{M}_e = 2.4_{-0.3}^{+0.5}$ , which is consistent with our re-analysis of the Suzaku data from which we derived  $\mathcal{M}_e^X = 2.5_{-0.2}^{+0.6}$ .

## Acknowledgements

We thank the anonymous referee for the helpful comments. This paper is based (in part) on results obtained with LOFAR equipment. LOFAR (Haarlem et al. 2013) is the Low Frequency Array designed and constructed by ASTRON. We thank the staff of the GMRT who have made these observations possible. The GMRT is run by the National Centre for Radio Astrophysics of the Tata Institute of Fundamental Research. The Westerbork Synthesis Radio Telescope is operated by the ASTRON (Netherlands Institute for Radio Astronomy) with support from the Netherlands Foundation for Scientific Research (NWO). The scientific results reported in this article are based in part on observations made by the Chandra X-ray Observatory and published previously in Ogreaan et al. (2014a). This research has made use of data obtained from the Suzaku satellite, a collaborative mission between the space agencies of Japan (JAXA) and the USA (NASA). DNH, TS and HR acknowledge support from the ERC Advanced



Investigator programme NewClusters 321271. DDM acknowledges support from ERCStG 307215 (LODESTONE). GB and RC acknowledge partial support from PRIN INAF 2014 and JD acknowledges support from ERC Marie-Curie Grant 658912 (Cosmo Plasmas). GJW gratefully acknowledges support from The Leverhulme Trust. HA acknowledges the support of NWO via a Veni grant. SRON is supported financially by NWO, the Netherlands Organization for Scientific Research. MB and MH acknowledge support by DFG FOR 1254. AD acknowledges support by BMBF 05A15STA. We thank G. A. Ogrean for providing us the Chandra map of CIZA2242. We thank M. James Jee for discussion on the weak lensing mass of CIZA2242.

## Appendices

### A Integrated fluxes for the radio relics and halo

Table 5 shows the integrated fluxes for the radio relics and halo in CIZA2242 that are plotted in Fig. 2.6. Note that the integrated fluxes for RN were reported in Stroe et al. (2015b); here we present the integrated fluxes from the images that were made with different CLEANing parameters (see Table 2.2).

### B Spectral index error maps

In Fig. 16, we show the error maps for the corresponding spectral index maps in Fig. 2.5, 2.8 and 2.12. The error estimation takes into account the individual image noise and a flux scale error of 10%, which is formulated in Eq. 2.2.

### C Eastern region of RS

A zoom-in optical image of the eastern region of RS is presented in Fig. 17.

Table 5: Integrated fluxes for the radio relics and halo in CIZA2242 in Fig. 2.6. The integrated fluxes for the relics were measured from the 18 arcsec  $\times$  16 arcsec images, and the halo fluxes were estimated from the 35 arcsec images (see Table 2.2 for imaging parameters). The flux measurement errors for the relics were added absolute flux scale uncertainties of 10% of the integrated fluxes. The flux error estimation for the radio halo was described in Subsec. 2.4.4.

Freq. (MHz)	RN (mJy)	RS (mJy)	Halo (mJy)	R1 (mJy)	R2 (mJy)
145	$1637 \pm 168$	$777 \pm 82$	$346 \pm 64$	$144 \pm 17$	$143 \pm 16$
153	$1488 \pm 171$	$711 \pm 93$	$288 \pm 64$	$76 \pm 20$	$122 \pm 24$
323	$646 \pm 71$	$193 \pm 25$	$-^a$	$38 \pm 7$	$20 \pm 5$
608	$337 \pm 35$	$83 \pm 9$	$59 \pm 20$	$16 \pm 2$	$29 \pm 3$
1221	$148 \pm 16$	$30 \pm 4$	$28 \pm 10$	$13 \pm 2$	$16 \pm 2$
1382	$140 \pm 14$	$34 \pm 4$	$43 \pm 10$	$10 \pm 1$	$15 \pm 2$
1714	$106 \pm 11$	$22 \pm 3$	$27 \pm 8$	$6 \pm 1$	$8 \pm 1$
2272	$72 \pm 8$	$17 \pm 2$	$19 \pm 6$	$4 \pm 1$	$8 \pm 1$

Notes:  $^a$ : a flux of 135 mJy was measured in the LOFAR  $\geq 3\sigma_{\text{noise}}$  region of the GMRT 323 MHz 35 arcsec map. However, most of the flux comes from the residuals of the subtracted compact sources. We excluded the halo flux at the 323 MHz in the integrated spectral index estimation.

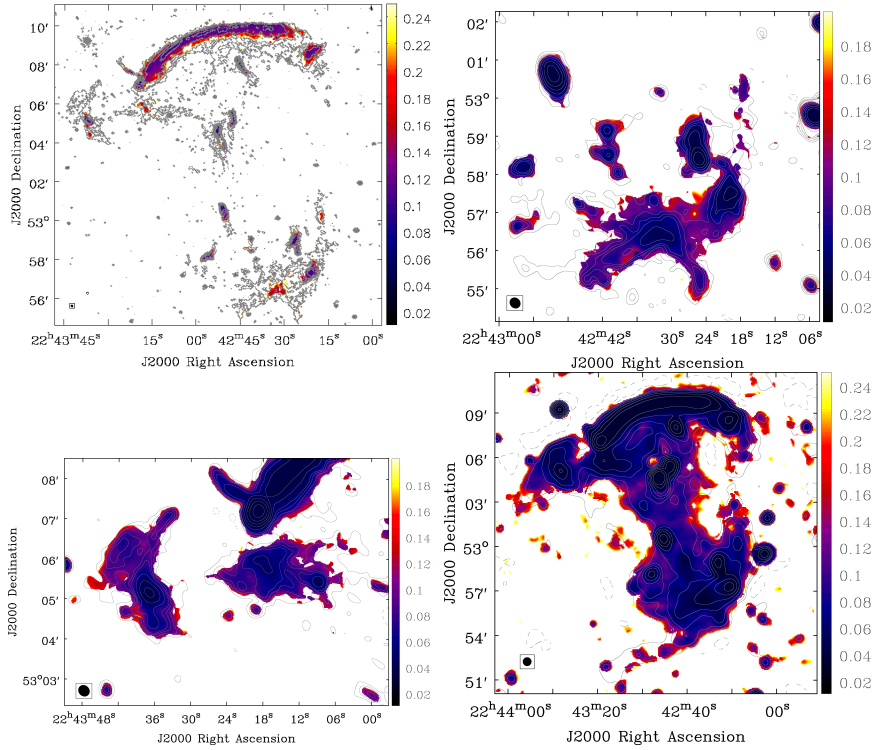


Figure 16: From left to right, top to bottom: The corresponding spectral index error maps for Fig. 2.5, 2.8 (left-right), and 2.12.

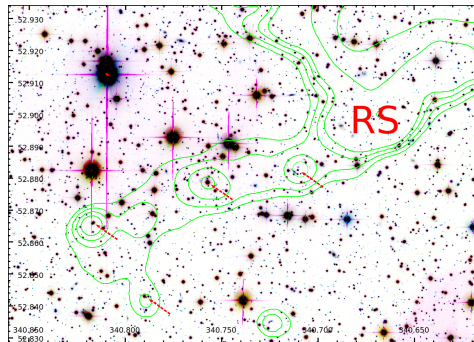


Figure 17: Optical image (Subaru *g* and *i* bands and CFHT*r* band, Stroe et al. 2015a; Jee et al. 2015) in the eastern side of RS. Four optical counterparts (red arrows) are detected at the locations of the radio emission peaks. The 35 arcsec-resolution radio emission contours are levelled at  $[3, 4, 5, 6, 12, 24] \times \sigma_{\text{noise}}$ .

# 3 | Radio observations of the double-relic galaxy cluster Abell 1240

## Abstract

We present LOFAR 120–168 MHz images of the merging galaxy cluster Abell 1240 that hosts double radio relics. In combination with the GMRT 595–629 MHz and VLA 2–4 GHz data, we characterised the spectral and polarimetric properties of the radio emission. The spectral indices for the relics steepen from their outer edges towards the cluster centre and the electric field vectors are approximately perpendicular to the major axes of the relics. The results are consistent with the picture that these relics trace large-scale shocks propagating outwards during the merger. Assuming diffusive shock acceleration (DSA), we obtain shock Mach numbers of  $\mathcal{M} = 2.4$  and  $2.3$  for the northern and southern shocks, respectively. For  $\mathcal{M} \lesssim 3$  shocks, a pre-existing population of mildly relativistic electrons is required to explain the brightness of the relics due to the high ( $> 10$  per cent) particle acceleration efficiency required. However, for  $\mathcal{M} \gtrsim 4$  shocks the required efficiency is  $\gtrsim 1\%$  and  $\gtrsim 0.5\%$ , respectively, which is low enough for shock acceleration directly from the thermal pool. We used the fractional polarization to constrain the viewing angle to  $\geq 53 \pm 3^\circ$  and  $\geq 39 \pm 5^\circ$  for the northern and southern shocks, respectively. We found no evidence for diffuse emission in the cluster central region. If the halo spans the entire region between the relics ( $\sim 1.8$  Mpc) our upper limit on the power is  $P_{1.4 \text{ GHz}} = (1.4 \pm 0.6) \times 10^{23} \text{ W Hz}^{-1}$  which is approximately equal to the anticipated flux from a cluster of this mass. However, if the halo is smaller than this, our constraints on the power imply that the halo is underluminous.

D. N. Hoang, T. W. Shimwell, R. J. van Weeren, et al.,  
MNRAS, 478, 2218 (2018)

### 3.1 Introduction

Massive galaxy clusters consist of hundreds to thousands of galaxies and grow hierarchically through a sequence of mergers of smaller clusters or groups of galaxies. Merging events between massive clusters release an enormous amount of gravitational energy ( $\sim 10^{63} - 10^{64}$  ergs) to the intra-cluster medium (ICM) over a few Gyrs (e.g. Hoeft et al. 2008; Brunetti & Jones 2014). Most of this energy is transferred to thermal energy by heating of the ICM plasma. Through large-scale motions (i.e. shocks and turbulence) and magnetic field amplification, a small fraction of it is converted to non-thermal energy of relativistic particles that permeate the ICM. In the presence of the large-scale,  $\sim \mu\text{G}$  cluster magnetic field, these relativistic electrons, that have a Lorentz factor  $\sim 10^3 - 10^5$ , emit synchrotron emission that is observable in the radio band (see, e.g., Blandford & Eichler 1987; Feretti et al. 2012; Brunetti & Jones 2014).

Depending on the morphology, location and polarimetric properties, the diffuse radio sources in galaxy clusters are primarily classified as radio haloes or relics. Radio relics are elongated diffuse sources observed at the periphery of galaxy clusters; some relics have been detected with a high fraction of linear polarization at  $\sim \text{GHz}$  frequencies (i.e. from  $\sim 10\%$  up to  $70\%$ ) and distinctive spectral index gradients across their structure. Radio haloes are cluster-wide sources that roughly follow the X-ray emission and are observed to be unpolarized down to a few percent (see, e.g., Feretti et al. 2012; Kierdorf et al. 2017).

The formation mechanism of radio haloes and relics has not been fully understood. The prominent model for the generation of radio haloes is the turbulent re-acceleration model where relativistic electrons are re-energized by magnetohydrodynamical turbulence during cluster mergers (Brunetti et al. 2001; Petrosian 2001). Another model has been proposed to explain the existence of radio haloes such as the hadronic model in which relativistic electrons are secondary products of proton-proton collisions (e.g. Dennison 1980). However, the secondary model has difficulties because of the non-detection of  $\gamma$ -rays by the Fermi  $\gamma$ -ray Space Telescope (e.g. Jeltama et al. 2009; Ackermann et al. 2010; Jeltama & Profumo 2011; Brunetti et al. 2012; Zandanel & Ando 2014; Ackermann et al. 2016; Brunetti et al. 2017). The secondary model is further challenged by the large amount of energy that is required to explain the steep spectra of some radio haloes (e.g. Brunetti 2004; Brunetti et al. 2008). However, the observed radio emission may be caused by a combination of the mechanisms in which the secondary

electrons are re-accelerated by merger turbulence (Brunetti & Blasi 2005; Brunetti & Lazarian 2011b; Pinzke et al. 2017).

Radio relics have been proposed to be the synchrotron emission from large-scale shocks that are generated during cluster mergers (e.g. Enßlin et al. 1998). Relativistic electrons gain energy either from the direct acceleration of the ICM thermal electrons or from the re-acceleration of fossil plasma remnants of active galactic nuclei (AGN) through Fermi-I DSA (e.g. Giacintucci et al. 2008; Markevitch et al. 2005). Observational evidence associating the formation of radio relics with cluster merger shocks have been observed in a large number of merging clusters (e.g. van Weeren et al. 2010; Bonafede et al. 2012; Stroe et al. 2013; de Gasperin et al. 2015; van Weeren et al. 2016c or see Feretti et al. 2012 for a review). The evidence includes (i) an arc-like morphology of some relics, which is consistent with an edge-on/close to edge-on view of 3D shock waves, (ii) spectral gradients or spectral curvature variations across the width of relics, suggesting that the relativistic electrons gain energy at the shock fronts and lose their energy after shock passage and (iii) high degree of linear polarization, indicating a magnetic field aligned within the shock plane. The distribution of size, shape and location of relics agree well with those of merger shocks in cosmological simulations (e.g. Nuza et al. 2017). Alternatively, the re-acceleration model requires pre-existing populations of mildly relativistic electrons to be present in the regions of the shocks and there is evidence for this in a few cases (e.g. van Weeren et al. 2013; Bonafede et al. 2014; Shimwell et al. 2015; Botteon et al. 2016a; van Weeren et al. 2017).

Galaxy clusters that host double radio relics on diametrically opposite sides of the clusters are some of the most interesting cases to study particle (re-)acceleration at Mpc scales. Only 17 double-relics clusters have been detected to date (Bonafede et al. 2017 and references therein). In these rare energetic merging clusters both the relics and the halo are expected to be generated by shocks and turbulence, respectively. Due to the diametrically opposite locations of the double relics, these shocks are thought to be caused by head-on binary mergers of roughly equal masses merging on/close to the plane of the sky (e.g. van Weeren et al. 2011a; Nuza et al. 2017). Hence, double-relic clusters provide a unique environment for studies of particle (re-)acceleration without the complication of projection effects (i.e. to minimise a mixture of relativistic electron populations along the line-of-sight (LOS); Stroe et al. 2013). Furthermore, since the possibility to have seed populations of mildly relativistic electrons is likely to correlate with the distribution of aged AGN, these double relics might provide hints

as to whether relics are formed by acceleration directly from the thermal pool or from fossil plasma pre-existing in the ICM.

Abell 1240 ( $z = 0.1948$ ; hereafter A1240) is a binary merging galaxy cluster ( $M_{500} = (3.7 \pm 0.4) \times 10^{14} M_{\odot}$ ; Planck Collaboration et al. 2016). A1240 was first observed to host faint diffuse emission located on the opposite sides of the cluster by Kempner & Sarazin (2001). Follow-up observations by Bonafede et al. (2009) confirmed the existence of the radio relics (labelled as A1240-1 and A1240-2 for the northern and southern relics, respectively) and found that they are elongated over  $\sim 650$  kpc and  $\sim 1250$  kpc in the east-west direction. Across the width of A1240-1, the spectral indices<sup>1</sup> steepen from  $-1.1$  to  $-1.6$  towards the cluster centre. Polarized emission was observed from the relics at 1.4 GHz and the electric field vectors are approximately perpendicular to the major axes of the relics, indicating the alignment of the ICM magnetic fields. Assuming a relativistic electron energy of Lorentz factor  $\geq 100$  with the spectrum of  $N(p) \propto p^{-\delta}$  (where  $\delta = -2\alpha_{\text{int}}$ ,  $\alpha_{\text{int}}^{\text{A1240-1}} = -1.2$  and  $\alpha_{\text{int}}^{\text{A1240-2}} = -1.3$ ) and equipartition energy conditions, Bonafede et al. (2009) estimated the equipartition magnetic field of  $2.4 \mu\text{G}$  and  $2.5 \mu\text{G}$  for A1240-1 and A1240-2, respectively. Due to their properties (i.e. location, morphology, spectral gradients and polarization properties), the relics were interpreted as synchrotron emission from large-scale shocks that were generated by a cluster merger in the plane of the sky and are moving outwards. Using the integrated spectral indices, Bonafede et al. (2009) estimated the Mach numbers of  $\mathcal{M}_{\text{int}} = 3.3 \pm 0.2$  for A1240-1 and  $\mathcal{M}_{\text{int}} = 2.8 \pm 0.3$  for A1240-2.

In the optical band, Barrena et al. (2009) studied the dynamical properties of A1240 using spectroscopic redshifts from 145 galaxies. A1240 was found to have a bimodal structure with clumps of galaxies separated in the north-south direction. The galaxy clumps have a relative rest-frame LOS velocity of  $V_{\text{rf}} = 390 \text{ km s}^{-1}$  at a projected distance of  $1.2 h_{70}^{-1}$  Mpc. The galaxy clumps were estimated to have passed 0.3 Gyr ago. Approximately 12 arcmin ( $\sim 2.3$  Mpc) to the south of A1240 is Abell 1237 (hereafter A1237;  $z = 0.1935$ , Barrena et al. 2009) that is thought to be in-falling to A1240. Barrena et al. (2009) found no signature of peculiar displacement of A1240 towards the direction of A1237 and suggested that A1237 and A1240 are in the pre-merging stage.

In this paper, we present Low Frequency Array (LOFAR) 120 – 187 MHz observations of A1240. LOFAR’s sensitivity to large-scale emission coupled with its high-angular resolution helps us to study the extended

---

<sup>1</sup>The convention  $S \propto \nu^{\alpha}$  is used in this paper

diffuse emission from A1240 in detail. Furthermore, LOFAR observations at low frequencies  $\leq 200$  MHz allow us to detect steep spectrum emission such as from radio haloes that are generated during minor mergers or mergers of low-mass clusters. In combination with archival Giant Metrewave Radio Telescope (GMRT) 595 – 629 MHz and Karl G. Jansky Very Large Array (VLA) 2 – 4 GHz data, we study spatial variations of spectral indices of the radio sources in A1240 across a wide frequency range. We use the VLA data to study the polarized emission from the cluster relics.

Throughout this paper, we assume  $H_0 = 70 \text{ km s}^{-1} \text{ Mpc}^{-1}$ ,  $\Omega_M = 0.3$  and  $\Omega_\Lambda = 0.7$ . In this cosmology, 1 arcmin corresponds to  $\sim 194h_{70}^{-1} \text{ kpc}$  at the cluster redshift of  $z = 0.1948$ .

## 3.2 Observations and data reduction

### 3.2.1 LOFAR 143 MHz

A1240 was observed with LOFAR for 8 hours on March 22, 2016 as part of the LOFAR Two-meter Sky Survey (LoTSS, Shimwell et al. 2017). A1240 was located at an angular distance of  $\sim 55$  arcmin from the LoTSS grid pointing centre (pointing P170+42 of project LC4\_034), where the primary beam sensitivity is  $\sim 78$  percent of the value at the pointing centre. The observations used the High-Band Antennas (120 – 187 MHz) on 48 core, 14 remote and 9 international stations. However, to obtain cluster maps at spatial resolutions of  $> 8$  arcsec, we used only data from baselines that have  $uv$ -range between  $15 \lambda$  and  $66 \text{ k}\lambda$ . For calibration purposes, 3C 196 was observed for 10 minutes before the target field. Details of the observations are listed in Table 3.1.

We used the facet calibration scheme to calibrate the target data for both direction-independent and direction-dependent effects. Details of the facet calibration are given in van Weeren et al. (2016a); Williams et al. (2016). But for completeness, we briefly describe the procedure below.

During the direction-independent calibration part, the target data were flagged for radio frequency interference (RFI) using AOflogger (Offringa et al. 2012) and time periods where the contamination from bright radio sources in the sidelobes (i.e. Cassiopeia A, Hercules A, Taurus A and Virgo A) were also flagged. The amplitude gains, initial clock and XX-YY phase offsets were derived from gain solutions of 3C 196. Here the calibration solutions of 3C 196 were obtained by calibrating a 4-Gaussian component source model that has an integrated flux of 83.1 Jy at 150 MHz in agreement



Table 3.1: LOFAR, GMRT and VLA observations

	LOFAR 143 MHz	GMRT 612 MHz	VLA 3 GHz
Pointing (RA, Dec)	170 <sup>h</sup> 48 <sup>m</sup> 54.0 <sup>s</sup> , +42 <sup>d</sup> 10 <sup>m</sup> 13.08 <sup>s</sup>	11 <sup>h</sup> 23 <sup>m</sup> 32.1 <sup>s</sup> , +43 <sup>d</sup> 06 <sup>m</sup> 31.9 <sup>s</sup>	11 <sup>h</sup> 23 <sup>m</sup> 29.0 <sup>s</sup> , +43 <sup>d</sup> 09 <sup>m</sup> 42.0 <sup>s</sup> 11 <sup>h</sup> 23 <sup>m</sup> 35.0 <sup>s</sup> , +43 <sup>d</sup> 01 <sup>m</sup> 12.9 <sup>s</sup>
Configuration	N/A	N/A	C, D
Observation date	March 22, 2016	July 2, 2011	October 10, 2014 (C) October 09, 2015 (D)
On-source time (hr)	8.0	6.0	1.1 (C), 3.4 (D)
Freq. coverage (GHz)	0.120 – 0.187	0.595 – 0.629	2 – 4
Usable bandwidth (GHz)	0.043	0.0333	1.992
Channel width (MHz)	0.0122	0.13	2
Integration time (s)	1	16	~ 5
Correlation	XX, XY, YX, YY	RR, LL	RR, RL, LR, LL
Number of antennas	62	28	51

with the Scaife & Heald (2012) absolute flux scale.

To prepare for the direction-dependent calibration, “blank” data sets for the target field were made by subtracting all sources within a  $\sim 30^\circ$  radius of the field centre using the direction independent calibration solutions. The CLEAN components used for the subtraction were obtained from imaging at resolutions of  $\sim 40$  arcsec and  $\sim 2$  arcmin.

In the direction-dependent calibration part, we aimed to obtain thermal-noise limited images of the cluster. To achieve this, the ionospheric distortions and beam errors towards the target direction were corrected and the contamination from nearby sources was minimized following the facet calibration procedure. The target field was divided into 15 regions (called facets), each containing bright, compact calibrator source(s). The direction-dependent gain and TEC (total electron content) solutions for each facet were derived by self-calibrating on selected calibrator sources and then applied to all other sources in the facet. The facet sky models, that were corrected for the direction-dependent effects, were progressively subtracted from the data. The procedure was repeated until only the last facet, containing A1240, was left in the data. The facet calibrator (i.e. B3 1121+435 at RA=11:24:32.043, Dec=+43:15:42.77) that was used to calibrate the facet containing the cluster has a flux of 2.91 Jy. As the distance between the facet calibrator and A1240 is 14 arcmin, the ionospheric and instrumental phase corrections should be similar to those towards the direction of A1240.

The data reduction was performed with the facet-calibration pipeline<sup>2</sup>. The pipeline exploits DPPP (LOFAR Default PreProcessing Pipeline) for data editing (i.e. flagging, averaging, concatenating), BBS (BlackBoard Selfcal, Pandey et al. 2009) for calibration and WSClean (W-Stacking Clean, Offringa et al. 2014) for imaging. To obtain final continuum images of A1240, the calibrated data were deconvolved in CASA (Common Astronomy Software Applications; McMullin et al. 2007, see Subsec. 3.2.4).

### 3.2.2 GMRT 612 MHz

The GMRT 595–629 MHz observations of A1240 were performed on July 2, 2011 for 6 hours (project code: 20\_004, PI: A. Bonafede). During the target observations, the radio source 1035+564 was observed for 5 minutes every about 40 minutes and was used as a phase calibrator. For flux calibration, two bright radio sources 3C 147 and 3C 286 were observed before and after the target observations. The observation details are given in Table 3.1.

---

<sup>2</sup><https://github.com/tammojan/facet-calibration>

The GMRT 612 MHz data were reduced with the Software Peeling and Atmospheric Modelling (SPAM) package (Intema et al. 2009) that performed both direction-independent and direction-dependent calibration. The direction-independent calibration using 3C 147 included flagging RFI, correcting initial phase offsets between the parallel-handed correlations, antenna-based phase delay and amplitude calibration. The flux scale of the primary calibrator 3C 147 was set according to the Scaife & Heald (2012) flux scale. Then a phase calibration was performed using a wide-field sky model. In the direction-dependent calibration, SPAM iteratively solved for amplitude and phase gains towards multiple directions in the target field. The calibration solutions were used to fit a 2D ionospheric model and the derived ionospheric corrections were then applied to the target data. To obtain final images, the direction-dependent calibrated data in the direction of A1240 were deconvolved with CASA (see Subsec. 3.2.4).

### 3.2.3 VLA 3 GHz

The VLA S-band observations were performed in C and D configuration on Oct. 10, 2014 and Oct. 09, 2015, respectively (project: 14B-157, PI: W. Dawson). In each configuration the array was separately pointed at each radio relic. The observations used 16 spectral windows, each of which was split into 64 channels, and covered the 2 – 4 GHz bandwidth in total. An overview of the observations is given in Table 3.1.

Following van Weeren et al. (2016b), we separately processed the target data for each configuration/pointing with the CASA package. The target data were Hanning smoothed and corrected for elevation-dependent gains and antenna position offsets. The RFI was flagged with the automatic flaggers in CASA and AOflogger (Offringa et al. 2012). The antenna delays and bandpass were derived using a model of 3C 286 that is set to the Perley & Butler (2013) flux scale and has an uncertainty of a few percent (Perley & Butler 2013). The cross-hand delays were solved using 3C 286, assuming a fractional polarization of 11% and a RL-phase difference of  $66^\circ$ . The polarization leakage terms for every channel were determined from J1407+2827 which served as a low polarization leakage calibrator. After the calibration parameters were derived they were transferred to the target data. The phase calibration of the target field was calculated every 20 minutes using J1146+3958. To improve the fidelity of the target field image, self-calibration loops were then performed. Finally, the calibrated data for the C and D configurations that have the same pointing centres were concatenated in  $uv$ -plane and were used to make continuum images

(see Subsec. 3.2.4).

### 3.2.4 Continuum imaging

To map the diffuse source structure with the wide-band data sets we exploited multi-scale and multi-frequency synthesis (MS – MFS) in CASA (McMullin et al. 2007; Cornwell 2008; Rau & Cornwell 2011). The LOFAR, GMRT and VLA calibrated data were separately CLEANed with MS – MFS to model the complex emission from A1240. The scales used in the deconvolution are multiscale =  $[0, 3, 7, 25, 60, 150] \times$  pixels, where the zero scale is for modelling point sources and the larger scales are for sampling the diffuse emission. Due to the wide fractional bandwidth of the VLA observations the primary beam considerably varies across the band and three Taylor terms (nterms = 3) were used to model the frequency dependence of the radio emission. nterms = 2 and 1 were used for the LOFAR and GMRT data that have bandwidths of 43 MHz and 33 MHz, respectively. Additionally a wide-field algorithm (W – projection, Cornwell et al. 2005, 2008) was employed to account for the non-coplanarity of the baselines across the sky. Specially depending on the image size, wprojplanes = 448 was used for the LOFAR data and wprojplanes = 384 was set for the WSRT and GMRT data.

To optimise for imaging on various different angular scales, the LOFAR, GMRT and VLA  $uv$ -data were weighted using Briggs’s robust weighting (Briggs 1995) in combination with uvtapers to down-weighting the outer baselines (see Table 3.2). The final LOFAR and VLA images were corrected for the attenuation of the primary beams that were generated with AWImager (Tasse et al. 2012) and CASA (McMullin et al. 2007), respectively. The GMRT 612 MHz images were also corrected for primary beam attenuation<sup>3</sup>,

$$A(x) = 1 - \frac{3.486}{10^3}x^2 + \frac{47.749}{10^7}x^4 - \frac{35.203}{10^{10}}x^6 + \frac{10.399}{10^{13}}x^8, \quad (3.1)$$

where  $x = f \times \theta$ , here  $\theta$  is angular distance in arcmin to the pointing centre, and  $f = 0.612$  GHz is the frequency of the GMRT observations.

### 3.2.5 Spectral index measurements

To make spectral index maps of A1240 we combined LOFAR 143 MHz, GMRT 612 MHz and VLA 3 GHz continuum images. To measure approxi-

---

<sup>3</sup>GMRT User’s manual

Table 3.2: Imaging parameters that were used to make images of A1240 and the image properties.

Data	$uv$ -range ( $kl$ )	Robust <sup>a</sup> (outertaper)	$\theta_{\text{FWHM}}$ (arcsec $\times$ arcsec, $PA$ )	$\sigma_{\text{rms}}$ ( $\mu\text{Jy beam}^{-1}$ )	Stokes	Fig.
LOFAR 143 MHz	0.2 – 66	–0.25 (5 arcsec)	$15 \times 10$ ( $87^\circ$ )	165	<i>I</i>	3.1
	0.2 – 66	0.10 (25 arcsec)	$41 \times 36$ ( $13^\circ$ )	410	<i>I</i>	3.3
	0.2 – 41	–0.25 (10 arcsec)	$21 \times 21$ <sup>b</sup>	280	<i>I</i>	3.4 <sup>c</sup>
GMRT 612 MHz	0.2 – 41	–0.25 (17 arcsec)	$21 \times 21$ <sup>b</sup>	175	<i>I</i>	3.4 <sup>c</sup>
	0.2 – 41	–0.25 (9 arcsec)	$21 \times 21$ <sup>b</sup>	17	<i>I</i>	3.4 <sup>c</sup>
	0.2 – 41	0.00	$18.5 \times 14.5$ ( $85^\circ$ )	13	<i>I</i>	3.6
VLA 3 GHz	0.2 – 41	0.00	$18.5 \times 14.5$ ( $85^\circ$ )	$\sim 6.4$	$\hat{Q}$	3.6 <sup>d</sup>
	0.2 – 41	0.00	$18.5 \times 14.5$ ( $85^\circ$ )	$\sim 6.5$	<i>U</i>	3.6 <sup>d</sup>
	0.2 – 41	0.00	$18.5 \times 14.5$ ( $85^\circ$ )	$\sim 6.5$	<i>U</i>	3.6 <sup>d</sup>

Notes: <sup>a</sup>: Briggs weighting of visibilities; <sup>b</sup>: smoothed; <sup>c</sup>: spectral index map; <sup>d</sup>:  $F$  vector map

mately the same spatial scales of emission, we selected a common  $uv$ -range (0.2 – 41.0  $k\lambda$ ) for the data sets when making the total intensity images. A common Briggs weighting (robust = -0.25) was applied to the data sets. It is noted that uniform weighting, or attempting to directly match the  $uv$ -coverage, helps to accurately compare interferometric images. However, such weighting of the  $uv$ -data significantly increases the noise levels of the continuum images. Instead, we used the Briggs weighting to increase signal to noise ratio (SNR) of the sources and attempted to ensure that the native resolution of the images from the different arrays was equal by applying different  $uv$ -tapers. To obtain an angular resolution of 20 arcsec we used an outer  $uv$ -taper of 10 arcsec, 17 arcsec and 9 arcsec for the LOFAR, GMRT and VLA data, respectively. The native resolution with these imaging parameters was 19.7 arcsec  $\times$  14.9 arcsec (position angle of  $PA = 86.3^\circ$ ) for the LOFAR image, 19.2 arcsec  $\times$  14.0 arcsec ( $PA = 24.4^\circ$ ) for the GMRT image and 20.0 arcsec  $\times$  15.8 arcsec ( $PA = -84.4^\circ$ ) for the VLA image. These total intensity maps were smoothed to an identical resolution of 21 arcsec, aligned and regridded. The LOFAR, GMRT and VLA images have noise levels of  $\sigma_{\text{rms}} = 280, 175$  and  $17 \mu\text{Jy}/\text{beam}$ , respectively. The spectral indices were calculated for each pixel by fitting the  $\geq 3\sigma_{\text{rms}}$  pixels in at least two images with a power-law function,  $S \propto \nu^\alpha$ . To estimate the spectral index error, we adapted a common flux scale uncertainty of 10% associated with the calibration of the LOFAR, GMRT and VLA data, as commonly used in the literature (e.g. van Weeren et al. 2016c; Hoang et al. 2017).

### 3.2.6 Polarization measurements

We used the VLA 2 – 4 GHz data to study the linear polarization properties of the faint diffuse emission from A1240. We made multiple polarization maps with (i) the full bandwidth 2 – 4 GHz data which maximised the polarization detection significance, (ii) successive narrower (480 MHz) band data to examine the frequency dependence of the polarized emission and (iii) successive 224 MHz bandwidth chunks to ensure that our measurements were not suffering from bandwidth depolarisation. In each case we made Stokes  $I$ ,  $Q$  and  $U$  images with WSClean (Offringa et al. 2014). The imaging was done with the multi-scale and joined-channel deconvolution algorithm (Offringa & Smirnov 2017). We also used Briggs (robust = 0.00) weighting on the  $uv$ -data. The reason for using WSClean, instead of CASA, is because the combination of multiscale and Stokes  $Q/U$  CLEAN, which is essential for recovering the faint diffuse polarized emission of A1240, is not yet available in CASA (version 4.7). To obtain the polarization intensity  $P$

and angle  $\phi$  maps, the Stokes  $Q$  and  $U$  images were combined as follows,

$$P = \sqrt{Q^2 + U^2}; \quad \phi = \frac{1}{2} \arctan \frac{U}{Q}. \quad (3.2)$$

From the polarized  $P$  and Stokes  $I$  emission maps, the total polarization fraction,  $F = P/I$ , was calculated for pixels within the  $\geq 3\sigma_{\text{rms}}$  region of the Stokes  $I$  image. To obtain the corrected flux measurements, the final Stokes  $P$  and  $I$  images were then divided by the VLA primary beam to correct for the sensitivity attenuation.

The polarization angle calculated from Eq. 3.2 was further corrected for the Faraday rotation caused by the Galactic magnetic field (i.e.  $\phi_{\text{A1240}} = \phi_{\text{Eq. 3.2}} - \phi_{\text{Galactic}}$ ). Given the mean Galactic rotation measure (RM) of 9.4 rad/m<sup>2</sup> towards the direction of A1240 (Oppermann et al. 2012), the Galactic Faraday rotation ( $\phi_{\text{Galactic}} = \text{RM} \times \lambda^2$ ) is 12° and 3° at the lower and higher edges of the 2 – 4 GHz band, respectively. Since the polarized emission map was made with full bandwidth data that has the central frequency at 3 GHz, we corrected the Galactic Faraday rotation using  $\phi_{\text{Galactic}} = 5^\circ$  (Oppermann et al. 2012).

### 3.2.7 Chandra X-ray data

The Chandra ACIS-I observation (ID: #4961, PI: Kempner) of A1240 was taken on Feb. 5, 2005 and has a duration of 52 ks. Following the data reduction procedure described in Vikhlinin et al. (2005), we applied the calibration files<sup>4</sup> using the *chav* package<sup>5</sup>. The calibration includes filtering out bad pixels, correcting for the position-dependent inefficiency of the charge transfer and correcting for photon energies with gain maps. The background emission was subtracted using standard blank sky files. For more details on the reduction procedure, we refer to Vikhlinin et al. (2005).

## 3.3 Results

In Fig. 3.1 we present high-resolution continuum images of A1240 that were made with LOFAR at a frequency of 143 MHz. The GMRT 612 MHz and VLA 3 GHz contours are overlaid on the Subaru r-band image in Fig. 3.2. The resolution is  $\theta_{\text{FWHM}} = 15 \text{ arcsec} \times 10 \text{ arcsec}$  ( $PA = 87^\circ$ ) for the LOFAR image and is  $\theta_{\text{FWHM}} = 21 \text{ arcsec} \times 21 \text{ arcsec}$  for the VLA

<sup>4</sup>CIAO v4.6 and CALDB v4.6.5

<sup>5</sup><http://hea-www.harvard.edu/~alexey/CHAV>

and GMRT images. A common Briggs' robust weighting of  $-0.25$  and outertaper = 5 arcsec, 17 arcsec and 9 arcsec were used for the LOFAR, GMRT and VLA imaging (see Subsec. 3.2.4). In Fig. 3.3 we present a low-resolution ( $41 \text{ arcsec} \times 36 \text{ arcsec}$ ,  $PA = 13^\circ$ ) 143 MHz image of A1240 (robust = 0.10, outertaper = 25 arcsec). The radio relics in the northern and southern outskirts of A1240, that were previously observed with the WENSS 325 MHz in Kempner & Sarazin (2001) and with the VLA 325 MHz and 1.4 GHz in Bonafede et al. (2009), were detected with a peak flux of  $12\sigma_{\text{rms}}$  in our high resolution images (Figs. 3.1-3.3). Bonafede et al. (2009) previously presented spectral index and polarization properties and equipartition magnetic field measurements of the relics. With the wide-band observations between 143 MHz and 3 GHz we provide new measurements on the spectra and polarization properties of the relics.

### 3.3.1 The double radio relics

The detected relics (Figs. 3.1 and 3.2) have projected sizes of  $0.68 \times 0.20 \text{ Mpc}^2$  and  $1.35 \times 0.35 \text{ Mpc}^2$ , respectively; and their major axes are aligned with the  $3\sigma_{\text{rms}}$  edges of the Chandra X-ray emission (Fig. 3.3). For both relics, the surface brightness gradient is steeper on the outer edges than that in the inner edges. Across the length of A1240-1, the surface brightness gradually decreases from west to east. The emission on the western and eastern sides of A1240-2 appears completely detached at 612 MHz and 3 GHz (Fig. 3.2), but is connected at 143 MHz (Fig. 3.1).

### Spectral analysis

In Fig. 3.4 (left) we present the three-frequency spectral index map between 143 MHz and 3 GHz of A1240 (see Subsec. 3.2.5). In Fig. 3.4 (left), the spectral indices for A1240-1 and A1240-2 were found to steepen from the outer edge towards the inner regions. The steepening trend across the width of the relics is better visible in the spectral index profiles in the right panel of Fig. 3.4. In particular the spectral indices are  $-0.94 \pm 0.06$  and  $-0.97 \pm 0.05$  at the outer edges of A1240-1 and A1240-2, respectively. Towards the inner regions at a distance of 63 arcsec ( $\sim 204 \text{ kpc}$ ) from the outer edges of A1240-1 and A1240-2, the spectral indices significantly steepen to  $-1.16 \pm 0.05$  and  $-1.23 \pm 0.05$ , respectively.

To estimate the integrated spectral indices of A1240-1 and A1240-2, we used the LOFAR 143 MHz, GMRT 612 MHz and VLA 3 GHz images that were used to make the spectral index map in Fig. 3.4. The integrated fluxes



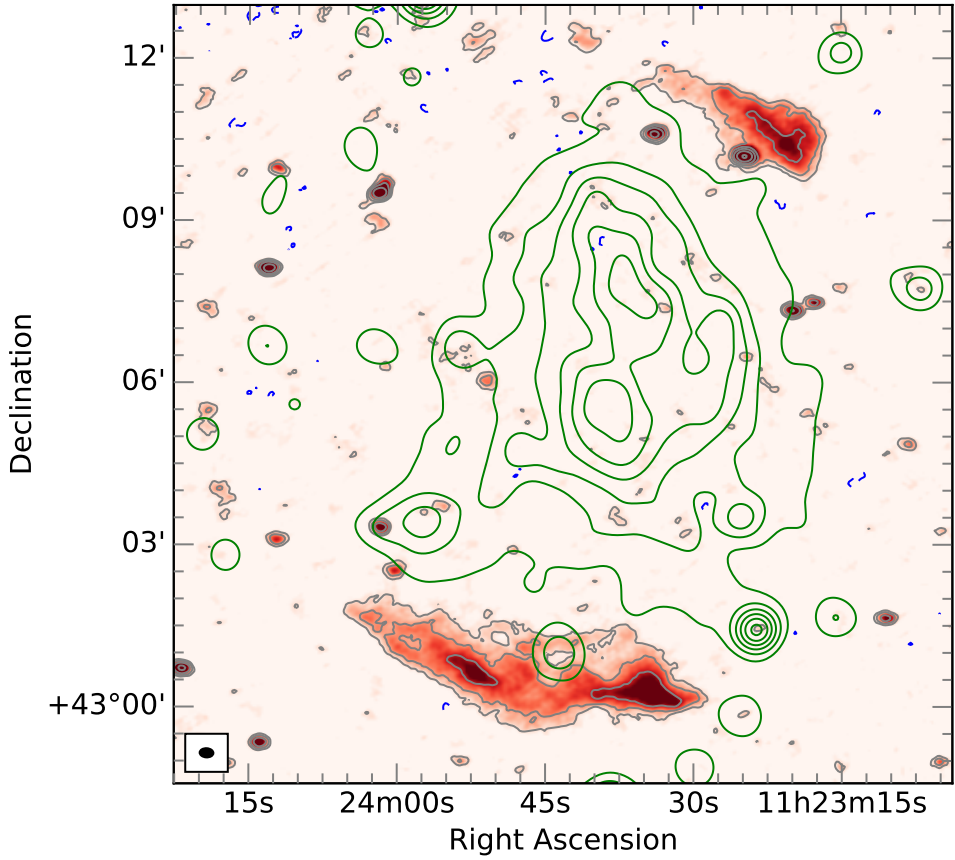


Figure 3.1: LOFAR 143 MHz total intensity map of A1240 with contours in grey (positive) and blue (negative) ( $\theta_{\text{FWHM}} = 15 \text{ arcsec} \times 10 \text{ arcsec}$ ,  $PA = 87^\circ$ ). The contours are  $[-3, 3, 6, 12, 24, 48] \times \sigma_{\text{rms}}$ , where  $\sigma_{\text{rms}} = 165 \mu\text{Jy}/\text{beam}$ . The green contours are the Chandra X-ray surface brightness smoothed with a 2D Gaussian kernel to 40 arcsec resolution. The X-ray contour levels are  $[3, 6, 9, 12, 15, 18] \times \sigma$ , where  $\sigma = 0.5 \times 10^{-6} \text{ cts/s/arcmin}^2$ .

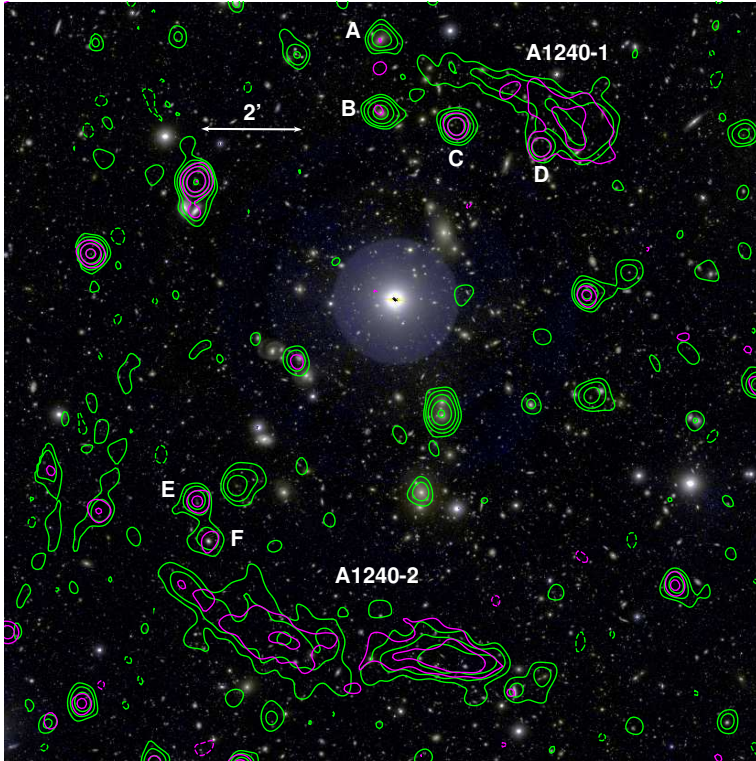


Figure 3.2: A Subaru r,g band image of A1240. The VLA (green) and GMRT (magenta) contours are levelled at  $[-3, 3, 6, 12, 24, 48] \times \sigma_{\text{rms}}$  (dashed negative), where  $\sigma_{\text{rms}} = 175 \mu\text{Jy}/\text{beam}$  and  $17 \mu\text{Jy}/\text{beam}$  for the GMRT and VLA images, respectively. The resolution of the radio images is  $\theta_{\text{FWHM}} = 21 \text{ arcsec} \times 21 \text{ arcsec}$ . The radio sources are labelled.

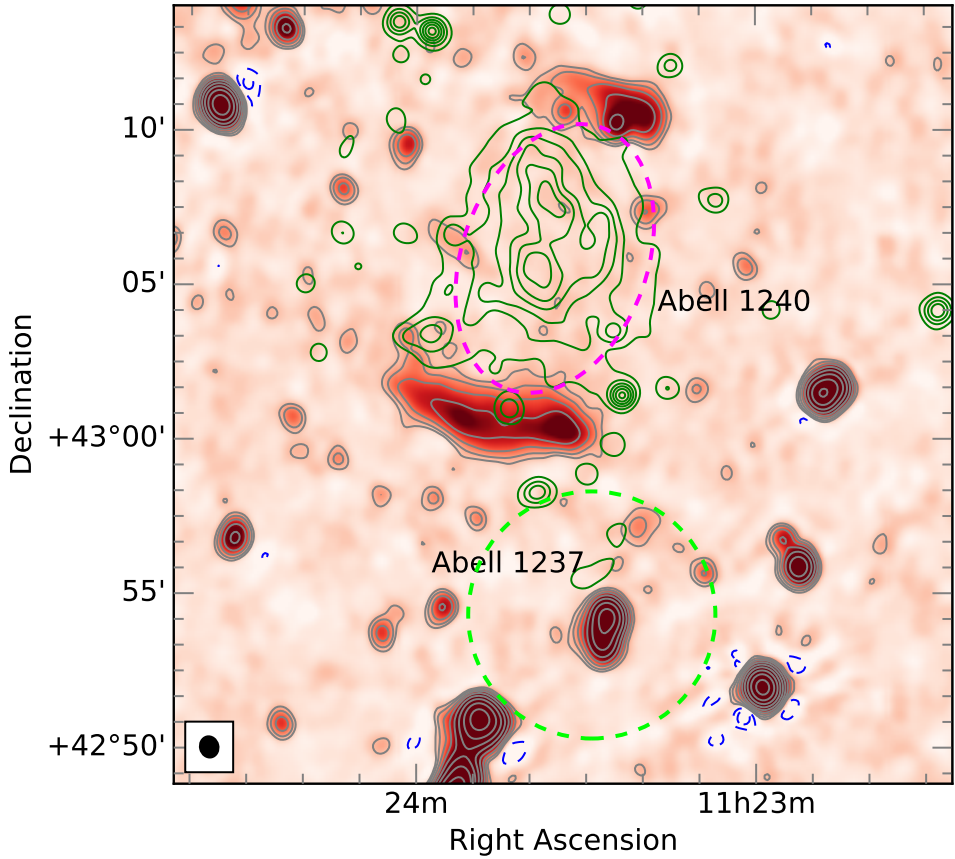


Figure 3.3: LOFAR 143 MHz total intensity map of A1240 with contours in grey (positive) and blue (negative) ( $\theta_{\text{FWHM}} = 41 \text{ arcsec} \times 36 \text{ arcsec}$ ,  $PA = 13^\circ$ ). The contours are  $[-3, 3, 6, 12, 24, 48] \times \sigma_{\text{rms}}$ , where  $\sigma_{\text{rms}} = 410 \mu\text{Jy}/\text{beam}$ . The X-ray contours are identical to those in Fig. 3.1 and are only available for A1240. The dashed magenta ellipse shows the region where the upper limit of diffuse emission is estimated in Subsec. 3.4.2. The green dashed circle marks the region of A1237.

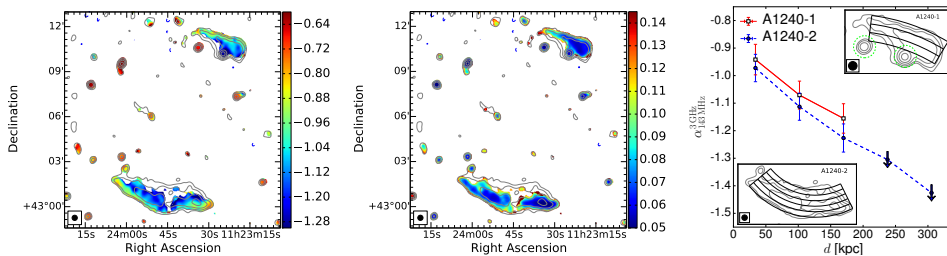


Figure 3.4: Left: Three-frequency spectral index map between 143 MHz and 3 GHz of A1240 at 21 arcsec (or  $\sim 68$  kpc) resolution. Middle: The corresponding spectral index error map. Right: The spectral index profiles across the width of the relics A1240-1 and A1240-2 and towards the cluster centre. The flattest spectral indices are  $-0.94 \pm 0.06$  and  $-0.97 \pm 0.05$  at the outer edges of A1240-1 and A1240-2, respectively. The subplots show the regions where the spectral indices were extracted. The compact sources (i.e. green dotted circles) were masked. The radial size of the region is equal to the synthesized beam size of 21 arcsec. The downward pointing arrows indicate the upper limit of the spectral indices that have  $< 2\sigma_{\text{rms}}$  detection confidence levels in VLA and/or GMRT observations. The LOFAR 143 MHz superimposed contours in both panels are at identical spacings to those in Fig. 3.1 (here  $\sigma_{\text{rms}} = 280 \mu\text{Jy}/\text{beam}$ ).

Table 3.3: Integrated fluxes for the radio relics of A1240.

Source	$S_{143 \text{ MHz}}$ (mJy)	$S_{612 \text{ MHz}}$ (mJy)	$S_{3 \text{ GHz}}$ (mJy)
A1240-1	$68.45 \pm 1.38$	$13.32 \pm 1.60$	$2.54 \pm 0.09$
A1240-2	$202.39 \pm 2.40$	$33.77 \pm 3.70$	$6.43 \pm 0.17$

were measured within the  $\geq 3\sigma_{\text{rms}}$  region of the LOFAR image on all three images, are given in Table 3.3 and is plotted in Fig. 3.5. The measured fluxes at three frequencies were fit with a power-law function,  $S \propto \nu^\alpha$ . The best-fit spectral indices for A1240-1 and A1240-2 were estimated to be  $-1.08 \pm 0.05$  and  $-1.13 \pm 0.05$ , respectively. Our spectral index measurements are statistically consistent with the 325 MHz – 1.4 GHz measurements of  $-0.96 \pm 0.26$  and  $-1.11 \pm 0.27$  in Kempner & Sarazin (2001) and  $-1.2 \pm 0.1$  and  $-1.3 \pm 0.2$  in Bonafede et al. (2009). In addition, to search for spectral curvature we divided the data into two frequency intervals: from 143 to 612 MHz and from 612 MHz to 3 GHz. We estimated the integrated spectral indices between 143 and 612 MHz to be  $-1.13 \pm 0.11$  and  $-1.23 \pm 0.10$  for A1240-1 and A1240-2, and between 612 MHz and 3 GHz to be  $-1.03 \pm 0.10$  and  $-1.08 \pm 0.05$  for A1240-1 and A1240-2, providing no clear evidence for spectral curvature between 143 MHz and 3 GHz in either relic.

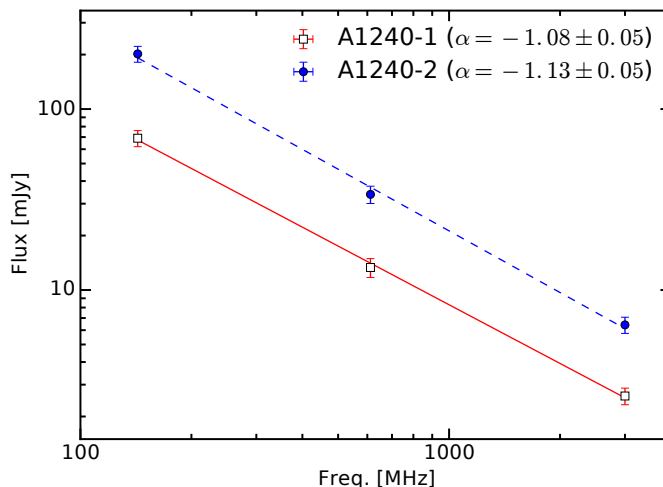


Figure 3.5: Integrated spectra for the radio relics of A1240. The integrated fluxes of the relics were measured in the LOFAR 143 MHz, GMRT 612 MHz and VLA 3 GHz 21 arcsec-resolution images (Table 3.2) and are given in Table 3.3. The spectral index values that were obtained from the spectral power-law fitting,  $S \propto \nu^\alpha$ , for the relics are given in Table 3.4.

### Polarization analysis

In Fig. 3.6 we present polarization electric field vectors in the regions of the relics. The polarized radio emission is extended along the length of the relics. The electric field vectors are approximately perpendicular to the major axes of the relics. The integrated fractional polarization at 3 GHz is  $29 \pm 2\%$  (up to  $\bar{F}_{\text{beam}} = 58\%$  in the most polarised regions in Fig. 3.6) for A1240-1 and is  $16 \pm 2\%$  (up to  $\bar{F}_{\text{beam}} = 40\%$ ) for A1240-2. Our fractional polarization measurement is close to the value of 26% for A1240-1 measured from the VLA 1.4 GHz data (Bonafede et al. 2009), but lower than that of 29% for A1240-2.

We examined the dependence of the fractional polarization on frequency. The VLA 2 – 4 GHz data were split into 4 sub data sets, each of which has a bandwidth of 480 MHz. For each 480 MHz data set, we made polarized emission and total intensity (Stokes  $I$ ) images in a similar manner to the procedure used for the full-band 2 – 4 GHz data (see Subsec. 3.2.6). The region that was used to measure the integrated polarized fluxes is within the  $\geq 3\sigma_{\text{rms}}$  pixels of the full-band Stokes  $I$  image. The fractional polarization,  $F = P/I$ , was estimated for each 480 MHz data set and is plotted in Fig. 3.6. The mean polarized emission for the first-three 480 MHz data chunks

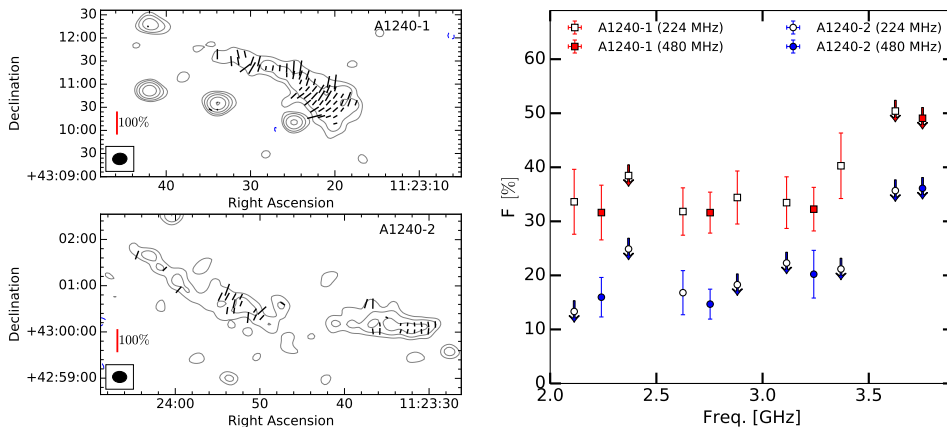


Figure 3.6: Left: Electric field vector maps in the regions of the A1240 relics. The red vertical reference lines for 100% of fractional polarization are shown in the left bottom corners. The VLA 2 – 4 GHz 18.5 arcsec  $\times$  14.5 arcsec resolution (grey) contours are at identical levels to those in Fig. 3.1 (here  $\sigma_{\text{rms}} = 13 \mu\text{Jy}/\text{beam}$ ). Right: Fractional polarization of A1240-1 and A1240-2 between 2 and 4 GHz. The down pointing arrows indicate the data points where polarized emission is below  $1.4\sigma_{\text{rms}}$  detection limit. The fractional polarization for the VLA 224 MHz and 480 MHz bandwidth data sets are in line with each other.

for A1240-1 and A1240-2 were measured to be  $\sim 32 \pm 4\%$  and  $\sim 17 \pm 4\%$ , respectively. These fractional polarization measurements are consistent with the mean values (i.e.  $29 \pm 2\%$  for A1240-1 and  $16 \pm 2\%$  for A1240-2) that we measured directly from the full-band polarized emission map (Fig. 3.6) indicating that our measurements are not severely affected by bandwidth depolarisation. Furthermore, measurements were also made with a bandwidth of 224 MHz and these, whilst at lower SNR, are consistent with both the 2 GHz and 480 MHz bandwidth measurements (Fig. 3.6). The polarization angle of the emission over the regions of A1240-1 and A1240-2 was measured to be approximately constant over the 2 – 4 GHz bandwidth.

### 3.3.2 A connection with Abell 1237

Fig. 3.3 shows the location of A1237 which is a cluster that is falling to A1240 from the south (Barrena et al. 2009). In the central region of A1237 we detect a tailed radio galaxy that shows extended emission towards the south, suggesting that the radio galaxy is moving to the north with respect to the local ICM. No diffuse large-scale emission was observed from the ICM of A1237 or the region between the clusters. Using the 41 arcsec  $\times$  36 arcsec-

Table 3.4: Spectral properties and Mach numbers for the radio relics.

Source	$\alpha_{\text{int}}$	$\alpha_{\text{inj}}$	$\mathcal{M}_{\text{int}}$	$\mathcal{M}_{\text{inj}}$
A1240-1	$-1.08 \pm 0.05$	$-0.94 \pm 0.06$	$5.1_{-1.1}^{+3.1}$	$2.4 \pm 0.1$
A1240-2	$-1.13 \pm 0.05$	$-0.97 \pm 0.05$	$4.0_{-0.6}^{+1.1}$	$2.3 \pm 0.1$

Notes: Col. 1: source name; Col. 2: integrated spectral index between 143 MHz and 3 GHz (Subsec. 3.3.1); Col. 3: injection spectral index calculated in the outer edge regions (Subsec. 3.3.1); Col. 4 – 5: Mach numbers derived from Col. 2 – 3, respectively.

resolution image (Fig. 3.3) we estimated the integrated flux over an area of radius of 3 arcmin – 5 arcmin (Fig. 3.3) is not higher than 25 – 69 mJy at 143 MHz at  $1\sigma_{\text{rms}}$  significance.

## 3.4 Discussion

### 3.4.1 Radio relics

Bonafede et al. (2009) discussed possible formation models for the radio relics in A1240. The models were associated with large-scale outward propagating shocks generated during the cluster merger and included (i) shock acceleration via Fermi-I process (Enßlin et al. 1998; Roettiger et al. 1999; Hoefl et al. 2007) and (ii) shock re-acceleration of fossil plasma via adiabatic compression (Enßlin & Gopal-Krishna 2001). Using our high-resolution, large-frequency range, and deep LOFAR, GMRT and VLA data, we discuss below the implications of our observational results (Sec. 3.3) in the framework of the relic formation models.

### **Injection spectral index and shock Mach number**

The predictions of particle (re-)acceleration models at shock fronts depends on the Mach number of shocks (e.g. Donnert et al. 2016; Kang & Ryu 2016) that is defined as follows,

$$\mathcal{M} = \frac{v_{\text{shock}}}{c_s}, \quad (3.3)$$

where  $v_{\text{shock}}$  is the shock speed and  $c_s$  is the sound speed in the upstream ICM. For simple planar shocks in the linear test particle regime of DSA,

the spectral index of the relativistic electrons that are injected at the shock front is a function of the Mach number (Blandford & Eichler 1987),

$$\alpha_{\text{inj}} = \frac{1}{2} - \frac{\mathcal{M}^2 + 1}{\mathcal{M}^2 - 1} \quad \text{or} \quad \mathcal{M} = \sqrt{\frac{2\alpha_{\text{inj}} - 3}{2\alpha_{\text{inj}} + 1}}. \quad (3.4)$$

where the injection spectral index  $\alpha_{\text{inj}} = (1 - \delta_{\text{inj}})/2$ , here  $\delta_{\text{inj}}$  is the power of the particle power spectrum,  $dN/dE \propto E^{-\delta_{\text{inj}}}$ .

The injection spectral index for a simple planar shock model has been commonly estimated in the literature by using an approximation,

$$\alpha_{\text{inj}} = \alpha_{\text{int}} + \frac{1}{2}, \quad (3.5)$$

where  $\alpha_{\text{int}}$  is the integrated spectral index of the relic. The advantage of this approach is that the measurement bias is free from the projection and synthesized beam effects as the integrated fluxes are measured over the whole region of the relic. However, in many clusters the Mach numbers derived from the integrated spectral index are higher than those estimated from X-ray data (e.g. Stroe et al. 2013; Akamatsu et al. 2015; Eckert et al. 2016). Furthermore, hydrodynamical simulations of cluster shocks indicate that the  $\alpha_{\text{inj}} - \alpha_{\text{int}}$  approximation (Eq. 3.5) does not hold for spherical expanding shocks as the shock speed decreases in time (Kang 2015a,b). A second method to estimate the injection spectral index is to directly measure at the shock front with sufficiently high-resolution spectral index maps (e.g. de Gasperin et al. 2015; van Weeren et al. 2016c; Hoang et al. 2017). It is noted that this direct measurement of the injection spectral index is only applicable to the shocks that are moving on/close the plane of the sky to minimize the mixing of different aged electrons. A third method to estimate the injection spectral index is to model the spectral ageing of the relics (Harwood et al. 2013, 2015; Stroe et al. 2014; de Gasperin et al. 2015). The spectral ageing modelling requires observations at least 4 frequencies to constrain the spectral curvature of the relics, which we are unable to do with our current data sets. The estimation of injection spectral indices for radio relics using the three approaches above have pros and cons which were discussed in the literature (e.g. Stroe et al. 2014; de Gasperin et al. 2015; Hoang et al. 2017).

In case of A1240, we estimated the integrated spectral indices between 143 MHz and 3 GHz to be  $-1.08 \pm 0.05$  and  $-1.13 \pm 0.05$  for A1240-1 and A1240-2, respectively (Subsec. 3.3.1). Using Eqs. 3.4 and 3.5, we estimated the injection spectral indices and the corresponding Mach numbers for the



relics to be  $-0.58 \pm 0.05$  and  $5.1_{-1.1}^{+3.1}$  for A1240-1 and  $-0.63 \pm 0.05$  and  $4.0_{-0.6}^{+1.1}$  for A1240-2. These Mach numbers are significantly higher than those (i.e.  $3.3 \pm 0.2$  and  $2.8 \pm 0.3$ , respectively) that were estimated with the VLA 325 MHz and 1.4 GHz data using the above approach reported in Bonafede et al. (2009). Using the second approach of measuring the injection spectral index directly at the shock front (Subsec. 3.3.1), we obtained injection spectral indices of  $-0.94 \pm 0.06$  and  $-0.97 \pm 0.05$  for the A1240-1 and A1240-2 shocks, respectively. The corresponding Mach numbers are  $2.4 \pm 0.1$  and  $2.3 \pm 0.1$ . The Mach numbers we have estimated are significantly different from each other. A possible reason for this discrepancy, as pointed out in Kang (2015a), is that the shock compression ratio and the flux of the injected relativistic electrons reduce as the shock speed decreases in time. These lead to a significant deviation of the integrated spectra of the relics from the power laws of the simple planar shock model which predicts the  $\alpha_{\text{inj}} - \alpha_{\text{int}}$  relation (Eq. 3.5). Therefore, the integrated spectra of the relics may be an inaccurate proxy for Mach numbers. However, the spectra of the relics at the location of the shock fronts are properly described by the DSA predictions (Kang 2015a) and should be used for the estimates of Mach numbers.

We analysed Chandra X-ray data to search for shocks at the relic locations. We fit the surface brightness (SB) with a function consisting of a  $\beta$ -model and a power law using PROFFIT (see, e.g., Eckert et al. 2011; Andrade-Santos et al. 2016). The X-ray SB profiles in Fig. 3.7 indicates possible discontinuities across A1240-1 and A1240-2 which would imply the presence of shocks or cold fronts at the location of the relics. To distinguish the nature of the possible discontinuities, a more detailed temperature map is required, which is not possible to make with the current shallow X-ray data. In Fig. 3.7, the SB profile has a break close to the central location of A1240-1 and a SB discontinuity towards the southern direction is found at the inner region of A1240-2. If the relics trace the candidate merger shocks, the locations of these breaks seem to be inconsistent with the DSA model that requires shock fronts to be located at the flattest spectral regions (i.e. the outer regions) of the relics which is where the relativistic electrons are (re-)accelerated (e.g. Enßlin et al. 1998; van Weeren et al. 2010). However, it is known that positional shifts between the relic and X-ray shock positions can occur due to the contamination of small-scale substructure behind the shock that is unresolved, by low-resolution X-ray observations (Ogrea et al. 2013b; van Weeren et al. 2016c), or due to the contamination of foreground X-ray emission in hydrodynamical simulations or due to projection

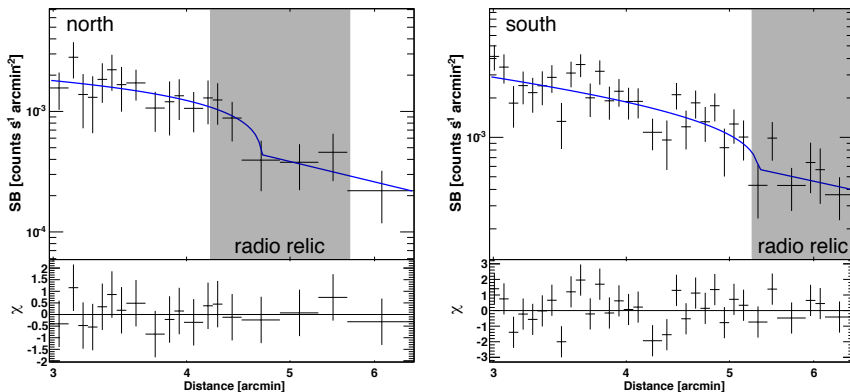


Figure 3.7: 52 ks Chandra 0.5 – 2.0 keV surface brightness profiles across A1240-1 (left) and A1240-2 (right). The blue lines are the fit of the data to a function consisting of a  $\beta$ -model and a power law.

effects (Hong et al. 2015). Finally, it is noted that the X-ray data is very shallow (i.e. exposure duration of 52 ks) and the apparent location of the shock fronts in Fig. 3.7 might be biased by the low S/N of the X-ray data.

In an attempt to obtain approximate estimates of the shock Mach numbers with the current X-ray data, we find that the best-fit density jumps would imply Mach numbers of  $\sim 2$  for both relics, assuming that the density jumps trace two shock fronts. These Mach numbers are in line with our estimates using the radio data (i.e.  $\mathcal{M}_{\text{inj}}$  in Table 3.4). However, future X-ray studies with deeper X-ray/SZ observations will be necessary to provide accurate constraints on the Mach numbers and the exact locations of the shock fronts.

### Acceleration efficiency and sources of relativistic electrons

A number of radio relics have been observed at the locations of merger shocks detected with X-ray observations (e.g. via surface brightness discontinuity and/or temperature jump). The shocks are generally thought to accelerate the ICM electrons to relativistic energies and are visible in the radio band under the presence of the large-scale,  $\mu\text{G}$  cluster magnetic field. The Mach numbers for the merger shocks are typically measured to be  $\lesssim 3$  from X-ray observations (e.g. Markevitch 2010; Akamatsu & Kawahara 2013). For these weak shocks, the efficiency to accelerate electrons to relativistic energies directly from the thermal pool can be challenging in the framework of DSA theory (e.g. Kang et al. 2012; Pinzke et al. 2013;

Brunetti & Jones 2014; Botteon et al. 2016a; Eckert et al. 2016; van Weeren et al. 2016c). Here the particle acceleration efficiency is defined as follows (Botteon et al. 2016a),

$$\eta = \frac{E_{\text{relic}}}{\Delta F_{\text{KE}}}, \quad (3.6)$$

where  $E_{\text{relic}}$  is the energy flux of the accelerated relativistic electrons at relic and  $\Delta F_{\text{KE}}$  is the kinematic energy flux available at the shock,

$$E_{\text{relic}} = \epsilon_{\text{e,down}} v_{\text{down}} \quad (3.7)$$

$$\Delta F_{\text{KE}} = 0.5 \rho_{\text{up}} v_{\text{shock}}^3 \left(1 - \frac{1}{C^2}\right), \quad (3.8)$$

where  $\epsilon_{\text{e,down}}$  and  $v_{\text{down}}$  are the downstream particle energy density and velocity, respectively;  $\rho_{\text{up}}$  is the upstream density;  $v_{\text{shock}}$  is the shock speed;  $C = \frac{(\gamma+1)\mathcal{M}^2}{(\gamma-1)\mathcal{M}^2+2}$  is the compression factor of a shock Mach number  $\mathcal{M}$  (here  $\gamma = 5/3$ ). The relativistic electrons in the downstream region were assumed to have a single-power law spectrum,  $N_{\text{inj}} \propto p^{-\delta_{\text{inj}}}$ . For details of the formulas, we refer to Botteon et al. (2016a).

In Fig. 3.8 we examine the particle acceleration efficiency for shocks with the injection indices (or Mach numbers) for the relics A1240-1 and A1240-2 (see Table 3.4). In the calculation, we used the downstream particle number densities  $\rho_{\text{A1240-1}} = (1-2) \times 10^{-4} \text{ cm}^{-3}$  and  $\rho_{\text{A1240-2}} = (2.5-3.5) \times 10^{-4} \text{ cm}^{-3}$ , which were derived by fitting of the electron density beta-model profile to the Chandra X-ray data. We also used the downstream temperature  $T_{\text{A1240-1}} = 5.1_{-0.8}^{+1.0} \text{ keV}$  and  $T_{\text{A1240-2}} = 5.4_{-0.8}^{+0.9} \text{ keV}$  (Barrena et al. 2009). The  $k$ -corrected radio power used for the relics in the calculation is  $P_{\text{A1240-1}}^{143 \text{ MHz}} = (7.52 \pm 0.17) \times 10^{24} \text{ W Hz}^{-1}$  and  $P_{\text{A1240-2}}^{143 \text{ MHz}} = (2.24 \pm 0.33) \times 10^{25} \text{ W Hz}^{-1}$  that we calculated from the LOFAR image (see Table 3.3). Given the equipartition magnetic field strength of  $\sim 2.5 \mu\text{G}$  in the relic regions (Bonafede et al. 2009), in the cases of higher Mach numbers (i.e. 4.0 for A1240-1 and 5.1 for A1240-2) the particle acceleration efficiencies that are required to produce the synchrotron emission in A1240-1 and A1240-2 are less than 1% and 0.5%, respectively. Although the precise efficiency of electron acceleration by the low Mach numbers of shocks associated with the relics is still an open question, these low efficiencies are likely to be realistic (Brunetti & Jones 2014). However, the required efficiencies for low Mach numbers (e.g.  $\lesssim 3$ ) are close to 100 percent which is challenging for DSA. To avoid the high efficiency problem, it is proposed that the low Mach number shocks

re-accelerate a pre-existing population of relativistic electrons, instead of accelerating the thermal electrons (e.g. Markevitch et al. 2005; Kang & Ryu 2011; Kang et al. 2012). The pre-existing fossil plasma could originate from radio galaxies that are close to the relics. To search for sources of possible fossil plasma, we obtained the redshifts from the Subaru and SDSS optical data (Golovich et al. 2017a) for the radio galaxies (i.e. A, B, C, E, F in Fig. 3.2) that have small angular separations to A1240-1 and A1240-2. The galaxies C ( $z = 0.888 \pm 0.0979$ ) and E ( $z = 0.448 \pm 0.0289$ ) are background sources and D has no redshift information. The radio galaxies A ( $z = 0.19299 \pm 0.00003$ ), B ( $z = 0.19223 \pm 0.00005$ ), and possibly F ( $z = 0.152 \pm 0.0263$ ) are close to the cluster mean redshift ( $z = 0.1948$ ) and are possibly sources of mildly relativistic electrons that could be associated with the synchrotron radio emission in the relics. An example of this scenario was observed in Abell 3411-3412 where fossil electrons from a radio galaxy have been suggested to be re-accelerated by a merger shock which disturbs the morphology of the tails at the location of the shock and re-flattens the spectral index of the tails at the location of the shock (van Weeren et al. 2017). Other less obvious examples are found in PLCKG287.0+32.9 (Bonafede et al. 2014) and the Bullet cluster 1E 0657-55.8 (Shimwell et al. 2015). As our radio data presented in Figs. 3.1 and 3.2 are not deep enough to provide information on whether A, B and F are connected to A1240-1 and A1240-2 and do not allow us to study the spectral index trend of the sources, future deeper, high-resolution radio observations will be necessary to establish such a connection.

### Size and power of the double relics

In the DSA model, the extent of radio relics is the same as the size of the shock fronts which (re-)accelerate in situ the relativistic electrons in the relics (e.g. Jaffe 1977; Blandford & Eichler 1987; Enßlin et al. 1998). In merging clusters that host double radio relics on opposite sides of the cluster centre, the relative largest linear size (LLS) of the relics depends on the mass ratio of the sub-clusters, as demonstrated in, e.g., hydrodynamical simulations of ideal binary cluster merger by van Weeren et al. (2011a). In these simulations, the sub-cluster mass ratio is varied to match the observed LLSs of double relics (i.e. in the Sausage cluster). The larger relic is found to be behind the more massive sub-cluster. Although the mass configuration (i.e. ratio of 1 – 3 : 1) in the simulations might be inconsistent with the reconstructed mass distribution in the weak lensing data (i.e. mass ratio  $\sim 1$  in Jee et al. 2015 or  $\sim 1 : 2$  in Okabe et al. 2015), this might be because

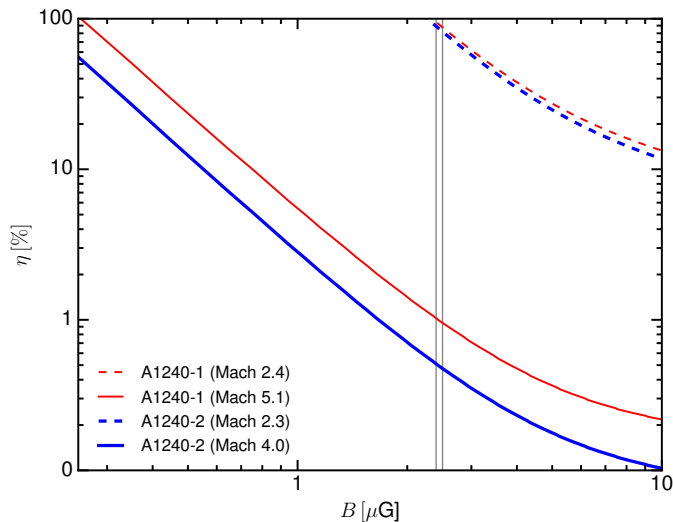


Figure 3.8: Particle acceleration efficiency  $\eta(B)$  required to produce the radio surface brightness in the relics of A1240. The vertical lines indicate the equipartition magnetic field  $2.4\mu\text{G}$  and  $2.5\mu\text{G}$  in A1240-1 and A1240-2, respectively (Bonafede et al. 2009). Calculations assume a minimum momentum of electrons  $p_{\min} = 0.1m_e c$ .

the observed LLS of the faint, steep spectrum relic were biased low by the sensitivity limitations of the high-frequency radio observations used in van Weeren et al. (2011a). We note that the error bars associated with the weak lensing analyses are so large that it is not clear there is real discrepancy. In support of this, it is known that the LLS of the small relic is much larger and almost equal to the main relic (Hoang et al. 2017). It is also noted that the observed LLS of a relic also depends on mass concentration of the sub-clusters prior to merger. In line with the simulations in van Weeren et al. (2011a), a number of merging clusters are observed to host more massive sub-clusters behind the main relics (e.g. ZwCl 0008.8+5215 in van Weeren et al. 2011b, Golovich et al. 2017b; RX J0603.3+4214 in van Weeren et al. 2016c, Jee et al. 2016; and PLCK G287.0+32.9 in Bonafede et al. 2014, Finner et al. 2017).

In A1240, the projected LLS of A1240-2 in the south is a factor of 2 larger than that of A1240-1 in the north (i.e. 1.35 and 0.68 Mpc, respectively; see Subsec. 3.3.1). This implies that the southern shock front is larger in projection than the north one. Unfortunately, we are unable to check this with the current shallow X-ray data. However, if this turns out to be the case and the mass concentration of the sub-clusters is similar,

the sizes of the shock fronts is likely different because the masses of the sub-clusters prior to the merger are not equal. The sub-cluster that is more massive (or larger in size) should generate a larger shock surface in front of its direction of propagation during a major cluster merger. This scenario might be applied for A1240 as the cluster is known to be observed 0.3 Gyr after core crossed (Barrena et al. 2009). The southern sub-cluster, which comes from the north before the merger, is more massive (about 2.8 times; Barrena et al. 2009) than the northern sub-cluster and generates a wider shock in the south than the northern counter shock.

The radio power at 143 MHz for A1240-2 is a factor of  $\sim 3$  more powerful than that for A1240-1 (see Subsec. 3.4.1). This is surprising because the radio derived Mach number for A1240-2 is smaller or equal to that for A1240-1 (Table 3.4). This might be because the surface area in the southern shock is larger than that in the northern shock which might be due to the difference in the mass of the sub-clusters, as we discussed above. The true reason is still unclear as the synchrotron power of the relics under DSA model is a function of many parameters (e.g. shock surface area, electron density, magnetic field strengths, ICM temperature, particle acceleration efficiency at the shocks; Eq. 32 in Hoeft et al. 2007) that are poorly constrained with the current data. Other possibilities for the difference in the power of the relics are that the relativistic electrons in the relics are re-accelerated from fossil plasma and the radio power depends on the fossil plasma populations (e.g. van Weeren et al. 2016c) or the Mach numbers derived from radio spectrum are not an approximate proxy for the X-ray shock Mach numbers (e.g. Akamatsu et al. 2015, 2017; van Weeren et al. 2016c).

### Viewing angle of the merger axis

The radio emission from the relics A1240-1 and A1240-2 (Fig. 3.6) is highly polarized. The electric field vectors are roughly perpendicular to the major axes of the relics which implies an alignment of magnetic fields along the major axes of the relics. At the shock fronts, the magnetic field alignments are likely to be caused by shock compression. Since the polarized emission is a vector quantity, the fractional polarization as measured by an observer depends on the viewing angle  $\theta$  and the compression factor  $C = (\alpha_{\text{int}} - 1)/(\alpha_{\text{int}} + \frac{1}{2})$  (assuming a polytropic index of the ICM gas of  $\gamma_{\text{gas}} = 5/3$ , Enßlin et al. 1998). The viewing angle here is the projection angle between the normal of the shock front and the line from the observers to the shock; for example,  $\theta = 0^\circ$  or  $90^\circ$  means that the shock is occurring along the

LOS or in the plane of the sky, respectively. In cases of a weak magnetic field or small ratio of the magnetic pressure to internal gas pressure (i.e.  $P_B/P_{\text{thermal}} = \frac{B^2}{8\pi\rho RT}$ , where  $B$  is magnetic field,  $\rho$  is thermal electron density,  $R$  is ideal gas constant,  $T$  is thermal gas temperature), the observed mean fractional polarization of a shock is estimated as following (Enßlin et al. 1998),

$$\bar{F} \leq \frac{\delta_{\text{int}} + 1}{\delta_{\text{int}} + \frac{7}{3}} \frac{\sin^2(\theta)}{\frac{2C^2}{C^2-1} - \sin^2(\theta)}, \quad (3.9)$$

where  $\delta_{\text{int}} = 1 - 2\alpha_{\text{int}}$  is the slope of the electron density spectrum. The  $\leq$  sign indicates that the observed polarized emission might further experience depolarization effects due to, e.g., the spatial resolution of the observations or wide bandwidth imaging. In case of A1240, we estimated the magnetic field to thermal pressure ratios of  $\sim 18\%$  for A1240-1 and  $\sim 9\%$  for A1240-2, which implies that the relics are located in a region that satisfies the weak magnetic field criteria. Here we used the magnetic field strength (i.e.  $B_{\text{A1240-1}} = 2.4 \mu\text{G}$ ,  $B_{\text{A1240-2}} = 2.5 \mu\text{G}$ ) estimated in Bonafede et al. (2009), the particle upstream densities (i.e.  $\rho_{\text{A1240-1}} = 1.5 \times 10^{-4} \text{cm}^{-3}$ ,  $\rho_{\text{A1240-2}} = 3.0 \times 10^{-4} \text{cm}^{-3}$ ) calculated in Sec. 3.4.1 and the thermal temperature (i.e.  $T_{\text{A1240-1}} = 5.1 \text{keV}$  and  $T_{\text{A1240-2}} = 5.4 \text{keV}$ ) measured in Barrena et al. (2009).

To examine the possible viewing angles of the relics A1240-1 and A1240-2, we plot the fractional polarization  $\bar{F}$  of the relics as a function of viewing angle  $\theta$  in Fig. 3.9. Here we used the integrated spectral indices of  $-1.08 \pm 0.05$  and  $-1.13 \pm 0.05$  for A1240-1 and A1240-2, respectively (Subsec. 3.3.1). Since the polarization measured from the VLA 2 – 4 GHz data might be slightly depolarized due to the wide-bandwidth, we used the mean fractional polarization that was measured from the VLA images (bandwidth of 480 MHz, see Subsec. 3.3.1). The mean fractional polarization measured from the VLA data sets are  $32 \pm 4\%$  and  $17 \pm 4\%$  for A1240-1 and A1240-2, respectively. These correspond to the viewing angles of  $\theta_{\text{A1240-1}} \geq 53 \pm 3^\circ$  and  $\theta_{\text{A1240-2}} \geq 39 \pm 5^\circ$  (i.e. via Eq. 3.9). The estimated viewing angles are in agreement with the constraints from the two-body modelling using optical redshift data that the cluster merger likely occurred in the plane of the sky (Barrena et al. 2009).

### 3.4.2 Radio halo and cluster mass

Cassano et al. (2013) reports the relation between the power of radio haloes and the cluster mass (i.e. the  $P_{1.4 \text{ GHz}} - M_{500}$  relation). The power of radio

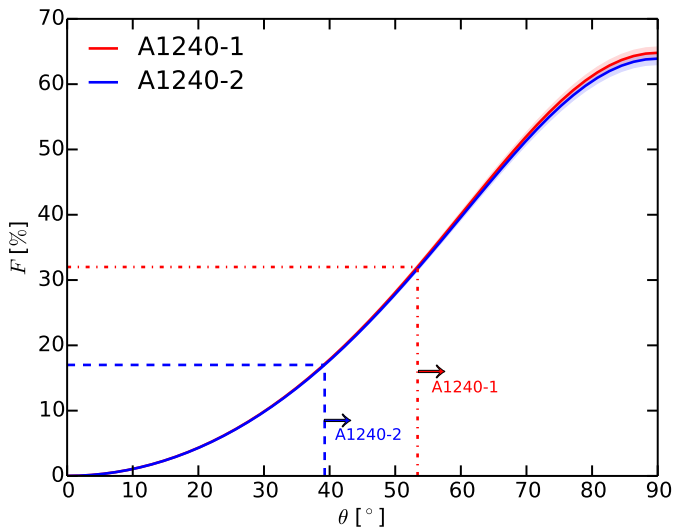


Figure 3.9: Fractional polarization of the relics A1240-1 and A1240-2 as a function of viewing angle. The mean fractional polarization of A1240-1 and A1240-2 was measured to be  $32 \pm 4\%$  and  $17 \pm 4\%$  from the 480 MHz-bandwidth data chunks (Subsec. 3.3.1), which correspond to viewing angles of  $\theta_{\text{A1240-1}} \geq 53 \pm 3^\circ$  (red arrow) and  $\theta_{\text{A1240-2}} \geq 39 \pm 5^\circ$  (blue arrow), respectively.

haloes increases as a function of cluster mass, implying that more gravitational energy is channelled into the radio emission in more massive merging clusters. A number of low-mass ( $\sim 10^{14} M_\odot$ ) merging clusters have also been detected to host radio haloes. However, diffuse emission has not been observed in the central regions of some clusters in a similar mass range (e.g. Abell 2345 in Bonafede et al. 2009, ZwCl 2341.1+0000 in van Weeren et al. 2009, ZwCl 0008.8+5215 in van Weeren et al. 2011b, PSZ1 G096.89+24.17 in de Gasperin et al. 2014). The question remains as to what fraction of merging galaxy clusters are not able to generate radio haloes or whether the non-detection is simply due to the sensitivity limitation of the current radio observations. In case of A1240, our LOFAR 143 MHz data (Fig. 3.3) shows no evidence of diffuse emission in the central region of the cluster despite of the fact that its ICM is highly disturbed. In this subsection, we use the LOFAR data to constrain the upper limit for the flux of the radio halo. We assume that the spectral index for the halo is  $\alpha_{\text{int}} = 1.3 \pm 0.2$  (i.e. the typical spectral index for a number of known haloes; Feretti et al. 2012) and the radio power is  $k$ -corrected for the redshift of the cluster.



Table 3.5: Upper limits for the radio halo power of A1240.

Region	$P_{1.4 \text{ GHz}} [10^{23} \text{ W Hz}^{-1}]$
Circle ( $R_{\text{H}} = 264 \text{ kpc}$ )	$0.30 \pm 0.14$
Circle (mock injection)	$0.29 \pm 0.13$
Ellipse (from Figs. 3.3)	$2.2 \pm 1.0$
Ellipse (mock injection)	$1.4 \pm 0.6$

### Upper limit for halo flux from the LOFAR data

Given the cluster mass of  $M_{500} = (3.7 \pm 0.4) \times 10^{14} M_{\odot}$  (Planck Collaboration et al. 2016), we found the predicted power for A1240 to be  $P_{1.4 \text{ GHz}} = (1.9 \pm 0.9) \times 10^{23} \text{ W Hz}^{-1}$ . The power of radio haloes is also found to be directly proportional to their radii,  $R_{\text{H}} = \sqrt{R_{\text{min}} \times R_{\text{max}}}$ , where  $R_{\text{min}}$  and  $R_{\text{max}}$  are the minimum and maximum radii of the haloes (e.g. Cassano et al. 2007). Using the  $P_{1.4 \text{ GHz}} - R_{\text{H}}$  relation in Cassano et al. (2007), we estimate that the radius for the halo in A1240 is  $R_{\text{H}} = 264 \text{ kpc}$ , which is significantly smaller than half of the distance between A1240-1 and A1240-2 (i.e. 900 kpc).

The  $1\sigma_{\text{rms}}$  upper limit for the flux of non-detected diffuse emission is commonly estimated as  $S = A \times \sigma_{\text{rms}}$ , where  $A$  is the area emitting the expected diffuse emission. Given the sensitivity of the LOFAR data (Fig. 3.3), we estimated that the halo flux at 143 MHz is at most  $S_{143 \text{ MHz}} = A \times \sigma_{\text{rms}} = 5.1 \text{ mJy}$ , where  $\sigma_{\text{rms}} = 410 \mu\text{Jy beam}^{-1} = 0.244 \mu\text{Jy arcsec}^{-2}$  and  $A = \pi R_{\text{H}}^2 = 21 \times 10^3 \text{ arcsec}^2$ , corresponding to a radius of 264 kpc. The derived upper limit for the halo power at 1.4 GHz is  $P_{1.4 \text{ GHz}} = (3.0 \pm 1.4) \times 10^{22} \text{ W Hz}^{-1}$ . Our estimated  $1\sigma_{\text{rms}}$  upper limit for the radio halo is  $\sim 6 - 12$  times smaller than the value predicted from the  $P_{1.4 \text{ GHz}} - M_{500}$  relation (i.e.  $P_{1.4 \text{ GHz}} = (1.9 \pm 0.9) \times 10^{23} \text{ W Hz}^{-1}$ ; Cassano et al. 2013). The radio halo in A1240 is therefore underluminous in comparison with the prediction of the  $P_{1.4 \text{ GHz}} - M_{500}$  relation if it has a small radius (i.e.  $R_{\text{H}}$ ). Several other double-relic clusters are observed to host small haloes (e.g. Brown et al. 2011a; Bonafede et al. 2012; de Gasperin et al. 2015). But it is noted that the apparent sizes of faint radio haloes might be biased due to, e.g., the depth or  $uv$ -coverage of the observations.

In the post-shock turbulence acceleration scenario, the turbulence is produced by the baroclinic effects at the shocks, where the pressure gradients are not in parallel with the downstream total plasma (Brunetti & Jones 2014). Suggested by the Fermi-II process, the radio halo emission may start from the inner edges of the relics, or behind the shocks, and approximately

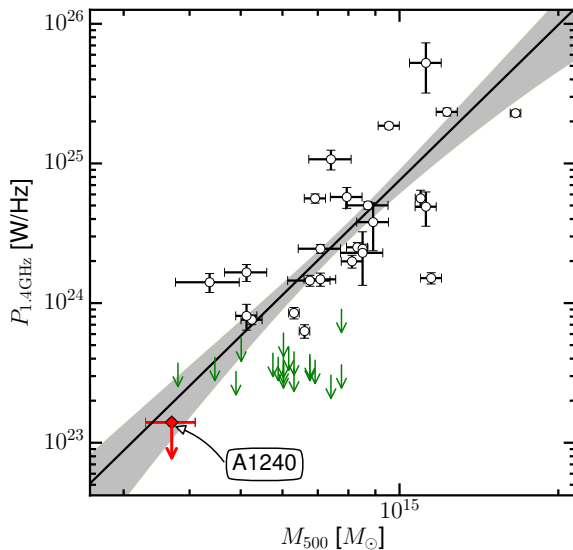


Figure 3.10: The  $P_{1.4 \text{ GHz}} - M_{500}$  relation of radio haloes (i.e.  $P_{1.4 \text{ GHz}} [10^{24} \text{ W Hz}^{-1}] = 10^{-2.82 \pm 0.51} \times M_{500}^{3.70 \pm 0.56} [10^{14} M_{\odot}]$ ; i.e. BCES bisector fitting for all detected haloes in Cassano et al. 2013). The upper limits of the radio halo for A1240,  $P_{1.4 \text{ GHz}} = (1.4 \pm 0.6) \times 10^{23} \text{ W Hz}^{-1}$  (red arrow), that we estimated from the LOFAR 143 MHz data in Subsec. 3.4.2. The green down arrows indicate upper limits for the undetected radio haloes (see Cassano et al. 2013 for the cluster list). The grey region indicate the 95% confidence region of the best-fit.

trace the X-ray emission (e.g. van Weeren et al. 2016c; Hoang et al. 2017). If the radio halo of A1240 follows a similar trend, the size of the halo should be approximately equal to the distance between A1240-1 and A1240-2 (i.e.  $\sim 1.8 \text{ Mpc}$  in projection). If we assume the halo emission encompasses the region shown by the ellipse in Fig. 3.3 then the  $1\sigma_{\text{rms}}$  upper limit of the radio flux is significantly higher at  $S_{143 \text{ MHz}} = A \times \sigma_{\text{rms}} = 37.2 \text{ mJy}$ , where  $A = 152.6 \times 10^3 \text{ arcsec}^2$ . The ellipse has semi-minor and semi-major axes of 3 and 4.5 arcmin, respectively. The position angle of the ellipse is  $160^\circ$  (the north-south axis being the reference, the counter-clockwise being positive direction). The corresponding limit on the 1.4 GHz radio power is  $P_{1.4 \text{ GHz}} = (2.2 \pm 1.0) \times 10^{23} \text{ W Hz}^{-1}$ , which is not discrepant from that predicted by the  $P_{1.4 \text{ GHz}} - M_{500}$  relation (i.e.  $P_{1.4 \text{ GHz}} = (1.9 \pm 0.9) \times 10^{23} \text{ W Hz}^{-1}$ ; see Fig. 3.10). Hence, even though we do not detect the halo, its expected power should be close to the detection limit of our observations.

### Upper limit of halo flux from simulations

Beside the uncertainty in the predictions of the halo size and its radio power, other possibilities for the non-detection of diffuse emission in the cluster centre are due to (i) the limited  $uv$ -coverage of the interferometric observations (see, e.g., Venturi et al. 2008) and (ii) the algorithms used in the data reduction procedure.

To examine (i), we generated a mock image for the radio halo with a surface brightness that follows an exponential function  $I(r) = I_0 \exp(-\epsilon/r_e)$ , where  $\epsilon = \frac{x^2}{a^2} + \frac{y^2}{b^2} \leq 1$  defines the projected shape of the diffuse emission (Bonafede et al. 2017);  $I_0$  and  $r_e$  are free parameters (Murgia et al. 2009). The mock halo has a peak brightness of  $I_0 = 3\sigma_{\text{rms}} = 0.732 \mu\text{Jy arcsec}^{-2}$ , an effective radius of  $r_e = 102 \text{ kpc}$  and an integrated flux of  $100.4 \text{ mJy}$  at  $143 \text{ MHz}$  over the elliptical region ( $a = 582 \text{ kpc}$  and  $b = 873 \text{ kpc}$ ) in Figs. 3.3 and 3.11. The halo model was injected (i.e. Fourier transformed) into a blank column of the LOFAR data set that does not include sources nor background noise. The injected  $uv$ -data were then deconvolved with the MS – MFS options in CASA (see Subsec. 3.2.4) to obtain the mock halo. The integrated flux for the mock halo that was measured in the deconvolved image is  $95.9 \text{ mJy}$  which is  $\sim 95\%$  of the integrated flux of the injected mock halo. This implies that the LOFAR observations are sensitive to the  $143 \text{ MHz}$ ,  $\sim \mu\text{Jy arcsec}^{-2}$  diffuse emission of scales equivalent to the separation of the relics in A1240.

To search for the upper limit of the halo flux, we follow the procedure described in Bonafede et al. (2017). We vary the integrated fluxes (i.e. using  $I_0$ ) and inject the elliptical model ( $a = 582 \text{ kpc}$ ,  $b = 873 \text{ kpc}$  and  $r_e = 102 \text{ kpc}$ ) to the LOFAR data column.  $I_0$  is varied in steps of  $0.5\sigma_{\text{rms}}$ , followed by fine steps of  $0.1\sigma_{\text{rms}}$  between  $1 - 2\sigma_{\text{rms}}$ . We found that no extended emission (i.e. size of  $\geq R_{\text{H}}$ ) is detected in the deconvolved images (Fig. 3.11) at  $2\sigma_{\text{rms}}$  when the integrated flux of the injected model is  $\leq 36.8 \text{ mJy}$  (i.e.  $I_0 = 1.1\sigma_{\text{rms}}$ ). The corresponding radio power at  $1.4 \text{ GHz}$  is  $P_{1.4 \text{ GHz}} = (1.4 \pm 0.6) \times 10^{23} \text{ W Hz}^{-1}$ . This injected power can be considered as the approximate upper limit of the halo power and is consistent with our  $1\sigma_{\text{rms}}$  estimate (i.e.  $P_{1.4 \text{ GHz}} = (2.2 \pm 1.0) \times 10^{23} \text{ W Hz}^{-1}$  at  $143 \text{ MHz}$ ) using the LOFAR low-resolution image. It is noted here that the halo emission is assumed to be distributed over an elliptical region between A1240-1 and A1240-2. In case that the  $P_{1.4 \text{ GHz}} - R_{\text{H}}$  relation holds for A1240, the halo would be smaller (i.e.  $a = b = R_{\text{H}} = 264 \text{ kpc}$ ) and the upper limit for the halo power derived from simulations is  $P_{1.4 \text{ GHz}} = (2.9 \pm 1.3) \times 10^{22} \text{ W Hz}^{-1}$ . This is  $\sim 6$  times lower than the value derived from the VLA  $1.4 \text{ GHz}$  data

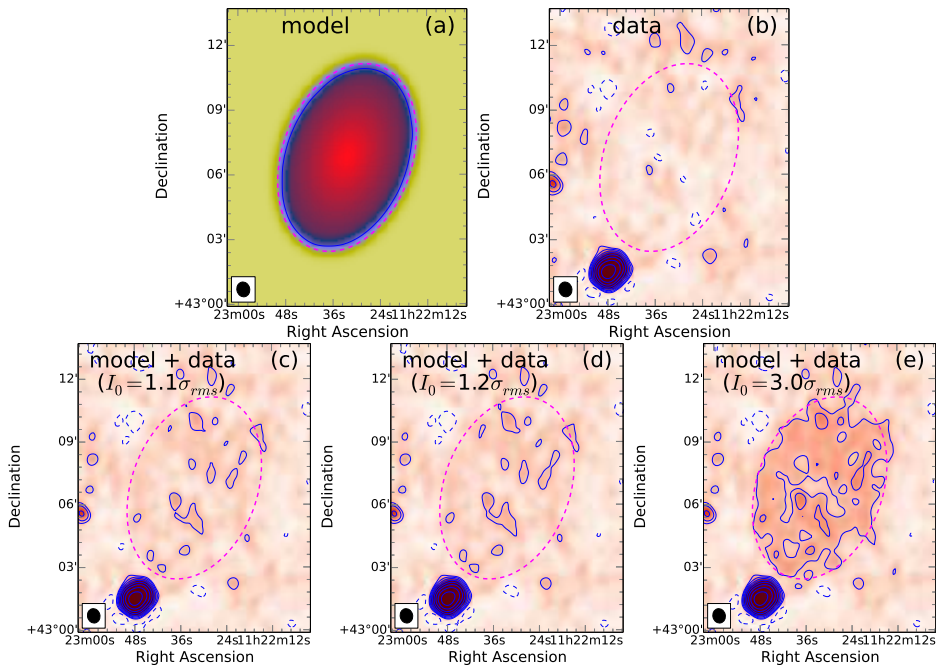


Figure 3.11: Injection of halo models to the LOFAR data. (a) An example of the injected model for the halo (smoothed to 41 arcsec  $\times$  36 arcsec resolution). (b) LOFAR image of the region where the halo model is injected. (c-e) LOFAR images after the halo models of various peak brightness  $I_0$  are injected. The contours start at  $\pm 2$  and are spaced with a factor of 2. The size of the elliptical region is identical to that in Fig. 3.3.

in Bonafede et al. (2017) and is  $\sim 7$  times below the value predicted by the  $P_{1.4\text{ GHz}} - M_{500}$  relation. The amount of flux that is recovered from the deconvolved images depends on the brightness of the injected halo model and the regions where the integrated flux is measured, as shown in Fig. 3.12 for the case of the elliptical model for the halo.

The second possibility (ii) for the absence of the radio halo is beyond the scope of this paper as it requires mock haloes to be corrupted with realistic direction-independent and direction-dependent effects and injected into the  $uv$ -data prior to processing.

### 3.5 Conclusions

A1240 is a galaxy cluster in the process of merging (Bonafede et al. 2009; Barrena et al. 2009). Previous radio observations with the VLA (325 MHz

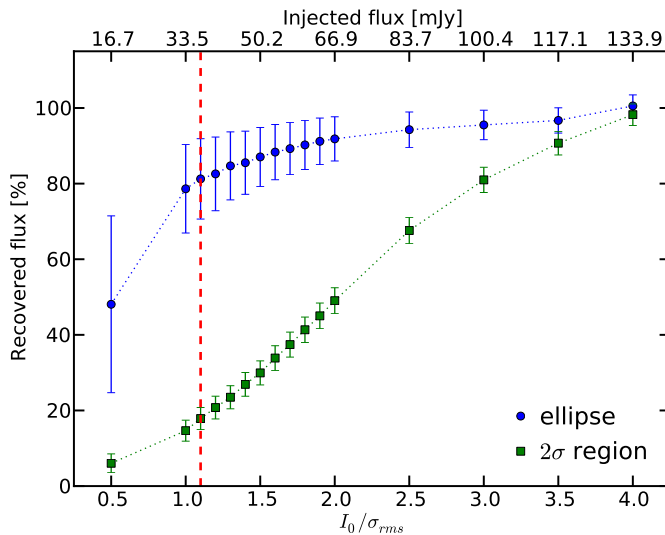


Figure 3.12: Recovered flux for the radio halo depends on the S/N of the injected elliptical model. The recovered fluxes are measured within the elliptical region and the  $\geq 2\sigma_{rms}$  region (see Fig. 3.11). The vertical dashed line indicates the upper limit for the halo flux (i.e. Fig. 3.11, c).

and 1.4 GHz) by Bonafede et al. (2009) characterised two radio relics in the peripheral regions of the cluster. In this paper, we performed LOFAR 143 MHz observations of the cluster and combined these with archival GMRT 612 MHz and VLA 3 GHz data. With the wide frequency range and deep observations, we provided new measurements on the spectral and polarimetric properties of the emission from the cluster relics and added further constraints on the existence of a radio halo. Below we summarize our results.

- From the 143 MHz – 3 GHz spectral index map we measured a spectral gradient across the width of the relics A1240-1 and A1240-2. The spectral indices steepen from  $-0.94 \pm 0.05$  and  $-0.97 \pm 0.05$  at the outer edges to  $-1.18 \pm 0.05$  and  $-1.23 \pm 0.05$  at the inner edges for A1240-1 and A1240-2, respectively. Using the spectral index values at the locations of the shock fronts and assuming DSA, the corresponding Mach numbers for the shocks are  $\mathcal{M} = 2.4 \pm 0.1$  and  $\mathcal{M} = 2.3 \pm 0.1$ , respectively. These Mach numbers are significantly lower than those (i.e.  $\mathcal{M}_{A1240-1} = 5.1^{+3.1}_{-1.1}$  and  $\mathcal{M}_{A1240-2} = 4.0^{+1.1}_{-0.6}$ ) estimated from the integrated spectral indices.

- At 2–4 GHz, we detected polarized emission in the regions of A1240-1 and A1240-2. The mean fractional polarization as measured from the VLA 480 MHz bandwidth data sets are  $32 \pm 4\%$  and  $17 \pm 4\%$  for A1240-1 and A1240-2, respectively. From these fractional polarization measurements we constrained the lower limits of the viewing angle of the merger axis to be  $53 \pm 3^\circ$  and  $39 \pm 5^\circ$  for A1240-1 and A1240-2, respectively.
- The magnetic field to thermal pressure ratio was estimated to be  $\sim 18\%$  and  $\sim 9\%$  in the regions of A1240-1 and A1240-2, respectively.
- The spectral gradients and polarimetric properties for the relics are consistent with the scenario that the relics were generated from shocks that are moving outwards. If the Mach numbers are 4.0 for A1240-1 and 5.1 for A1240-2, the required efficiency to accelerate electrons is less than 1% and 0.5%, respectively, suggesting that the relativistic electrons in the relics might be accelerated directly from the thermal pool. If the relics have low Mach numbers (e.g. below 3), fossil electrons from radio galaxies in A1240 existing prior to the shock passage will be required.
- With the sensitivity of our current LOFAR 143 MHz data, no hints of diffuse emission in the central regions of A1240 and A1237 were detected. Furthermore, no emission was observed in the region between the clusters. In the case that the A1240 halo spans the entire region (i.e. the ellipse in Fig. 3.3) between the relics, our upper limit for the radio halo power of A1240 by injecting of halo models is  $P_{1.4 \text{ GHz}} = (1.4 \pm 0.6) \times 10^{23} \text{ W Hz}^{-1}$  which is consistent with the expected power from the  $P_{1.4 \text{ GHz}} - M_{500}$  scaling relation. However, in case of small halo (i.e. circle of radius  $R_{\text{H}} = 264 \text{ kpc}$ ) the estimated upper limit (i.e.  $P_{1.4 \text{ GHz}} = (2.9 \pm 1.3) \times 10^{22} \text{ W Hz}^{-1}$ ) is  $\sim 7$  times below the  $P_{1.4 \text{ GHz}} - M_{500}$  relation. Our analysis suggests that we can reasonably exclude the presence of a small ( $R_{\text{H}} = 264 \text{ kpc}$ ) radio halo in A1240, while we cannot exclude the presence of a large elliptical radio halo extending between the two relics, since in this case our upper limit is consistent with the  $P_{1.4 \text{ GHz}} - M_{500}$  correlation.

## Acknowledgements

We thank the anonymous referees for the helpful comments. DNH, TS, RJvW and HR acknowledge support from the ERC Advanced Investigator programme NewClusters 321271. GB and RC acknowledge partial support from grant PRIN-INAF2014. AB acknowledges support from the ERC-Stg17 714245 DRANOEL. HA acknowledges the support of NWO via a Veni grant. SRON is supported financially by NWO, the Netherlands Organization for Scientific Research. GJW gratefully thanks the Leverhulme Trust for funding. This paper is based (in part) on results obtained with LOFAR equipment. LOFAR (Haarlem et al. 2013) is the Low Frequency Array designed and constructed by ASTRON. We thank the staff of the GMRT that made these observations possible. GMRT is run by the National Centre for Radio Astrophysics of the Tata Institute of Fundamental Research. The National Radio Astronomy Observatory is a facility of the National Science Foundation operated under cooperative agreement by Associated Universities, Inc. The scientific results reported in this article are based in part on data obtained from the Chandra Data Archive, observations made by the Chandra X-ray Observatory and published previously in cited articles. This research has made use of software provided by the Chandra X-ray Center (CXC) in the application packages CIAO, ChIPS, and Sherpa. This work was performed under the auspices of the U.S. Department of Energy by Lawrence Livermore National Laboratory under Contract DE-AC52-07NA27344. We thank J. J. Harwood for discussions on the possibility of modelling of spectral ageing of radio relics.

# 4 | Radio observations of the merging galaxy cluster Abell 520

## Abstract

Extended synchrotron radio sources are often observed in merging galaxy clusters. Studies of the extended emission helps us to understand the mechanisms in which the radio emitting particles gain their relativistic energies. We examine the possible acceleration mechanisms of the relativistic particles that are responsible for the extended radio emission in the merging galaxy cluster Abell 520. We perform new 145 MHz observations with LOFAR and combine these with the archival GMRT 323 MHz and VLA 1.5 GHz data to study the morphological and spectral properties of the extended cluster emission. The observational properties are discussed in the framework of particle acceleration models associated with cluster merger turbulence and shocks. In Abell 520, we confirm the presence of extended ( $760 \times 950 \text{ kpc}^2$ ) synchrotron radio emission that has been classified as a radio halo. The comparison between the radio and X-ray brightness suggests that the halo might originate in a cocoon rather than from the central X-ray bright regions of the cluster. The halo spectrum is roughly uniform on the scales of 66 kpc. There is a hint of spectral steepening from the SW edge towards the cluster center. Assuming the diffusive shock acceleration (DSA), the radio data is suggestive of a shock Mach number of  $\mathcal{M}_{\text{SW}} = 2.6_{-0.2}^{+0.3}$ , consistent with the X-ray derived estimates. This is in agreement with the picture that the relativistic electrons in the SW radio edge gain their energies at the shock front via the Fermi-I acceleration of either thermal or fossil electrons. We do not detect extended radio emission ahead of the SW shock that is predicted if the emission is the result of adiabatic compression. An X-ray surface brightness discontinuity is detected towards the NE region which may be a counter shock of Mach number  $\mathcal{M}_{\text{NE}}^{\text{X}} = 1.52 \pm 0.02$ . This is lower than the value predicted from the radio emission which, assuming DSA, is consistent with  $\mathcal{M}_{\text{NE}} = 2.1 \pm 0.2$ . Our observations indicate that the radio emission in the SW of Abell 520 is likely effected by the prominent X-ray detected shock where radio emitting particles are (re-)accelerated through the Fermi-I mechanism. The NE X-ray discontinuity that is approximately collocated with an edge in the



radio emission hints at the presence of a counter shock.

D. N. Hoang, T. W. Shimwell, R. J. van Weeren, et al.,  
*Astronomy & Astrophysics*, 622, A20 (2019)

## 4.1 Introduction

Non-thermal components, i.e. relativistic particles and magnetic fields, in the intra-cluster medium (ICM) are important tracers of the formation and evolution of large-scale structures. Their origin, and the role they play on the physical processes in the ICM, during cluster mergers are still being investigated. There is evidence that extended synchrotron emission, namely haloes and relics, can be generated during the mergers of sub-clusters/groups during which a part of the gravitational energy goes into particle acceleration and amplification of large-scale magnetic fields (for reviews, see Bruggen et al. 2012; Feretti et al. 2012; Brunetti & Jones 2014).

Radio haloes are Mpc-scale, faint synchrotron sources that are approximately co-spatial with the thermal emission from the ICM. At moderate observing resolutions, they are measured to be unpolarized down to a few per cent at  $\sim$  GHz frequencies. The mechanism of particle acceleration is powered by turbulence that is introduced during a merging event (e.g. Brunetti et al. 2001; Petrosian 2001; Fujita et al. 2003; Cassano & Brunetti 2005; Brunetti & Lazarian 2007, 2016; Pinzke et al. 2017). Hadronic CR proton-proton collisions in the ICM may also contribute to the observed radiation as they produce secondary relativistic electrons (e.g. Dennison 1980; Blasi & Colafrancesco 1999; Dolag & Ensslin 2000; Miniati et al. 2001; Pfrommer & Enßlin 2004; Pfrommer 2008; Keshet & Loeb 2010; Enßlin et al. 2011). However, current limits from the Fermi-LAT severely challenge a scenario of pure hadronic models for radio haloes (e.g. Jeltama & Profumo 2011; Brunetti et al. 2012; Zandanel et al. 2014; Ackermann et al. 2010, 2016) still leaving open the possibility of hadronic models where secondary particles are re-accelerated by turbulence Brunetti & Lazarian (2011a); Brunetti et al. (2017); Pinzke et al. (2017).

Radio relics are faint, elongated synchrotron sources in the peripheral regions of galaxy clusters. These can have projected sizes up to  $\sim$  Mpc and are often measured to have a high degree of polarization, up to 70 per cent. Relics are thought to form due to merger or accretion shocks which accelerate particles to relativistic energies via e.g. the Fermi-I diffusive shock acceleration (DSA; e.g. Enßlin et al. 1998; Roettiger et al. 1999; Enßlin & Gopal-Krishna 2001; Pfrommer 2008). However, the merger shocks with Mach number of  $\mathcal{M} \lesssim 5$  might be insufficient to generate the observed brightness and the spectra of relics in a number of clusters (e.g. Stroe et al. 2013; van Weeren et al. 2013, 2016c, 2017; Bonafede et al. 2014; Akamatsu et al. 2015; Shimwell et al. 2015; Vazza et al. 2015; Botteon

et al. 2016a; Hoang et al. 2017, 2018a). To overcome this problem, a pre-existing population of fossil electrons which is re-accelerated at shock is required to be present prior to the shock passage (e.g. Markevitch et al. 2005; Kang & Ryu 2011; Kang et al. 2012).

Studies of the processes occurring at cluster shock-fronts are best done using systems where accurate observational constraints can be derived. The best observations require relatively strong shocks ( $\mathcal{M} \lesssim 3$ ), which are usually found in the peripheral regions of galaxy clusters where the electron density is very low ( $\lesssim 10^{-4} \text{ cm}^{-3}$ ). However, in these regions the low gas density can make it challenging to observe temperature and surface brightness discontinuities with the current generation of X-ray telescopes (Markevitch & Vikhlinin 2007; Botteon et al. 2018). Additionally, to best study the shocks it is preferable to minimize the mixing of different populations of electrons along the line of sight, large spherical shocks are preferred, since for them the de-projection is more accurate. As merger induced shocks in clusters are rare (because the systems must be caught within a limited stage of the overall merging event) there are only a handful of known strong shocks ( $\mathcal{M}_X \sim 2 - 3$ ) that meet these conditions, namely those in Abell 520 (Markevitch et al. 2005), Abell 2146 Russell et al. (2011, 2012), Abell 665 (Dasadia et al. 2016), Abell 115 (e.g. Botteon et al. 2016a), and El Gordo (Botteon et al. 2016b).

## 4.2 The galaxy cluster Abell 520

The Train Wreck Cluster Abell 520 (hereafter A520;  $z = 0.201$ ) is a highly-disturbed merging galaxy cluster with a merger axis  $\sim 60^\circ$  to the plane of the sky (e.g. Proust et al. 2000; Mahdavi et al. 2007; Girardi et al. 2008; Markevitch et al. 2005; Govoni et al. 2001b; Jee et al. 2012; Vacca et al. 2014). The total mass for A520 is estimated to be  $M = 7.8 \times 10^{14} M_\odot$  in Planck Collaboration et al. (2016). Previous studies at radio wavelengths have revealed  $\sim \text{Mpc}$ -scale, faint ( $\sim \mu\text{Jy arcsec}^{-2}$  at 1.4 GHz) emission associated with the ICM, which was classified as a radio halo (e.g. Giovannini et al. 1999; Govoni et al. 2001b; Vacca et al. 2014). With observations at a resolution of 39 arcsec the spectral energy distribution was found to be patchy with a mean value of  $-1.25^1$  and a dispersion of 0.22 (Vacca et al. 2014). In the SW region, the level of radio emission rapidly drops at the location of a prominent  $\mathcal{M}_X = 2.1_{-0.3}^{+0.4}$  bow shock, where the shock strength was derived from surface brightness and temperature jumps from Chandra

---

<sup>1</sup>The convention  $S \propto \nu^\alpha$  is used in this paper.

X-ray data (Markevitch et al. 2005; Wang et al. 2016, 2018). In addition there may be another shock toward the NE of the cluster (Wang et al. 2016) but the radio emission in this region has not been carefully examined. Edges to radio haloes, such as that in the SW of A520, at the locations of shocks have been observed in several other clusters (Markevitch 2010; Brown & Rudnick 2011; Macario et al. 2011; Shimwell et al. 2016; van Weeren et al. 2016c). However, a few of these situations, including in Abell 520, are puzzling since the expected properties for a radio relic (such as spectral transversal steepening gradients) are not detected (Vacca et al. 2014).

In this paper, our main aim is to examine the low-frequency emission from the cluster and to use these measurements to better constrain the spectral energy distribution of the diffuse synchrotron emission. This allows us to search for a spectral index structure associated with the shock in the SW. In addition we can also examine the structure of the radio emission in the NE at the location of the possible shock front identified by Wang et al. (2016). To achieve this aim, we observed the cluster with the Low Frequency Array (LOFAR; Haarlem et al. 2013) using High Band Antennas (HBA, 120 – 187 MHz) and combined these data with existing Giant Metrewave Radio Telescope (GMRT) 306 – 339 MHz and Very Large Array (VLA) 1 – 2 GHz data. We also make use of archival Chandra X-ray data.

In this study, we assume  $H_0 = 70 \text{ km s}^{-1} \text{ Mpc}^{-1}$ ,  $\Omega_M = 0.3$  and  $\Omega_\Lambda = 0.7$ . In this cosmology, an angular distance of 1 arcmin corresponds to a physical scale of 198.78 kpc at the cluster redshift of  $z = 0.201$ .

## 4.3 Observations and data reduction

### 4.3.1 LOFAR 145 MHz

The LOFAR 145 MHz observations of A520 were performed for a total of 7.3 hours divided equally between April 17 and 25, 2017 (project: LC7\_025). The calibrator 3C 147 was observed for 10 minutes. A summary of the observations is given in Table 4.1.

The calibration of the LOFAR data was done using the facet calibration scheme to correct for the direction-independent and direction-dependent effects which are implemented in the PreFactor<sup>2</sup> and Factor<sup>3</sup> pipelines. The data reduction procedure is described in detail in van Weeren et al. (2016a),

---

<sup>2</sup><https://github.com/lofar-astron/prefactor>

<sup>3</sup><https://github.com/lofar-astron/factor>

Table 4.1: Radio observations of A520

Telescope	LOFAR 145 MHz	GMRT 323 MHz	VLA 1.5 GHz
Project	LC7_25	27_070	AF349, AC706, AC776
Observation IDs	L584441, L589773	7394, 8007	—
Configuration	—	—	C, D
Calibrator	3C 147	3C 147	3C 48, 3C 147, 3C 138, 3C 286
Observation dates	Apr. 17 and 25, 2017	Oct. 31, 2014; Aug. 21, 2015	1998 Dec. 8; 1999 Mar. 19 2004 Aug. 30; 2005 Aug 30
Total on-source time (hr)	7.3	17.2	15.1
Correlations	full Stokes	RR, LL	full Stokes
Bandwidth (MHz)	48	33	150
Channel width (MHz)	0.0122	0.1302	50
Time resolution (s)	1	16	10
Number of (used) stations	62	28	24–27

Williams et al. (2016), and de Gasperin et al. (2018). In particular, the data were flagged for radio interference frequency (RFI) with Aoflagger (Offringa et al. 2012), were removed the contamination of the bright sources in the distant side lobes (i.e. Cassiopeia A, Taurus A), and were corrected for the initial phase offsets between the XX and YY polarizations. The clock offsets of different stations were also removed. The flux scale of the target data was calibrated according to the Scaife & Heald (2012) flux scale using the primary calibrator 3C 147. In Factor, the data were corrected for direction-dependent distortions that are mainly caused by ionospheric effects and errors in the beam model. After this pipeline processing, the final calibrated data from the different observations were combined for imaging (see details in Sec. 4.3.4).

#### 4.3.2 GMRT 323 MHz

A520 was observed with the GMRT 323 MHz on October 31, 2014 and August 21, 2015 for a total of 17.2 hours (project: 27\_070; PI: A. Shweta and R. Athreya). The calibrator 3C 147 was observed before and after the target. The observation details are summarized in Table 4.1.

The calibration of the GMRT data was done in SPAM (Source Peeling and Atmospheric Modelling; Intema et al. 2009). In this procedure the absolute flux scale was calibrated using 3C 147 and a source model consistent with the Scaife & Heald (2012) flux density scale. The data were flagged for RFI, and the gain and bandpass were calibrated. The direction-dependent calibration was performed with multiple self-calibration loops to correct for the ionospheric phase delay toward the direction of the target. The final calibrated data were used to make continuum images of A520 (see Sec. 4.3.4 for details).

#### 4.3.3 VLA 1.5 GHz

We combine multiple archival L-band data sets centered on A520. These data were observed in C- and D-configurations. The data are originally presented in Govoni et al. (2001b) (project: AF349) and Vacca et al. (2014) (project: AC776 and AC706). Details of the observations are summarized in Table 4.1.

The VLA data are separately calibrated in CASA using the flux calibrator 3C 48 for project AF349, 3C 147 for project AC776, 3C 147, 3C 138, and 3C 286 for project AC706. The phase calibrator is 0459+024 for project AF349 and 0503 + 020 for projects AC706 and AC776. The amplitude is

calibrated according to the Perley & Butler (2013) flux scale which has an uncertainty of a few percent for these calibrators. After the initial calibration, the data are self-calibrated with phase-only calibration steps before phase-amplitude calibration steps. The calibrated data from all observations are combined in the (u,v)-plane and used to make continuum images of A520 (see Sec. 4.3.4).

#### 4.3.4 Continuum imaging and spectrum mapping

To map the diffuse emission from A520, the LOFAR, GMRT and VLA calibrated data sets were deconvolved with the MS-MFS (multi-scale and multi-frequency synthesis) CLEAN algorithm in CASA (McMullin et al. 2007; Cornwell 2008; Rau & Cornwell 2011). The MS-MFS option was used to properly model frequency-dependent emission and more accurately deconvolve extended objects. A wide-field algorithm (W-projection, Cornwell et al. 2005, 2008) was also used to account for the baseline non-coplanarity over the sky. The diffuse emission at different spatial scales was enhanced using Briggs (1995) weighting schemes with multiple robust values (see Table 4.2). The primary beam correction for LOFAR was done by dividing the image by the square root of the .avgpb map generated by AWimager (Tasse et al. 2012). Whereas, the GMRT images were divided by a primary beam approximated by <sup>4</sup>,

$$A(x) = 1 - \frac{3.397}{10^3}x^2 + \frac{47.192}{10^7}x^4 - \frac{30.931}{10^{10}}x^6 + \frac{7.803}{10^{13}}x^8, \quad (4.1)$$

where  $x = f \times \theta$  with  $f = 0.323$  GHz and angular distance  $\theta$  from the pointing center in arcmin. The VLA images were primary beam corrected using the built-in pbcor option of CASA's CLEAN task.

Spectral index maps of A520 were made with the LOFAR, GMRT and VLA Stokes I images that were made using similar imaging parameters (i.e. uv-range, MS-MFS, W-projection options, Briggs' robust weighting; see Table 4.2). Additionally, we used an outertaper to adjust the weightings of long baselines to obtain a spatial resolution of  $\sim 20$  arcsec for each of the maps. The LOFAR, GMRT and LOFAR Stokes I images were then smoothed with 2D Gaussians to a common resolution of exactly 20 arcsec. They were also corrected for any astrometric misalignments between the images. To do this, we fit 2D Gaussian to compact sources in the images. The central positions of the Gaussians are considered as approximate locations of the sources. The misalignments between the images is taken to be

---

<sup>4</sup>GMRT User's manual

Table 4.2: Image properties

Telescope	uv-range ( $k\lambda$ )	robust <sup>a</sup>	outertaper (arcsec)	resolution (arcsec <sup>2</sup> , p.a.)	$\sigma$ ( $\mu\text{Jy beam}^{-1}$ )	Fig.
LOFAR	$\geq 0.100$	0.0	15	$31.3 \times 20.4$ (47.7°)	460	4.1
	0.114 – 16.220	0.0	5	$20 \times 20^b$	450	4.3 <sup>c</sup>
GMRT	$\geq 0.100$	0.0	15	$18.3 \times 15.5$ (60.8°)	100	4.1
	0.114 – 16.220	0.0	16	$20 \times 20^b$	130	4.3 <sup>c</sup>
VLA	0.114 – 16.220	0.0	5	$19.5 \times 18.7$ (–43.1°)	26	4.1, 4.3 <sup>c</sup>

Notes: <sup>a</sup>: Briggs weighting of uv data; <sup>b</sup>: smoothed; <sup>c</sup>: spectral index map



the mean of the offsets between the locations of the compact sources. The images were then regridded to identical pixel size. To calculate the spectral index map, only the  $\geq 3\sigma$  pixels that were detected in at least 2 images were used. These were fit with a power-law function of the form  $S \propto \nu^\alpha$ . The spectral index errors were calculated taking into account the image noise and a flux scale uncertainty of 15% for LOFAR, 10% for GMRT and 5% for VLA.

We note that to ideally recover the same spatial scales at each frequency the uv-coverage of each data set should be matched. Generally, this matching is approximated by imaging the data sets with a uniform weighting scheme and with a common uv-coverage in each data set, but this can result in a significantly increased noise level. Therefore, to maintain a sufficient S/N detection of A520 we have instead imaged the data with equal uv-range and a combination of robust parameter and taper to ensure that the images produced are of approximately equal resolution.

#### 4.3.5 *Chandra*

Archival Chandra data in the energy band of 0.5 – 2.0 keV were fully calibrated and are published as part of an X-ray sample study in Andrade-Santos et al. (2017) from which we acquire the calibrated data. The observation IDs of the archival data used are 528, 4215, 7703, 9424, 9425, 9426, and 9430, resulting in a total observing duration of 528 ks.

## 4.4 Results

In Figs. 4.1 and 4.2, we present the continuum images of A520 obtained with the LOFAR 145 MHz, GMRT 323 MHz, and VLA 1.5 GHz observations. The image properties are summarized in Table 4.2. The radio images show the detection of diffuse emission associated with the ICM as well as multiple radio galaxies. To study the spectral properties of the extended radio sources, we combine the LOFAR, GMRT and VLA data to make the spectral index map in Fig. 4.3.

### 4.4.1 The radio halo

Similarly to previous observations, the new LOFAR 145 MHz and GMRT 323 MHz images (Fig. 4.1 and 4.2) show the presence of a giant radio halo ( $760 \times 950 \text{ kpc}^2$ ) with an overall morphology that approximately traces the X-ray emission of A520 (e.g. Giovannini et al. 1999; Govoni et al. 2001b;

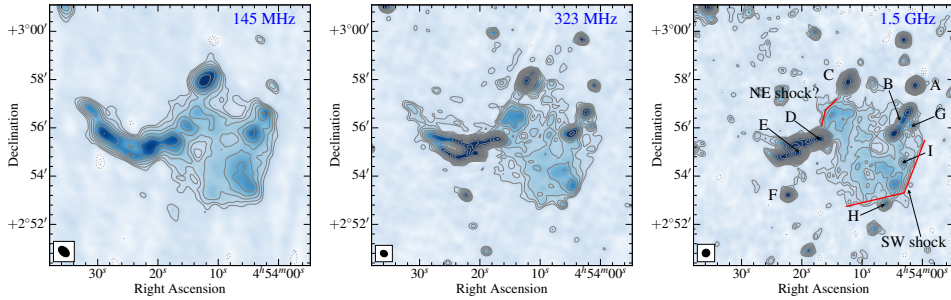


Figure 4.1: Radio continuum images of A520. The contours are from  $\pm 3\sigma$  and are spaced by  $\sqrt{2}$ . The image noise is  $\sigma = 460, 100, \text{ and } 26 \mu\text{Jy beam}^{-1}$  for the LOFAR, GMRT, and VLA images, respectively. The sources are labeled in the VLA image, partly adapting the notation in Vacca et al. (2014). The synthesized beams are shown in the bottom left corners.

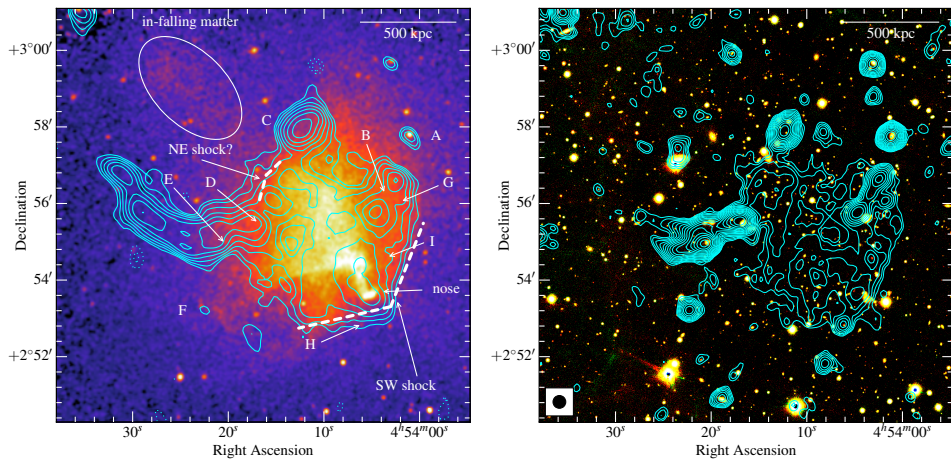


Figure 4.2: Chandra 0.5 – 2.0 keV (left) and PanSTARRS color (right) images of A520. The LOFAR (left) and GMRT (right) contours are identical to those in Fig. 4.1.

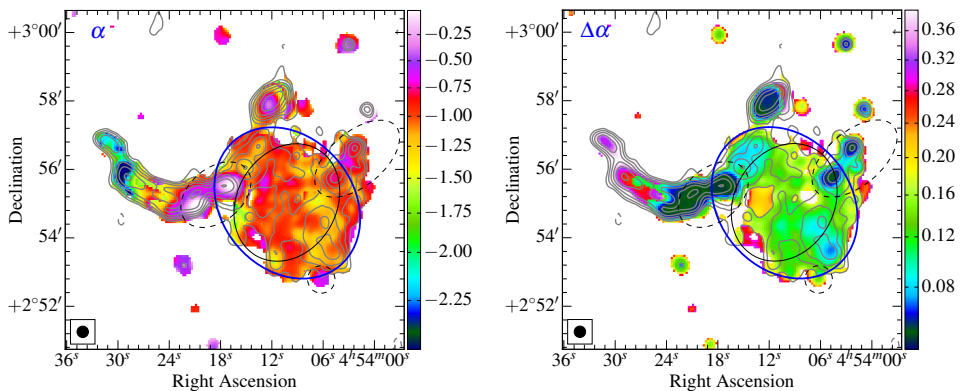


Figure 4.3: The 145 MHz–1.5 GHz spectral index (left) and error (right) maps of A520. In the both panels, the blue thick ellipse roughly follows the  $3\sigma$  contour of the halo emission. The black thin ellipse shows the inner region of the halo. The black dashed regions are masked. The LOFAR contours begin with  $3\sigma$ , where  $\sigma = 450 \mu\text{Jy beam}^{-1}$ , and are spaced with  $\sqrt{2}$ .

Vacca et al. 2014). We use the LOFAR, GMRT, and VLA 20 arcsec maps that are made with identical imaging parameters (i.e uv-range  $0.114 - 16.220 k\lambda$ , Briggs' robust weighting 0.0) to measure the integrated flux for the halo emission. The measurement is done within an elliptical region (i.e. the blue thick ellipse in Fig. 4.3) with regions contaminated by the emission from the radio galaxies B, D, E, H, G, and I masked out. The elliptical region was chosen to roughly follow the  $3\sigma$  contour of the LOFAR detected emission. Since the surface brightness (SB) of the halo is approximately uniform within the  $\lesssim 450$  kpc-radius central region (see Fig. 4.1, also Fig. 5 in Vacca et al. 2014), we assume that the SB in the masked regions can be extrapolated from the unmasked regions. The integrated flux of the halo is then calculated as the integrated flux measured in the unmasked region multiplied by a factor to account for the area of the masked regions (see Fig. 4.3). The total error quoted for the integrated flux measurements is the quadratic sum of the uncertainty in the flux scale and the image noise. The integrated fluxes of the halo at 145 MHz, 323 MHz and 1.5 GHz are  $229.7 \pm 34.8$  mJy,  $90.5 \pm 9.2$  mJy and  $18.8 \pm 1.0$  mJy, respectively. For comparison with the Wang et al. (2018) measurement, that uses the same VLA data, we repeat the calculation for the flux within a region encompassing the  $1\sigma$  contour. The halo flux within this region is  $20.6 \pm 1.1$  mJy and is consistent with the value of  $20.2 \pm 1.5$  mJy that was measured in a radio galaxy subtracted image presented in Wang et al. (2018). Another flux mea-

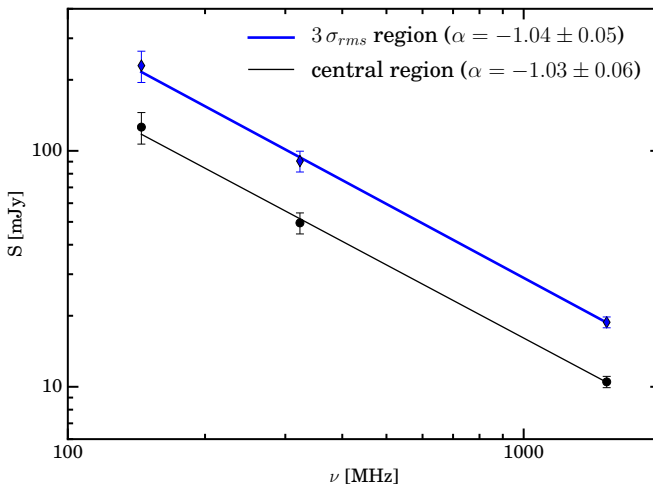


Figure 4.4: Integrated spectrum between 145 MHz and 1.5 GHz for the radio halo. The integrated fluxes are measured within the  $3\sigma$  contour (blue thick) and central (black thin) regions in Fig. 4.3.

surement for the extended emission at 1.4 GHz in Cassano et al. (2013) is  $19.4 \pm 1.4$  mJy which is in agreement with our estimate. Vacca et al. (2014) obtain a smaller value of  $16.7 \pm 0.6$  mJy for the halo flux, but they did not extrapolate their measurements to estimate the contribution from masked regions, which might explain the difference.

To estimate spectral index of the halo, we fit the integrated fluxes with a single-power-law function,  $S \propto \nu^\alpha$ , that describes the synchrotron emission mechanism. As plotted in Fig. 4.4, the integrated spectrum of the halo follows the power law relation with an index of  $\alpha_{145 \text{ MHz}}^{1.5 \text{ GHz}} = -1.04 \pm 0.05$ . Our measurement of the integrated spectral index is in line with the estimate of  $\alpha_{325 \text{ MHz}}^{1.4 \text{ GHz}} = -1.12 \pm 0.05$  in Vacca et al. (2014). In the central region of the halo, the integrated spectral index is estimated to be  $\alpha_{145 \text{ MHz}}^{1.5 \text{ GHz}} = -1.03 \pm 0.06$ . Examining the spatial distribution of the halo spectrum, we find that the spectral index over the inner region of the halo (i.e. black thin ellipse in Fig. 4.3) remains approximately constant around a mean of  $-1.01$  with a scatter of 0.12. A similar situation is found in the larger region (i.e.  $\bar{\alpha} = -1.03$  in the blue thick ellipse in Fig. 4.3). However, Fig. 4.3 also indicates that there are small changes of the spectral indices in the NE and SW region on scales larger than the beam size. These estimates on the spectral index, based on the distribution of the spectral indices, are also consistent with the integrated spectral index values above.

#### 4.4.2 The SW region of the radio halo

The radio continuum images in Fig. 4.1 show excess emission in the SW region of the radio halo, consistent with previous observations in, e.g., Giovannini et al. (1999), Govoni et al. (2001b), and Vacca et al. (2014). The SW radio emission roughly follows the "bullet"-like shock front detected with the X-ray observations (Markevitch et al. 2005). The radio emission increases sharply across the SW shock front from west to east. Assuming that the upper limit for the radio emission in the pre-shock region is  $1\sigma$  of the background noise, the increase in the radio surface brightness is  $\sim 4$ ,  $\sim 5$ , and  $\sim 8$  times at 145 MHz, 323 MHz, and 1.5 GHz, respectively. In Fig. 4.5, we plot the regions where the SB and spectral indices are extracted for examining the spatial distribution of the radio emission and spectral energy distribution. The profiles in Fig. 4.6 show that the radio emission in the region behind the SW shock continues to increase, most significantly at low frequencies, before gradually decreasing in the region  $\sim 230$  kpc away from the SW radio edge. The spectrum index in the SW radio edge is flattest at the  $3\sigma$  SW edge with  $-0.84 \pm 0.11$  and steepens to  $-1.13 \pm 0.07$  at  $\sim 165$  kpc towards the cluster center from the SW  $3\sigma$  contour. This spectral trend can also be seen in the spectral index map (Fig. 4.3). Our spectral index measurement between 145 MHz and 1.5 GHz at the SW radio edge is flatter than the previous estimate of  $\alpha_{323\text{ MHz}}^{1.4\text{ GHz}} = -1.25$  which was derived from lower (39 arcsec) resolution data in Vacca et al. (2014).

#### 4.4.3 The NE region of the radio halo

Towards the NE direction, the radio emission of the halo gradually increases before sharply decreasing at the NE edge (Fig. 4.1). An enhancement in the extended radio emission (i.e. projected size of  $\sim 65$  kpc in radius) is detected at  $\sim 3\sigma$  at 1.5 GHz but is slightly less visible at the lower frequencies of 145 MHz and 323 MHz. At the NE edge there is a hint that the spectral index seems to steepen in the NE-SW direction, but the steepening trend of the spectral index is still uncertain due to the large errors in the spectral measurement (see the spectral index profile in Fig. 4.6, bottom panel).

A number of merging clusters generate double shocks that propagate on diametrically opposite sides of the cluster center (e.g. Russell et al. 2011; Dasadia et al. 2016; Urdampilleta et al. 2018). In A520, a shock ( $\mathcal{M}_X = 2.1$ ; Markevitch et al. 2005) is detected in the SW region of the cluster and Wang et al. (2016) discussed a possibility of a counter shock in the NE side of the cluster. To further search for a possible counter shock, we fit the

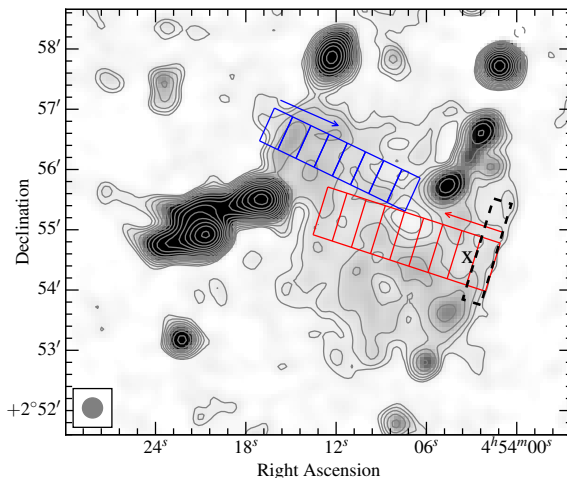


Figure 4.5: The rectangle regions in the SW and NE directions where SB and spectral indices are plotted in Fig. 4.6. The black dashed rectangle is where the spectral index right behind the SW shock is estimated. The X cross indicates the location of a compact source I that is subtracted from the VLA data. The VLA contours are identical to those in Fig. 4.1 (right).

X-ray SB emission with a broken power-law function<sup>5</sup>, assuming that the X-ray emission is spherically symmetric about a point at the cluster center. The fitted function is consistent with underlying broken power-law particle density profile,

$$n(r) = \begin{cases} C n_0 \left(\frac{r}{r_{\text{break}}}\right)^{-a_d} & \text{if } r \leq r_{\text{break}} \\ n_0 \left(\frac{r}{r_{\text{break}}}\right)^{-a_u} & \text{if } r > r_{\text{break}} \end{cases} \quad (4.2)$$

where  $C = n_d/n_u$  is the shock compression factor or particle density jump (the subscripts  $d$  and  $u$  stand for downstream and upstream regions, respectively);  $r_{\text{break}}$  is the location of the SB discontinuity;  $a$  is the slope of the power-law function;  $n_0$  is normalization factor or particle density at the  $r_{\text{break}}$  location of the upstream region. We find the best-fit parameters for the selected sector (see Fig. 4.7) that has a compression factor of  $C = 1.74 \pm 0.03$ , coincidentally close to the outer edges of the radio emission. The SB jump is located  $428.6_{-0.8}^{+1.1}$  kpc from the sector center (i.e.  $4^{\text{h}}54^{\text{m}}07.96^{\text{s}}$ ,  $+2^{\text{d}}55^{\text{m}}29.64^{\text{s}}$ ). The best-fit indices are  $a_d = 0.23 \pm 0.02$  and  $a_u = 1.56 \pm 0.02$ . The normalization factor is  $n_0 = (20.1 \pm 0.4) \times 10^{-3} \text{ cm}^{-3}$ .

<sup>5</sup>using PyXel, available on <https://github.com/gogrean/PyXel>

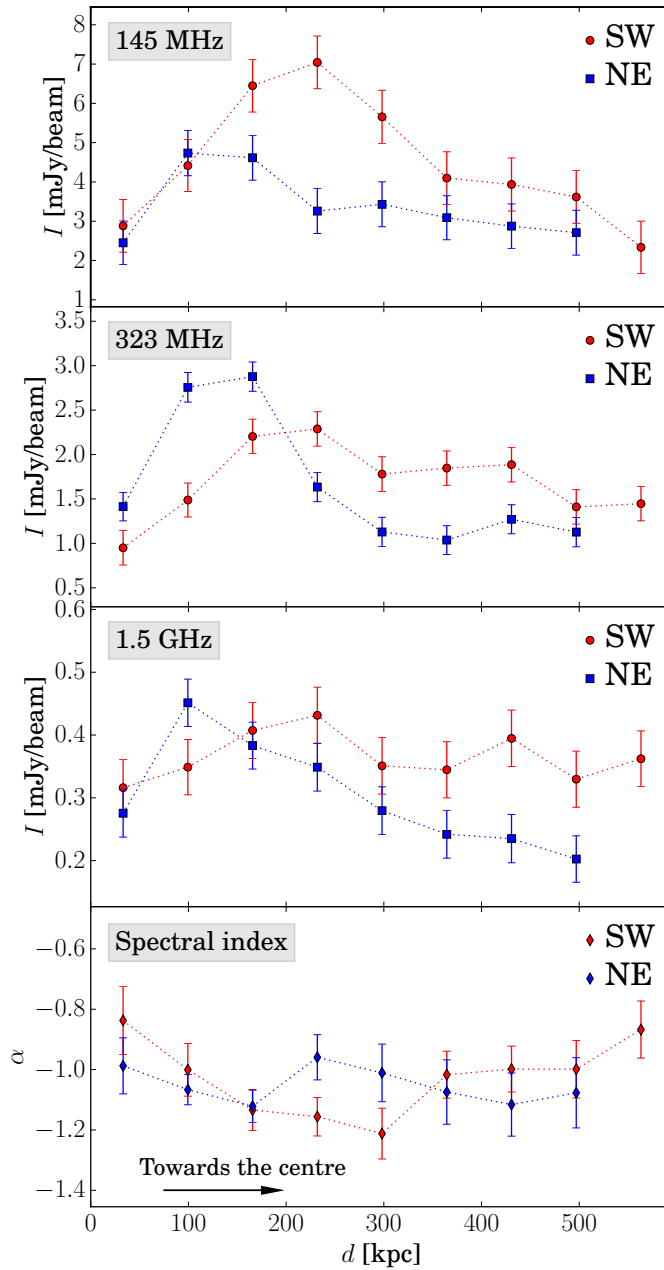


Figure 4.6: The SB (top panels) and spectral index (bottom panel) profiles from outer edges toward cluster center for the regions in the SW and NE directions in Fig. 4.5. Toward the cluster center, the spectral index is steepened for the SW radio emission and remains approximately constant for the NE radio emission.

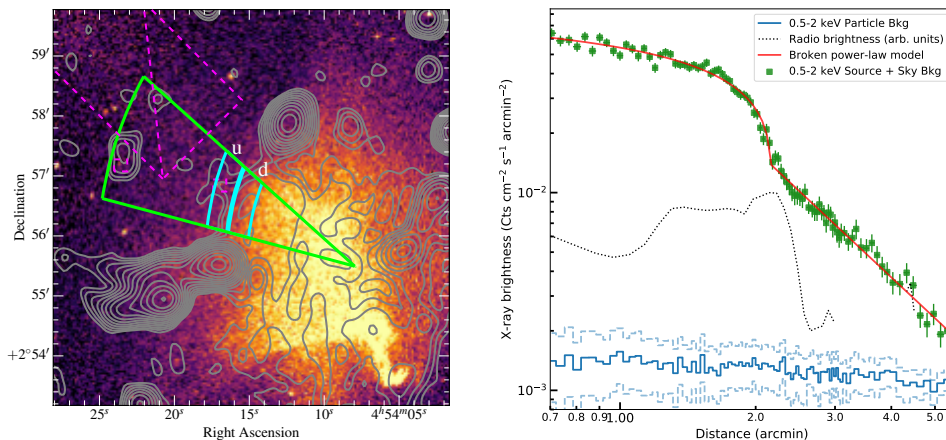


Figure 4.7: Left: the sector where SB are extracted from the Chandra X-ray data. The magenta dashed regions are masked to remove the point sources and the emission from the NE plasma that is falling into the cluster. The blue regions are where temperature is calculated for upstream and downstream ICM regions. Right: SB profile toward the NE region and the best-fit radial SB profile (red).

The particle density jump suggests the presence of either a cold front or shock front at the  $r_{\text{break}}$  location.

If the detected discontinuity in the X-ray SB is due to a cold front, the ICM thermal pressure must be balanced in the upstream and downstream regions (or  $T_u/T_d = C$ ). To check this possibility, we estimate temperature on both sides of the density jump location from the Chandra data. The selected upstream and downstream regions are shown in Fig. 4.7. We obtain temperature of  $T_u = 8.57^{+1.48}_{-1.16}$  keV for the pre-shock region and a slightly higher temperature in the post-shock region  $T_d = 9.49^{+0.90}_{-0.88}$  keV, but still within the  $1\sigma$  significance. Wang et al. (2016) estimated a slight decrease in the temperature in the post-shock region (i.e.  $\sim 9$  keV), but the decrease is still within their  $1\sigma$  uncertainty and they use larger regions (i.e. C3 and C4 in their Fig. 4) than the regions we used here in Fig. 4.7. It is also noted that the temperature estimate in the NE region might be contaminated by other sources such as the in-falling hot matter (see Fig. 4.2) or the nearby X-ray emission in the regions of sources C, D, and E (Wang et al. 2016). The temperature value we estimate here implies that if the SB jump is due to a cold front then  $C = 0.90 \pm 0.16$ . This is inconsistent with the SB jump of  $C = 1.74 \pm 0.03$  from the broken power-law fitting of the X-ray emission. Therefore, the assumption that the SB jump is because of the presence of a cold front might be unlikely.



In the case that the discontinuity is caused by a merger shock front, the compression of the ICM plasma is directly related to the shock Mach number by the Rankine-Hugoniot jump relation,

$$\mathcal{M}_X = \sqrt{\frac{2C}{\gamma + 1 - C(\gamma - 1)}}, \quad (4.3)$$

where  $\gamma = 5/3$  is the adiabatic index of the ICM plasma. Given the compression factor of  $C = 1.74 \pm 0.03$ , we have  $\mathcal{M}_{\text{NE}}^X = 1.52 \pm 0.02$  which is smaller than the SW shock Mach number ( $\mathcal{M}_{\text{SW}}^X = 2.4_{-0.2}^{+0.4}$ ; Wang et al. 2018), but is still in the range of values that are typically estimated for cluster merger shocks (i.e.  $\mathcal{M}_X \lesssim 3$ ) in the literature (e.g. Russell et al. 2010; Macario et al. 2011; Akamatsu et al. 2015; Botteon et al. 2016a,b; Dasadia et al. 2016). The shock Mach number can also be related to the temperature jump at the shock,

$$\mathcal{M}_X = \sqrt{\frac{[(8T_{du} - 7) + [(8T_{du} - 7)^2 + 15]^{1/2}]}{5}}, \quad (4.4)$$

where  $T_{du} = \frac{T_d}{T_u}$  (e.g. Landau & Lifshitz 1959; Markevitch & Vikhlinin 2007; Finoguenov et al. 2010; van Weeren et al. 2016c). The Mach number derived from the temperature is  $\mathcal{M}_{\text{NE}}^X = 1.1_{-0.2}^{+0.3}$  which is slightly smaller than the value we estimate from the SB jump above. As mentioned, the precise temperature value might be biased by the contaminating sources in the NE region which are not be easily removed (e.g. Wang et al. 2016).

## 4.5 Discussion

### 4.5.1 The radio halo

Despite the accurate characterization of the radio emission in A520, it remains uncertain whether or not the emission can all be attributed to a halo or if there is additional radio relic emission (e.g. Govoni et al. 2001b; Vacca et al. 2014). The radio halo coincides with the region swept by the SW shock and by the (possible) NE shock. Shocks are detected coincidence with the edges of a number of radio haloes (e.g. Markevitch et al. 2005; Markevitch 2010; Macario et al. 2011; Shimwell et al. 2014) suggesting that they might drive a turbulent region bounded by tangential magnetic fields where particles are confined and re-accelerated.

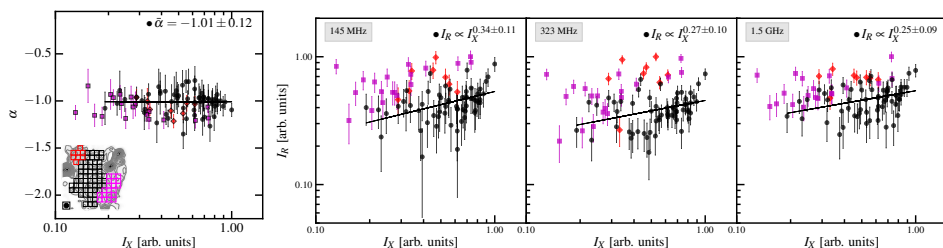


Figure 4.8: The scatter plots of spectral index and radio SB ( $I_R$ ) as a function of X-ray SB ( $I_X$ ). The regions for extracting data are shown in the overlaid image (left). The data points are plotted in the same color as the regions in the overlaid image (i.e. black circles for the central regions, magenta squares for the regions in the SW direction, and red diamonds for the regions in the NE direction). The best-fit parameters are obtained for the central regions.

Although the overall shape of the halo follows the X-ray emission, the radio brightness of the halo is very flat, especially at 1.5 GHz (Fig. 4.1). A correlation between radio and X-rays is observed only in the region of the trail/bullet-like structure in the southern region where the radio and X-ray emission appears brighter (Fig. 4.2). However, in general the radio brightness does not follow the X-ray emission. This is clear in Fig. 4.8 where we show the point-to-point radio to X-ray brightness using cells of the beam size (i.e. 20 arcsec or 66 kpc). Basically only a tentative trend in the form of  $I_R \propto I_X^b$ , where  $b = 0.34 \pm 0.11$ ,  $0.27 \pm 0.10$ , and  $0.25 \pm 0.09$  at 145 MHz, 323 MHz, and 1.5 GHz, respectively, is observed in the central region of the halo. This is similar to a case reported by Shimwell et al. (2014) who finds no significant correlation between radio halo and X-ray brightness in the bullet cluster 1E 0657–55.8. However, the relation between the radio and X-ray brightness in A520 is different from a number of cases of regular and roundish radio haloes reported in the literature where a clear correlation, typically slightly sublinear, is found between the radio and X-ray brightness (e.g.  $b \approx 0.64 - 0.99$ ; Govoni et al. 2001a,b; Ferretti et al. 2001; Venturi et al. 2013; Rajpurohit et al. 2018). This suggests that the haloes in A520 and the bullet cluster may be in similar evolution states, but their states may be different from those of the haloes in the clusters that follow the scaling relation.

All models that have been proposed for the formation of radio haloes predict a connection between radio and X-ray emission (e.g. see Brunetti & Jones 2014 for review). This is straightforward in hadronic models (including the models where secondary particles are re-accelerated by turbulence)

because the ICM that produces the X-ray radiation also provides the targets for the inelastic collisions that generate the radio emitting secondary electrons. Also in the case where primary seed electrons are re-accelerated by turbulence the energy reservoir to re-accelerate particles is extracted from the turbulent and kinetic energy of the thermal ICM. This should induce some connection between thermal and non-thermal quantities. One possibility to explain the properties of the extended radio emission in A520 is that the radio and X-ray emission are not co-spatial and that the majority of the radio emission is produced in a thick perturbed cocoon that bounds the volume. The halo is swept by the outgoing shocks and embeds the very central dense substructures that appear bright in the X-ray band. This situation may explain the connection between the edges of the halo and the shocks and - in fact - it is not surprising given the very particular evolutionary stage of A520. According to Wang et al. (2016), the very peculiar twisted structure that dominates the X-ray emission in A520 traces the gas from a disrupted cool core that is swept away from the central galaxy of its former host sub-cluster by ram pressure in the downstream region of the SW shock. This gas is observed to form a physically connected trail of dense and cold clumps resembling a leg with a bright foot, a knee and a leg along the ridge extending about 300 kpc east from the knee (Wang et al. 2018). The twisted structure suggests that motions in the shocked gas surrounding the trail are turbulent, however the cool gas within the trail itself is probably not turbulent because at this early stage ram pressure stripping prevents the development of instabilities at its boundaries and the mixing of the trail with the hot surrounding medium (Takizawa 2005).

Another important clue to the origin of the radio halo is provided by the spectral index distribution in A520. As already mentioned in Sec. 4.4.1, the spectral index in the radio halo is fairly constant  $\alpha \approx -1.03$  with a scatter of  $\sim 0.12$  on beam scales (i.e. 20 arcsec or 66 kpc). We perform simulations to examine whether the scatter is due to statistical errors (i.e. from the image noise) or it is the intrinsic spectral features of the halo. First, we assume that the radio halo has a constant spectral index (i.e.  $\alpha = -1.03$ , meaning no intrinsic scatter). Using the observed VLA 1.5 GHz map, we generate the halo flux distribution at 145 MHz and 323 MHz. Gaussian noise is then added to the maps at levels that are estimated from the observed LOFAR, GMRT and VLA maps (see Table 4.2). The spectral index maps derived from the simulated radio maps are used to calculate the anticipated scatter in spectral index. The cells we used here have the size of the beam (i.e. 20 arcsec, see Fig. 4.8). We find that the observed spectral index scatter of

0.12 on the scales of the beam size is consistent with the scatter recovered from the simulated spectral index maps (i.e.  $\Delta\alpha_{\text{sim.}} = 0.13 \pm 0.02$ ) where the statistical errors are from the image noise alone. On larger scales, there are hints of possible spectral variations, for example the southern region of the halo (the nose and bullet-like/trail; the magenta squares in Fig. 4.8) shows a spectral index that is steeper than the SW region of the halo (Fig. 4.3), still spectral variations are fairly small, in the range 0.1 – 0.2, if we exclude the regions in the SW direction (i.e. magenta squares). A more detailed constraint on spectral variations in the halo using, e.g., simulations and theoretical analysis is beyond the aim of this paper. However, the projected distribution of spectral indices in the halo can be used to infer basic constraints. For example, using a conservative limit  $\Delta\alpha_{\text{proj.}} < 0.12$  on spatial scales of the beam (i.e. 20 arcsec) and assuming that the spectral index in the halo volume can change stochastically around a mean value, the intrinsic scatter is roughly  $\Delta\alpha_{\text{intr.}} \approx \sqrt{N} \times \Delta\alpha_{\text{proj.}}$ , where  $N \approx 10$  is the number of beam cells intercepted along the line of sight, implying  $\Delta\alpha_{\text{intr.}} < 0.38$ . Such a small-moderate scatter of the spectrum in the halo volume is also consistent with the hypothesis that the majority of the radio emission is generated in a smooth extended cocoon rather than from the central regions where strong X-ray gradients and the disrupted cool core are observed.

#### 4.5.2 The SW radio edge

Markevitch et al. (2005) and Wang et al. (2018) discussed whether the radio emission close to the prominent SW shock could be induced by adiabatic compression or Fermi-I processes. The Fermi-I processes generate synchrotron emitting relativistic electrons by accelerating electrons either directly from the thermal pool or re-accelerating mildly relativistic electrons from a seed population of pre-existing fossil plasma. In this section we reassess these possibilities making use of our new measurements.

#### Shock acceleration

In the DSA model, relativistic electrons with the Lorentz factor  $\gamma \gg 10^3$ , that emit radio synchrotron emission in  $\sim \mu\text{G}$  magnetic fields, are (re-)accelerated by a shock. The sources of the relativistic electrons could be either the thermal electrons or a pre-existing population of fossil electrons in the ICM. Unless the fossil electrons have flat spectrum, the spectral index ( $\alpha_{\text{inj}}$ ) of the injected CR electrons is related to the shock Mach number  $\mathcal{M}$  (e.g.

Blandford & Eichler 1987),

$$\alpha_{\text{inj}} = \frac{1}{2} - \frac{\mathcal{M}^2 + 1}{\mathcal{M}^2 - 1}. \quad (4.5)$$

The relativistic electrons injected by the shock have an energy spectrum distribution of  $\frac{dN}{dE} \propto E^{-\delta_{\text{inj}}}$ , where  $\delta_{\text{inj}} = 1 - 2\alpha_{\text{inj}}$ . In cases where the electron cooling time is much quicker than the lifetime of the shock, the integrated spectral index of the radio emission in the region behind the shock is steeper than the injection index by 0.5 (i.e.  $\alpha_{\text{int}} = \alpha_{\text{inj}} - 0.5$ ; Ginzburg & Syrovatskii 1969).

The electron cooling due to the synchrotron and IC energy losses is one of the key observational links between large-scale shocks and extended radio emission in merging galaxy clusters. Observationally, the cooling results in a characteristic steepening of the spectral index of the radio emission with distance from the shock front (e.g. van Weeren et al. 2010). Despite the SW region of A520 hosting a strong shock, previously radio observations have not detected the spectral steepening in the region behind the shock (Vacca et al. 2014). The lack of detection may be due to the sensitivity and resolution limitations.

In Sec. 4.4.2, we use the 20 arcsec-resolution images to show that the spectral index for the radio emission steepens in the region behind the SW shock front. The spectral index immediately behind the shock front is  $\alpha_{145 \text{ MHz}}^{1.5 \text{ GHz}} = -0.85 \pm 0.06$ . For a proper comparison with the X-ray study in Wang et al. (2018), we measure here the index in the post-shock region where the shock Mach number is highest (i.e. region N1+N2 in Wang et al. 2018; also see the black dashed rectangle in Fig. 4.5). According to the DSA model, if the relativistic electrons in the SW edge are (re-)accelerated from the thermal pool or steep-spectrum fossil electrons with the injection index of  $-0.85 \pm 0.06$ , the shock should have a Mach number of  $\mathcal{M}_{\text{SW}} = 2.6_{-0.2}^{+0.3}$ . Our estimate of the shock Mach number is in line with the measurements from X-ray data (e.g.  $\mathcal{M}_{\text{SW}}^{\text{X}} = 2.4_{-0.2}^{+0.4}$  in Wang et al. 2018). The agreement between the radio and X-ray derived Mach numbers for the SW shock implies that, in this case, the spectral properties of the radio emission at the SW edge are consistent with the DSA picture that the radio emitting relativistic electrons are either accelerated from the thermal pool or re-accelerated from a pre-existing population of fossil plasma.

In the shock-related (re-)acceleration scenario, radio emission is brightest at the shock front and becomes fainter in the downstream region where steeper spectrum emission should be detected (e.g. van Weeren et al. 2010; Rajpurohit et al. 2018). However, the brightest emission in the SW region

of A520 is found at far distance (i.e.  $\sim 220$  kpc) from the SW shock front and is located at the region of the steepest spectrum emission (Fig. 4.6), which seems to be inconsistent with the shock-related (re-)acceleration. A possibility for this mismatching is that the downstream shock-related emission is mixed with the emission from the halo due to the smoothing and/or projection effects. Otherwise, the agreement between the radio and X-ray derived Mach numbers might be a random coincidence. To separate the two scenarios, polarization observations will be required.

### Shock compression

Another possible mechanism for the radio emission at the SW edge is the gas compression of fossil electrons by the merger shock as being discussed in Markevitch et al. (2005). Since magnetic fields are embedded in the ICM plasma, the adiabatic compression by the shock amplifies the magnetic field strength and increases the energy density of pre-existing relativistic electrons. A requirement for this scenario to happen is that both fossil electrons and magnetic fields must be present and produce synchrotron emission before the shock passage. Given a population of fossil electrons of a power-law energy spectrum,  $dN/d\gamma = N_0\gamma^{-\delta}$ , the synchrotron emissivity per unit volume immediately behind the shock front is proportional to the shock compression factor  $C$ ,

$$I_\nu \propto C^{(2/3)\delta+1}. \quad (4.6)$$

Under the hypothesis of power-law distribution of the emitting electrons, the predicted relation, Eq. 4.6, between the radio emission in the pre- and post-shock regions by the compression model provides means for observationally testing of the model. A recent study by Wang et al. (2018) investigated this scenario using the VLA 1.4 GHz data, but no extended emission is detected in the pre-shock region. By modeling the radio emission in the shock regions, Wang et al. (2018) find that an emissivity jump of a factor of 10 (or 16) is inconsistent with the VLA data at  $3\sigma$  (or  $2\sigma$ ) significance. Given the estimated parameters for the shock (i.e.  $\alpha = -1.25$ ,  $C_{\text{nose}} = 2.7$ ), Wang et al. (2018) found a predicted emissivity jump of 16, meaning that the compression model is rejected at  $2\sigma$  significance. However, if the CRs lose most of their energy within 130 kpc, the spectral index immediately behind the shock was approximated as  $\alpha = -1.25 + 0.50 = -0.75$ . In this case, the compression model predicts a jump of 9, which increases the statistical significance of rejecting the compression model to  $3\sigma$  (Wang

et al. 2018). It is noted that the spectral index value used in Wang et al. (2018) is estimated from a low-resolution (39 arcsec or 130 kpc) spectral index map in Vacca et al. (2014). This may bias the spectral measurement as high-resolution maps are required to resolve the distribution of the source spectrum.

Our 20 arcsec-resolution spectral index map in Fig. 4.3 quantifies the steepening of the spectral index behind the SW shock front (also see the spectral index profile in Fig. 4.6, bottom). The spectral index between 145 MHz and 1.5 GHz in a 20 arcsec-wide region behind the SW edge (i.e. the N1+N2 sector in Wang et al. 2018; see Fig. 4.5) is  $\alpha = -0.85 \pm 0.06$ . With this higher-resolution measurement of the spectral index, we estimate that the emissivity in the pre-shock region should be  $10 \pm 3$  times lower than that in the region immediately behind the shock front, according to the adiabatic compression model (Eq. 4.6). This prediction can be ruled out at the  $2 - 3\sigma$  confidence levels, based on our new spectral index measurement and the modeling of the radio emission in the shock region in Wang et al. (2018). In the calculation, we have used a power-law spectrum slope of  $\delta = 1 - 2\alpha = 2.64$  and a shock compression factor of  $C(\theta) = C_{\text{nose}} \sqrt{\cos(\theta)}$  which is the correction for the azimuthal dependence in the measurement of the gas density jump (here  $\theta$  is the angle from the shock nose; Wang et al. 2018). We have used  $C_{\text{nose}} = 2.7 \pm 0.3$  which is the maximum density jump at the location of the shock nose (i.e. region N1 in Wang et al. 2018). The true spectral index at the SW shock front might be even flatter if the relativistic electrons radiate a significant amount of their energies within the 20 arcsec resolution region we use here. This would further lower the predicted emissivity jump and increase the significance at which this scenario could be ruled out.

The generation of the relativistic electrons at the SW shock is therefore unlikely to be solely caused by the adiabatic compression of the fossil electrons. However, this does not exclude the scenario where the adiabatic compression and re-acceleration of fossil electrons by the shock simultaneously occur since the predicted emissivity jump, depending on the spectrum of the pre-existing relativistic electrons, might be considerably higher in this case (Markevitch et al. 2005) and could still be consistent with the constraints obtained by Wang et al. (2018) using the VLA data set.

### 4.5.3 The NE radio edge

The origin of the excess radio emission in the NE region remains unclear. The detection of the SB X-ray jump coincident with at the location of the

NE radio edge in Fig. 4.7 might imply a possible connection between the thermal and non-thermal processes in the ICM. In Sec. 4.4.3, we find that the discontinuity in the X-ray SB corresponds to a shock Mach number of  $\mathcal{M}_X = 1.52 \pm 0.02$  if a counter merger shock is present. The true value of the Mach number could be higher since the X-ray emission in the region beyond the SB jump location contains emission from the in-falling materials (e.g. Wang et al. 2016) which might lower the apparent X-ray SB jump and the derived Mach number. In the radio bands, the spatial energy distribution of the radio emission in Fig. 4.6 does not indicate a clear spectral steepening in the inner region from the X-ray SB jump as it has been observed in a number of shock-related relics (e.g. Orrù et al. 2007; Giacintucci et al. 2008; Stroe et al. 2013; Bonafede et al. 2014; van Weeren et al. 2010, 2016c, 2017; Hoang et al. 2018a). This might be due to the large errors associated with the spectral index measurements. However, if the NE radio emission is related to a shock, the spectral index of  $-1.08 \pm 0.12$  at the outermost region would imply a shock Mach number of  $\mathcal{M}_{NE} = 2.1 \pm 0.2$ , a higher prediction than the value we obtained from the X-ray data (i.e.  $\mathcal{M}_X = 1.52 \pm 0.02$ ).

## 4.6 Conclusions

We present multi-frequency radio continuum images of the merging galaxy cluster A520 using the new LOFAR 145 MHz data and the archival GMRT 323 MHz and VLA 1.5 GHz data. Combining the multi-frequency radio data sets, we study the morphology and spectral energy distribution of the extended radio emission from the ICM. We also re-analyze the existing Chandra X-ray data to search for the possible counter shock in the NE region that was pointed out in Wang et al. (2016). Listed below are the main results.

- We confirm the presence of the large-scale ( $760 \times 950 \text{ kpc}^2$ ) synchrotron radio emission from the cluster that was detected with the VLA 1.4 GHz observations (e.g. Giovannini et al. 1999; Govoni et al. 2001b; Vacca et al. 2014). The radio emission in the SW region is enhanced behind the X-ray detected shock. The spectral index measured at the SW radio edge is consistent with the DSA model (acceleration or re-acceleration), assuming the shock Mach number measured with the X-ray observations ( $\mathcal{M}_X = 2.4_{-0.2}^{+0.4}$ ; Wang et al. 2018). A spectral steepening is also detected from the SW edge toward the cluster center. The radio emission is brightest at the steep spectrum region behind the shock front which is unexpected due to the shock



(re-)accelerated electrons age in the downstream region. This might suggest a mixing/projection between halo and the downstream emission from shock (re-)accelerated particles.

- Our analysis on the new 20 arcsec spectral index map indicates that the extended emission might consist of a radio halo in the center and, possibly, two other sources in the SW and NE regions. No strong variations of the spectral index of the halo are measured. Furthermore, the radio brightness of the halo is fairly flat and poorly correlated with the X-ray brightness. These facts may suggest that the halo is generated in an extensive turbulent cocoon swept by the outgoing shocks rather than from the very central regions where complex substructures are seen in the X-ray emission.
- We do not detect extended radio emission in front of the SW shock with the radio observations at 145 MHz, 323 MHz, and 1.5 GHz. This disagrees with the prediction by the gas adiabatic compression model. Our results are in line with a recent study in Wang et al. (2018).
- We detect an X-ray SB discontinuity in the NE region of the cluster, as was also pointed out in Wang et al. (2016), which might indicate the presence of a counter merger shock ( $\mathcal{M}_{\text{NE}}^{\text{X}} = 1.52 \pm 0.02$ ). In the same region, a small enhancement of radio emission is visible at high frequencies. If the NE radio emission is shock related, we might detect the steepening of the spectral index behind the X-ray discontinuity. However, we are unable to confirm this due to the large uncertainty in our spectral measurements.

## Acknowledgments

We thank the anonymous referee for the helpful comments. DNH, TS, and HR acknowledge support from the ERC Advanced Investigator programme NewClusters 321271. RJvW acknowledges support from the VIDI research programme with project number 639.042.729, which is financed by the Netherlands Organisation for Scientific Research (NWO). The LOFAR group in Leiden is supported by the ERC Advanced Investigator programme New-Clusters 321271. AD acknowledges support by the BMBF Verbundforschung under the grant 05A17STA. FdG is supported by the VENI research programme with project number 639.041.542, which is financed by the Netherlands Organisation for Scientific Research (NWO). This paper is

based (in part) on data obtained with the International LOFAR Telescope (ILT) under project code LC7\_025. LOFAR (van Haarlem et al. 2013) is the Low Frequency Array designed and constructed by ASTRON. It has observing, data processing, and data storage facilities in several countries, which are owned by various parties (each with their own funding sources), and are collectively operated by the ILT foundation under a joint scientific policy. The ILT resources have benefitted from the following recent major funding sources: CNRS-INSU, Observatoire de Paris and Université d'Orléans, France; BMBF, MIWF-NRW, MPG, Germany; Science Foundation Ireland (SFI), Department of Business, Enterprise and Innovation (DBEI), Ireland; NWO, The Netherlands; The Science and Technology Facilities Council, UK; Ministry of Science and Higher Education, Poland. We thank the staff of the GMRT that made these observations possible. GMRT is run by the National Centre for Radio Astrophysics of the Tata Institute of Fundamental Research. The National Radio Astronomy Observatory is a facility of the National Science Foundation operated under cooperative agreement by Associated Universities, Inc. The scientific results reported in this article are based in part on data obtained from the Chandra Data Archive, observations made by the Chandra X-ray Observatory and published previously in cited articles. This research has made use of software provided by the Chandra X-ray Center (CXC) in the application packages CIAO, ChIPS, and Sherpa.



# 5 | Characterizing the radio emission from the binary galaxy cluster merger Abell 2146

## Abstract

The collisions of galaxy clusters generate shocks and turbulence in the intra-cluster medium (ICM). The presence of relativistic particles and magnetic fields is inferred through the detection of extended synchrotron radio sources, such as haloes and relics, and implies that merger shocks and turbulence are capable of (re-)accelerating particles to relativistic energies. However, the precise relationship between merger shocks, turbulence and extended radio emission is still unclear. Studies of the most simple binary cluster mergers are important to help understand the particle acceleration in the ICM. Our main aim is to study the properties of the extended radio emission and the particle acceleration mechanism(s) associated with the generation of relativistic particles in the ICM. We measure the low-frequency radio emission from the merging galaxy cluster Abell 2146 with LOFAR at 144 MHz. We characterize the spectral properties of the radio emission by combining these data with archival GMRT at 238, 612 MHz and VLA at 1.5 GHz data. Behind the NW and SE shocks we observe extended radio emission at 144 MHz. Across the NW extended source, the spectral index steepens from  $-1.06 \pm 0.06$  to  $-1.29 \pm 0.09$  in the direction of the cluster center. This spectral behavior suggests that a relic is associated with the NW upstream shock. The precise nature of the SE extended emission is unclear. It may be a radio halo bounded by a shock or a superposition of a relic and halo. At 144 MHz, we detect a faint emission which was not seen with high-frequency observations, implying a steep ( $\alpha < -1.3$ ) spectrum nature of the bridge emission. Our results imply that the extended radio emission in Abell 2146 is probably associated with shocks and turbulence during cluster merger. The relativistic electrons in the NW and SE may originate from fossil plasma and thermal electrons, respectively.

D. N. Hoang, T. W. Shimwell, R. J. van Weeren, et al.,  
Astronomy & Astrophysics, 622, A21 (2019)

## 5.1 Introduction

Extended radio synchrotron emission ( $\sim$  Mpc-scale) in clusters is generally associated with large-scale shocks and turbulence that are generated in the intra-cluster medium (ICM) during the formation of galaxy clusters (see, e.g., Ferrari et al. 2008; Feretti et al. 2012; Brunetti & Jones 2014 for reviews). The detection of this emission reveals the presence of relativistic particles (i.e. cosmic rays, CRs) and magnetic fields in the ICM. Based on its physical properties, the extended emission is commonly classified as either a relic or a halo (e.g. Kempner et al. 2004). Radio relics are elongated, highly polarized, steep spectrum sources that are usually observed at the cluster periphery. Radio haloes are roundly-shaped, apparently unpolarized sources that are found in the central regions of clusters. Due to the short cooling timescale of the radio-emitting relativistic electrons through synchrotron and inverse-Compton (IC) energy losses in  $\sim \mu\text{G}$  magnetic fields, the  $\sim$  Mpc scale of radio relics and haloes implies that CRs must be (re-)accelerated in situ (Jaffe 1977).

The favored mechanism of particle acceleration in haloes is where CRs are energized by turbulence during cluster mergers (e.g. Brunetti et al. 2001; Petrosian 2001; Fujita et al. 2003; Cassano & Brunetti 2005; Brunetti & Lazarian 2007, 2016; Pinzke et al. 2017). The collisions of the relativistic protons and thermal protons in the ICM (i.e. the hadronic model), that produce secondary relativistic electrons, may also contribute to the observed radio emission (e.g. Dennison 1980; Blasi & Colafrancesco 1999; Dolag & Ensslin 2000; Miniati et al. 2001; Pfrommer & Enßlin 2004; Pfrommer 2008; Keshet & Loeb 2010; Enßlin et al. 2011). However, pure hadronic models for radio haloes are severally challenged by limits from Fermi-LAT observations (e.g. Jeltema & Profumo 2011; Brunetti et al. 2012; Zandanel et al. 2014; Ackermann et al. 2010, 2016), although hadronic models in which secondary particles are re-accelerated by turbulence might be still possible to explain the radio emission in haloes Brunetti & Lazarian (2011a); Brunetti et al. (2017); Pinzke et al. (2017). The generation and dissipation of turbulence in the ICM is a complicated process and involves a complex chain of mechanisms (see, e.g., Brunetti & Jones 2014, for review). For example, the gravitational potential induced by the motion of dark matter sub-haloes can cause a mixing of the gas and a stretching of the magnetic fields in the ICM generating instabilities at different scales (e.g. Cassano & Brunetti 2005; Fujita et al. 2004; ZuHone et al. 2013; Miniati 2014). Also merger shocks driven in the ICM can generate turbulence at different scales

via baroclinic and compressive processes (e.g. Iapichino & Niemeyer 2008; Iapichino et al. 2008, 2011; Vazza et al. 2017).

The relativistic electrons in relics are thought to be more locally generated through Fermi-I acceleration by cluster-scale shocks during the collisions of sub-clusters/groups (e.g. Enßlin et al. 1998; Roettiger et al. 1999). The observation evidence for this is that radio relics have been observed at the location of some X-ray shock fronts (e.g. Shimwell et al. 2015; Botteon et al. 2016a; Eckert et al. 2016; Akamatsu et al. 2017; van Weeren et al. 2016c, 2017; Urdampilleta et al. 2018). The steepening of the radio spectral index across the width of the elongated relics provides additional evidence that relativistic electrons in relics are (re-)accelerated at shock fronts and lose their energy in the post-shock region due to synchrotron and IC energy losses (e.g. Giacintucci et al. 2008; van Weeren et al. 2010; Stroe et al. 2013; Hoang et al. 2017; Hindson et al. 2014). Moreover, the alignment of magnetic field vectors along the length of some relics implies a compression of the magnetic fields in these regions which is an expected consequence of a passing shock front (e.g. Bonafede et al. 2009, 2012; Kale et al. 2012; de Gasperin et al. 2014; Pearce et al. 2017; Hoang et al. 2018a).

Despite of the observational evidence associating radio relics with shocks, radio relics have not been firmly detected at all known strong ( $\mathcal{M} \approx 2 - 3$ ) cluster shocks. For example, relics are not obviously associated with shocks in Abell 520 (e.g. Markevitch et al. 2005; Govoni et al. 2001b; Vacca et al. 2014; Hoang et al. 2018a, submitted), the western edge of the Bullet cluster (1E 065 – 558; e.g. Markevitch et al. 2002; Shimwell et al. 2014), Abell 665 (e.g. Feretti et al. 2004; Dasadia et al. 2016), and Abell 2146 (e.g. Russell et al. 2010; Hlavacek-Larrondo et al. 2018). In these regions, extended radio emission is either undetected at the shocks (e.g. Abell 665), the spectrum of the observed radio emission does not steepen in the post-shock region (e.g. the Bullet cluster) or the distribution of spectral index has not been obtained (e.g. Abell 2146). Moreover, polarimetric measurements have not been reported for most of these clusters, except for the Bullet cluster. The non-detection of radio relics at these shocks would challenge the shock-related formation model of radio relics, however observational limitations should be carefully sorted out. To address this problem, we have performed new low-frequency radio observations of galaxy clusters with prominent shocks but debated or no radio relic emission, i.e., Abell 520 (Hoang et al. 2018b), Abell 665, and Abell 2146 (Hoang et al. 2018c).

## 5.2 The galaxy cluster Abell 2146

Abell 2146 (hereafter A2146;  $z = 0.232$ ) is a binary merging galaxy cluster where the first core passage occurred approximately 0.24-0.28 Gyr ago in the plane of the sky. (e.g. Russell et al. 2010, 2011, 2012; Rodríguez-Gonzálvez et al. 2011; Canning et al. 2012; White et al. 2015; King et al. 2016; Coleman et al. 2017; Hlavacek-Larrondo et al. 2018). The total mass of A2146 is estimated to be  $M_{500} = (4.04 \pm 0.27) \times 10^{14} M_{\odot}$  (Planck Collaboration et al. 2016). Chandra X-ray observations revealed a NW-SE elongation and a highly disturbed morphology of the thermal ICM (Russell et al. 2010). Detailed analysis of the X-ray surface brightness (SB) and temperature distribution revealed a bow shock in the SE region and an upstream shock in the NW region (Russell et al. 2010, 2012). From the jumps in the X-ray derived density profiles, Russell et al. (2012) estimated Mach numbers of  $\mathcal{M}_{SE}^X = 2.3 \pm 0.2$  and  $\mathcal{M}_{NW}^X = 1.6 \pm 0.2$  for the SE and NW shocks, respectively. Despite A2146 being a highly disturbed cluster with clear shock fronts, initially radio observations did not detect extended radio emission from the cluster (Russell et al. 2011). However, recently Hlavacek-Larrondo et al. (2018) discovered radio emission extending up to  $\sim 850$  kpc with deep VLA L-band observations. The  $\sim 30$  arcsec-resolution VLA L-band image shows two separated patches of extended emission in the NW and SE regions. Based on the location and morphology, Hlavacek-Larrondo et al. (2018) suspect that the NW emission is a radio relic associated with the NW upstream shock. Although Hlavacek-Larrondo et al. (2018) suggested that the SE emission might be a radio halo, they also speculated whether or not it may consist of a halo and a relic which could not be separated with their low-resolution VLA image. However, for both the NW and SE regions key observational evidence to connect the extended radio emission (i.e. relics) with the shocks (i.e. spectral steepening in the post-shock regions and the alignment of magnetic fields at the shock fronts) is still missing. Thus, the precise nature of the diffuse radio emission in A2146 still needs to be determined.

In this paper, we present deep LOFAR 120 – 168 MHz observations of A2146. We aim to map the extended emission from A2146 at 144 MHz with a high resolution ( $\lesssim 15$  arcsec). To study spectral properties of the radio emission from the cluster, we combine the LOFAR 144 MHz data with the existing VLA 1 – 2 GHz data presented in Hlavacek-Larrondo et al. (2018) and the archival GMRT 222 – 254 and 596 – 628 MHz data. We assume the cosmological parameters,  $H_0 = 70 \text{ km s}^{-1} \text{ Mpc}^{-1}$ ,  $\Omega_M = 0.3$ , and  $\Omega_{\Lambda} = 0.7$ .

In this cosmology, 1 arcmin corresponds to 221.88 kpc at  $z = 0.232$ .

## 5.3 Observations and data reduction

### 5.3.1 LOFAR 144 MHz

A2146 was observed for a total of 16 hours split over two dates (ObsID: L589831 and L6311955) with LOFAR (Haarlem et al. 2013). One of the observations (i.e. L589831) forms part of the LOFAR Two-meter Sky Survey (LoTSS; Shimwell et al. 2017) and has a pointing center of  $1.3^\circ$  from the target. The other is a targeted observation centered on A2146. A summary of the observations is given in Table 5.1.

We have calibrated the LOFAR data to correct for direction-independent and direction-dependent effects using the facet calibration technique described in van Weeren et al. (2016a) and Williams et al. (2016) and summarized here for completeness. The direction-independent calibration (see de Gasperin et al. (2018) for an overview of direction independent effects) is done using the PreFactor<sup>1</sup> pipeline which includes flagging radio frequency interference (RFI), removing contamination from bright sources in the distant sidelobes (i.e. Cassiopeia A and Cygnus A), correcting the amplitude gain, the initial clock offsets and XX-YY phase offsets. The calibration parameters were derived from 10 min observations of the primary calibrators 3C 196 and 3C 295 (Obs. IDs: L589831 and L6311955). The 3C 196 and 3C 295 models used to calibrate these data have integrated flux densities which are consistent with the Scaife & Heald (2012) flux scale. After the target data are calibrated with the solutions derived from the calibrator observations, the data are phase calibrated against a wide-field sky model obtained from the TIFR GMRT 150 MHz All-sky Radio Survey: First Alternative Data Release (TGSS-ADR1; Intema et al. 2017). The direction-dependent calibration is performed separately on each dataset using the Factor<sup>2</sup> pipeline which aims to correct for ionospheric distortions and errors in the primary beam model to allow for accurate calibration in the direction of A2146.

To obtain continuum images, the data calibrated in the direction of A2146 were deconvolved with MS – MFS (multiscale-multifrequency) with  $n_{\text{terms}} = 2$  and W–projection options in the Common Astronomy Software Applications package (CASA) to account for the frequency dependence

---

<sup>1</sup><https://github.com/lofar-astron/prefactor>

<sup>2</sup><https://github.com/lofar-astron/factor>



Table 5.1: Observation details

Telescope	LOFAR 144 MHz	GMRT 238 MHz	GMRT 612 MHz	VLA 1.5 GHz
Project codes	LC7_024, DDT9_001	20_065	20_065, 12DDT009	12A-029
Configurations	–	–	–	B, C, D
Observing dates	Apr. 25, 2017; Dec. 7, 2017	Jun. 05, 2011	Jun. 05, 2011; Mar. 17, 2012	Jun. 9, 2012 (B); Mar. 16, 2012 (C); Apr. 22, 2012 (C); Jan. 27, 2013 (D)
Obs. IDs	L589831, L631955	5369	5369, 5888	–
Calibrators	3C 295, 3C 196	3C 48	3C 286	3C 286, J1634+6245
Bandwidth (MHz)	48	32	32	1000
Total on-source time (hr)	16	8.7	15	11.1
Integration time (s)	1	16	16	3 (B), 5 (C, D)
Correlations	XX, XY, YX, YY	RR, LL	RR, LL	RR, RL, LR, LL (B, D) RR, LL (C)
Number of antennas	62	28	28, 30	15, 16

of the sky and non-coplanar effects (Cornwell et al. 2005, 2008; Rau & Cornwell 2011). To map emission at different scales, we make continuum images with various different weightings of the visibilities. All continuum images that were obtained from the observations were corrected for primary beam attenuations. To minimize the uncertainty in the LOFAR flux scale, the LOFAR images obtained from the observations L589831 and L6311955 are multiplied by factors of 1.02 and 1.18, respectively; where these scaling factors were obtained by comparing the integrated flux densities of nearby compact sources in the LOFAR images with those from the TGSS-ADR1 (Intema et al. 2017). The pixel values for the final combined continuum image are calculated as the average of the primary beam, corrected images, weighted by the local noise in each image.

### 5.3.2 GMRT 238 and 612 MHz

The GMRT 238 and 612 MHz observations of A2146 were carried out on Jun. 5, 2011 and Mar. 17, 2012 (Obs. IDs: 5369 and 5888). Table 5.1 provides more details on the observations. Each data set was separately calibrated using the Source Peeling and Atmospheric Modeling package (SPAM; Intema et al. 2009, 2017). This calibration mainly aims to correct for the ionospheric distortion which includes an interferometric phase delay. The amplitude gains were calibrated according to the flux scale in Scaife & Heald (2012). The flux scale error of 10% is used for the GMRT observations (e.g. Chandra et al. 2004). The final continuum images of A2146 at 612 MHz were obtained by averaging the primary beam corrected images from the different observations.

### 5.3.3 VLA 1.5 GHz

A2146 was observed for a total of 11.1 hours with the VLA at 1.5 GHz in B, C and D configurations on multiple dates in 2012 and 2013. The frequency bandwidth is divided into two intermediate frequency (IF) pairs, each of which has 8 sub-bands of 64 MHz. The observations were done with full-polarization settings. The integration time was set at 3 seconds for the B-configuration and 5 seconds for the C- and D-configurations. More details on the VLA observations are given in Table 5.1.

The calibration for each configuration of the VLA datasets was done separately in CASA by Hlavacek-Larrondo et al. (2018). For a full description of the procedure, we refer to Hlavacek-Larrondo et al. (2018). To obtain continuum images, the calibrated data of the B-, C- and D-configurations

were combined and imaged with the MS – MFS and W–projection algorithms in CASA.

### 5.3.4 Spectral measurements

We make a spectral index map to study the spectral energy distribution of the extended emission from A2146. The spectral index map is made with the LOFAR 144 MHz and VLA 1.5 GHz data. The LOFAR and VLA continuum images used for the spectral index mapping are imaged with the same parameters (i.e. uv-range of 0.12 – 65 k $\lambda$ , Briggs’ robust weighting of 0.0, outertaper of 15 arcsec and 30 arcsec for the LOFAR and VLA, respectively, to obtain an approximate resolution of 30 arcsec). The spectral index<sup>3</sup> and the corresponding error for each pixel are estimated as

$$\alpha = \frac{\ln \frac{S_1}{S_2}}{\ln \frac{\nu_1}{\nu_2}} \quad \text{and} \quad \Delta\alpha = \frac{1}{\ln \frac{\nu_1}{\nu_2}} \sqrt{\left(\frac{\Delta S_1}{S_1}\right)^2 + \left(\frac{\Delta S_2}{S_2}\right)^2}, \quad (5.1)$$

where  $\Delta S_i = \sqrt{(\sigma_i)^2 + (f_{\text{err}} S_i)^2}$  with  $i = [1, 2]$  is the total error associating with the flux density measurement  $S_i$ ; and the subscripts 1 and 2 stand for 144 MHz and 1.5 GHz, respectively. The total error is propagated from the flux scale uncertainty (i.e.  $f_{\text{err}} = 15\%$  and  $5\%$  are commonly used for the LOFAR and VLA observations, respectively) and the image noise ( $\sigma$ ).

## 5.4 Results and discussion

In Fig. 5.1, we present LOFAR 144 MHz continuum images of A2146. In this section, we estimate flux densities and spectral index for the compact and extended sources in the cluster and discuss the implications.

### 5.4.1 The radio galaxies

A2146 is known to host two bright radio galaxies (namely A2146-A and A2146-B) that are located in the central regions of the NW and SW sub-clusters (see Fig. 5.1, left). One of these is the brightest cluster galaxy (BCG) belonging to the SE sub-cluster (e.g. Russell et al. 2011). In projection, the radio galaxies are approximately coincident with the extended non-thermal emission from the ICM (Hlavacek-Larrondo et al. 2018) and are situated behind the SE and NW merger shocks (e.g. Russell et al. 2011).

---

<sup>3</sup>In this paper, we use the convention  $S \propto \nu^\alpha$

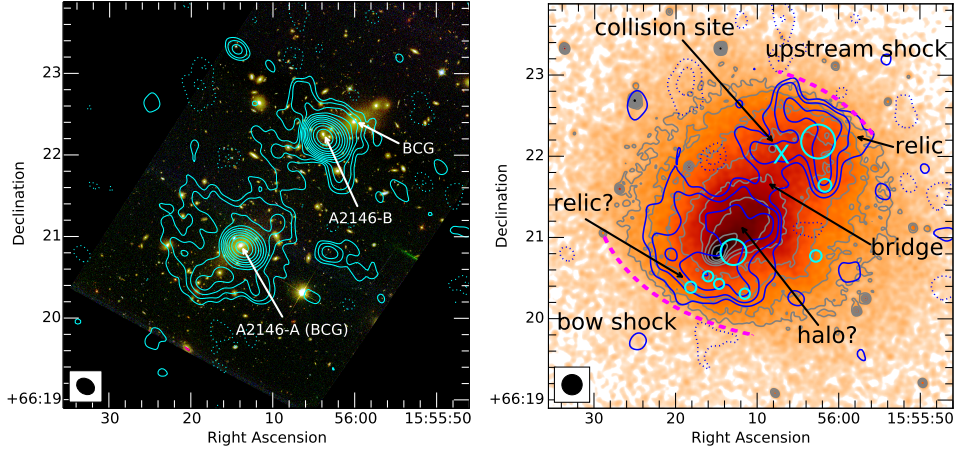


Figure 5.1: HST composite optical (left) and Chandra (right) images overlaid with the LOFAR 144 MHz contours (blue in the right panel). The resolutions of the LOFAR contours shown in the bottom-left corner are  $14\text{arcsec} \times 11\text{arcsec}$  ( $P.A. = 55^\circ$ , left) and  $15\text{arcsec} \times 15\text{arcsec}$  (right). In the right panel, the compact radio sources marked with the cyan circles are subtracted in the uv-data. The magenta dashed lines show the shock locations. In both images, the LOFAR contours start from  $\pm 2.5\sigma$  (dotted negative), where  $\sigma = 135$  and  $160\ \mu\text{Jy beam}^{-1}$  in the left and right panels, respectively. The Chandra first contour is  $2 \times 10^{-9}\ \text{cts cm}^{-2}\text{s}^{-1}\text{arcsec}^{-2}$ . The next contours are spaced by a factor of  $\sqrt{3}$ .

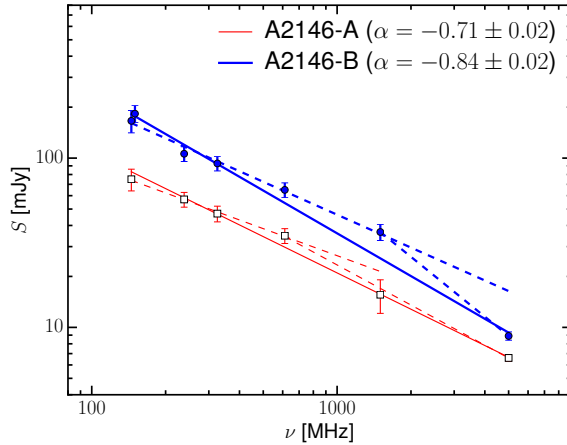


Figure 5.2: The spectral energy distribution between 144 MHz and 5 GHz for A2146-A and A2146-B. The flux densities are summarized in Table 5.2.

Table 5.2: Flux density for the radio galaxies in the vicinity of A2146.

Freq. (MHz)	$S_{\text{A2146-A}}$ (mJy)	$S_{\text{A2146-B}}$ (mJy)	Telescope	Ref.
144	$75 \pm 11$	$166 \pm 25$	LOFAR	this paper
150	–	$183 \pm 21$	GMRT	<i>a</i>
238	$56.8 \pm 5.7$	$106.1 \pm 10.6$	GMRT	this paper
325	$47 \pm 5$	$93 \pm 9$	GMRT	<i>b</i>
612	$37.8 \pm 3.8$	$67.6 \pm 6.8$	GMRT	this paper
1400	$15.6 \pm 3.5$	$36.6 \pm 4.0$	VLA	<i>a</i>
5000	$6.6 \pm 0.3$	$8.9 \pm 0.5$	VLA	<i>c, a</i>

Notes: *a*: Hlavacek-Larrondo et al. (2018), *b*: Russell et al. (2011),  
*c*: Hogan et al. (2015)

The total flux density of these sources at 144 MHz is  $75 \pm 11$  mJy for A2146-A (i.e. the SE BCG) and  $166 \pm 25$  mJy for A2146-B. We also obtained measurements at 150 MHz from the TGSS-ADR1 (Intema et al. 2017), 325 MHz (Russell et al. 2011), 612 MHz (see Sec. 5.3.2), VLA 1.5 GHz (Hlavacek-Larrondo et al. 2018) and 5 GHz (Hogan et al. 2015; Hlavacek-Larrondo et al. 2018) observations and present the spectral properties of these sources in Fig. 5.2 and Table 5.2. Since both A2146-A and A2146-B are present in the TGSS-ADR1 150 MHz image, but A2146-A resides in the region that has high background and is only detected at  $\lesssim 2\sigma$ , we exclude the TGSS-ADR1 flux density measurements for A2146-A in this analysis.

To estimate the integrated spectral indices for A2146-A and A2146-B, we fit their spectra with an exponential function,  $S \propto \nu^\alpha$ . In the fitting, the flux densities are weighted by the inverse square of the flux density errors. We find that the average spectral index is  $-0.71 \pm 0.02$  for A2146-A and  $-0.84 \pm 0.02$  for A2146-B. However, the spectral energy distribution in Fig. 5.2 hints at possible spectral breaks at about 612 MHz and 1.5 GHz for A2146-A and A2146-B, respectively. To quantify this, we fit the radio flux density of the galaxies with a double-power-law function. The resulting spectral indices are  $\alpha_{144\text{ MHz}}^{612\text{ MHz}} = -0.53 \pm 0.11$  and  $\alpha_{612\text{ MHz}}^{5\text{ GHz}} = -0.79 \pm 0.05$  for A2146-A and  $\alpha_{144\text{ MHz}}^{1.5\text{ GHz}} = -0.64 \pm 0.06$  and  $\alpha_{1.5\text{ GHz}}^{5\text{ GHz}} = -1.17 \pm 0.10$  for A2146-B where in both cases the spectral index steepens at high frequencies. The spectral steepening of A2146-A and A2146-B at high frequencies might be due to the synchrotron and IC energy losses of the radio emitting particles.

It is noted that the spectrum below 612 MHz for A2146-A roughly follows a single power law function,  $S \propto \nu^\alpha$ , and does not indicate a sharp

turnover at low frequencies as reported in Hlavacek-Larrondo et al. (2018) which used GMRT 150 MHz data.

#### 5.4.2 The NW extended emission

In Fig. 5.1, the NW radio emission extends over a region of  $200 \times 310 \text{ kpc}^2$ . The NW radio emission is elongated in the NE-SW direction which is approximately perpendicular to the merger axis (e.g. White et al. 2015). The outer edge of the NW radio emission is located behind the detected upstream X-ray shock (Russell et al. 2010). The integrated flux densities of the NW emission measured within the  $2.5\sigma$  contours are  $S_{144 \text{ MHz}} = 13.1 \pm 2.0 \text{ mJy}$  and  $S_{1.5 \text{ GHz}} = 0.89 \pm 0.08 \text{ mJy}$ , resulting in an integrated spectral index of  $\alpha = -1.14 \pm 0.08$ . This spectral index measurement for the NW radio emission is typical value for an elongated relic known (i.e.  $\bar{\alpha} \approx -1.3$ ; Feretti et al. 2012). However, our spectral index is flatter than the 1-2 GHz in-band measurement of  $\alpha_{1-2 \text{ GHz}} = -2.3 \pm 0.3$  that was reported in Hlavacek-Larrondo et al. (2018). As mentioned by Hlavacek-Larrondo et al. (2018), the true uncertainty of the in-band spectral measurement is likely higher. However, if the true value of the 1-2 GHz spectral index of the NW emission is indeed this steep then it would imply a spectral curvature between 144 MHz and 1.5 GHz. Unfortunately, we are unable to check this possibility because the NW extended emission has only been detected at 144 MHz and 1.5 GHz.

To examine the distribution of the spectral index and search for a spectral index gradient that is often associated with radio relics, we make the spectral index map in Fig. 5.3 and the spectral index profile in Fig. 5.4. In the spectral index profile a steepening of the spectral index of the NW emission approximately along the merger axis is apparent. In the outer region, the spectral index is  $-1.06 \pm 0.06$ , but steepens to  $-1.29 \pm 0.09$  in the inner region about 170 kpc from the outer  $2.5\sigma$  contour. Since we examine the spectral trend, the flux scale errors due to the amplitude calibration are not used in the calculation of the spectral index errors. We emphasize that due to the limited resolution of our spectral index map we are only able to make two independent measurements of the spectral index in the region of NW emission and that it is important to confirm the spectral gradient across the NW extended radio emission with high-resolution observations.

Basing on the morphology of the NW radio emission, Hlavacek-Larrondo et al. (2018) concluded that it is likely a radio relic. A number of radio relics have been observed to have steeper spectra toward the cluster center (e.g. Bonafede et al. 2009; Kale et al. 2012; de Gasperin et al. 2015; van

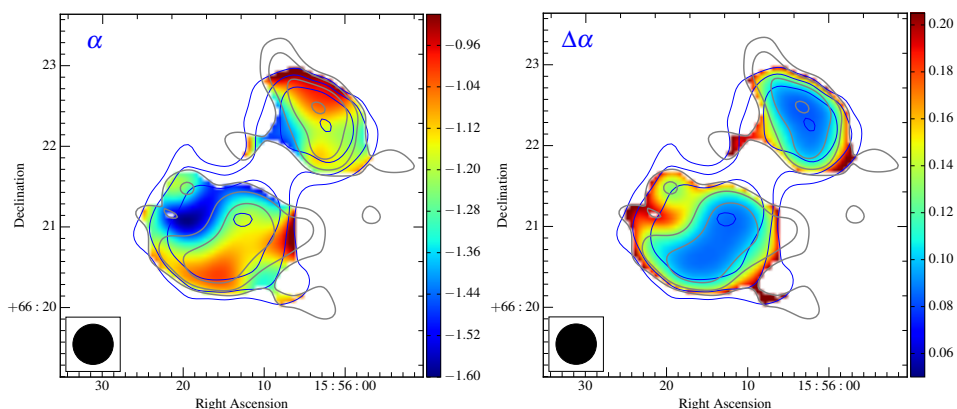


Figure 5.3: The 30 arcsec-resolution spectral index (left) and error (right) maps between 144 MHz – 1.5 GHz for the extended radio emission from A2146. In both images, the LOFAR 144 MHz (blue) and VLA 1.5 GHz (gray) first contours are  $2.5\sigma$ , where  $\sigma = 340$  and  $27 \mu\text{Jy beam}^{-1}$  for the LOFAR 144 MHz and VLA 1.5 GHz data, respectively. The next contours are multiplied by  $\sqrt{3}$ .

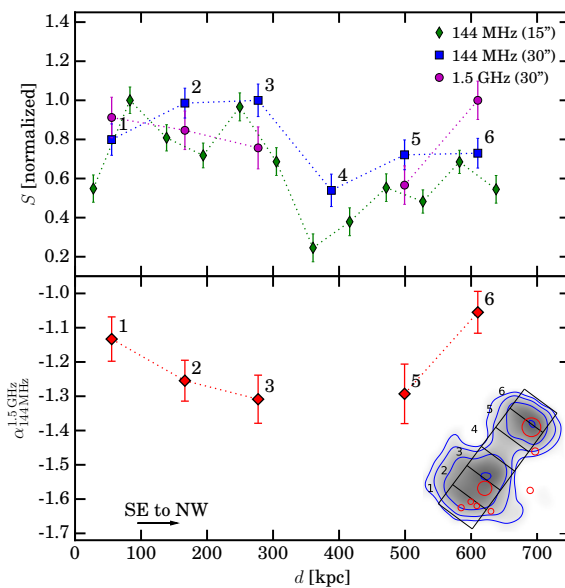


Figure 5.4: The SB (top) and spectral index (bottom) profiles for the extended radio emission from A2146. The flux scale errors are not added to the total errors of the flux densities. The numbers next to the data points indicate the region numbers shown in overlaid image. The red circular regions at the locations of the subtracted compact sources are masked.

Weeren et al. 2010, 2017). The spectral steepening is due to the energy losses through the synchrotron and IC emission. In the spectral analysis above, we show that the radio spectral index in the region behind the NW shock front is steeper than that in the outer edge, which supports the nature of the NW extended radio emission being a radio relic. Its location and spectral properties imply that the NW extended emission is likely to be associated with the NW upstream shock. Shocks will compress ICM magnetic fields resulting in polarized radio emission. Therefore, new radio polarization observations will provide further information on the relation between the shock and extended emission in the NW region of the cluster.

According to the diffusive shock acceleration (DSA) (e.g. Blandford & Eichler 1987), a shock of Mach number  $\mathcal{M}$  should accelerate thermal electrons and generate a population of relativistic electrons with an energy spectrum,

$$\frac{dN}{d\gamma} = N_0 \gamma^{-\delta_{\text{inj}}}, \quad (5.2)$$

where  $N_0$  and  $\gamma$  are the spectral normalization and Lorentz factors, respectively; the spectral slope  $\delta_{\text{inj}}$  is related to the shock Mach number via

$$\delta_{\text{inj}} = 2 \frac{\mathcal{M}^2 + 1}{\mathcal{M}^2 - 1}. \quad (5.3)$$

In the presence of magnetic fields, the relativistic electrons emit synchrotron radiation with a spectrum of  $I \propto \nu^{\alpha_{\text{inj}}}$ , where  $\alpha_{\text{inj}} = (1 - \delta_{\text{inj}})/2$ . The NW upstream shock in A2146 has a Mach number of  $\mathcal{M} = 1.6 \pm 0.1$  that was derived from the X-ray SB jump (Russell et al. 2012). According to the DSA model, we should therefore observe radio emission along the shock with an injection spectral index of  $\alpha_{\text{inj}} = -1.78^{+0.22}_{-0.32}$ . This prediction is steeper than our estimate (i.e.  $\alpha_{\text{inj}} = -1.06 \pm 0.09$  which takes into account the flux scale errors of 15% and 5% for LOFAR and VLA, respectively). The discrepancy should not be caused by the resolution of the radio observations because if there is indeed a spectral index gradient then at higher resolution the index would be even flatter in the region closer to the shock front. The discrepancy could be because the shock is not powerful enough to efficiently accelerate thermal electrons and is instead (re-)accelerating pre-existing fossil electrons. Such electrons could be remnants of lobes of radio galaxies (e.g. Markevitch et al. 2005; Kang et al. 2012). In this scenario, the shock increases the brightness of the radio emission, but preserves the spectrum of the pre-shock fossil electrons if the fossil electrons have flatter spectrum than that generated by the shock (e.g. Markevitch et al. 2005). If fossil



electrons were being re-accelerated we may see extended radio emission in front of the shock (Markevitch et al. 2005) but this is not present in the LOFAR 144 MHz and VLA 1.5 GHz observations (Figs. 5.1 and 5.3). Finally, we do note that the spectral index of  $-1.06$  that we estimated for the NW outer region is the typical value for the lobes of radio galaxies although unlike van Weeren et al. (2017) the potential source of the fossil electrons in the NW region of the cluster is not obvious.

As discussed in van Weeren et al. (2016c) for the Toothbrush relic, an alternative explanation for the mismatch of injection indices obtained from the radio observations and the DSA model is that the shock might contain different Mach numbers along the line of sight (e.g. Skillman et al. 2011, 2013; Vazza et al. 2012). In the case of a nonlinear dependence of the Mach numbers on the acceleration efficiency (e.g. Hoeft et al. 2007), the radio observations are particularly sensitive to the shocks with high Mach numbers (resulting in flat spectrum radio emission), while the X-ray observations tend to observe the lower Mach number shocks (corresponding to steep spectrum radio emission). This explanation is supported by recent simulations of particle acceleration at cluster merger shocks in Hong et al. (2015) and Ha et al. (2018). These studies reported that the weighted Mach numbers derived from the gas temperature jumps are smaller than those obtained from the shock kinetic energy flux (i.e. radio data). Hence, the discrepancy between the injection indices derived from spectral index map and the DSA model might be explained if the shock consists of multiple Mach numbers along the line of sight. We note that if we use the Mach number  $\mathcal{M}_{\text{NW}} = 2.0 \pm 0.3$  calculated from temperature jump (Russell et al. 2012), the injection index predicted by the DSA model is  $\alpha = -1.17^{+0.20}_{-0.39}$  which is consistent with our injection spectral measurement (i.e.  $\alpha_{\text{inj}} = -1.06 \pm 0.09$ ). However, Russell et al. (2012) pointed out that the Mach number calculated from the temperature jump is less accurate due to the large radial bins which cannot resolve the shock jump accurately.

The Mach numbers calculated from X-ray SB density jump could be biased low due to projection effects. Without the correction for the projection effects, this bias increases the difference between the X-ray and radio derived Mach numbers (or the DSA predicted and observed injection indices). However, as two sub-clusters in A2146 are known to merge almost on the plane of the sky (i.e. the angle between the merger axis and the plane of the sky is  $\sim 16^\circ$ ; White et al. 2015), the viewing angle to the NW shock is likely to be edge on. Hence, the projection effects might not play an important role in the mismatching of the DSA predicted and radio observed injection

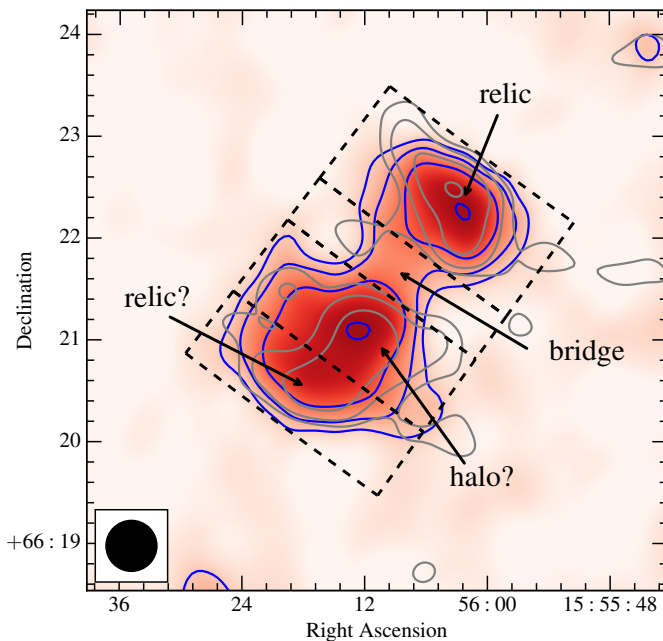


Figure 5.5: Regions (dashed lines) where flux densities were extracted are shown on the LOFAR 144 MHz 30 arcsec-resolution image. The LOFAR 144 MHz (blue) and VLA 1.5 GHz (gray) contours are identical to those in Fig. 5.3.

indices in the NW extended emission.

### 5.4.3 The radio bridge

In Fig. 5.1, the NW relic is connected with the SE extended emission through a faint emission (bridge). We measure the flux density of the radio emission in the bridge using the  $> 2.5\sigma$  pixels within the region of the bridge (see Fig. 5.5). The integrated flux density of the emission in the bridge is 1.1 mJy at 144 MHz, but it is undetected at 1.5 GHz (see Figs. 5.3 and 5.5). We assume the size of the bridge emission at 1.5 GHz is similar to that at 144 MHz. We find that  $1\sigma$  upper limit for the bridge emission at 1.5 GHz is 0.047 mJy. This implies that the integrated spectral index of the emission in the bridge is likely steeper than  $-1.3$ . The elongated morphology of the bridge along the merger axis implies that it likely associates with the turbulence induced by the on-going merger. However, it is still unclear whether or not the bridge emission is a separated source or is part of the SE extended emission.

#### 5.4.4 The SE extended emission

In Fig. 5.1, we show the SE extended emission at 144 MHz. The SE emission has a projected size of  $300 \times 350 \text{ kpc}^2$  and is elongated in the NW-SE direction. The SE edge of the SE emission roughly follows the SE bow shock (e.g. Russell et al. 2010). The integrated flux density of the SE extended emission (without the bridge, see Figs. 5.1 and 5.5) encompassing  $2.5\sigma$  contours is  $24.3 \pm 3.8 \text{ mJy}$  at 144 MHz and  $1.3 \pm 0.1 \text{ mJy}$  at 1.5 GHz. The spectral index between 144 MHz and 1.5 GHz is  $\alpha = -1.25 \pm 0.07$ . Unlike the spectral index estimate for the NW relic, our spectral index measurement for the SE emission is consistent with the VLA in-band estimate of  $-1.2 \pm 0.1$  that was presented in Hlavacek-Larrondo et al. (2018). The spectral index map in Fig. 5.3 shows a patchy distribution in the SE region. Along the SE-NW merger axis, the SE extended emission has a flat spectrum in the SE region and the spectrum becomes steeper toward the NW direction. The trend is more visible in the spectral index profile in Fig. 5.4.

The nature of the SE extended emission is still unclear. Possibilities include: (i) a radio halo bounded by a merger shock (e.g. Markevitch et al. 2005; Shimwell et al. 2014; Markevitch 2010; Brown & Rudnick 2011; van Weeren et al. 2016c); (ii) a radio relic on the SE edge superimposed on a radio halo that extends outwards from the cluster center (e.g. Brunetti et al. 2008; Macario et al. 2011; van Weeren et al. 2016c; Hoang et al. 2017). Scenario (ii) was the favored scenario in Hlavacek-Larrondo et al. (2018). The extended emission in scenarios (i) and (ii) can perhaps be generated by the same merger; but the distinct appearance of the radio emission and its spectrum depends on the shock Mach number, the magnetic field strength behind the shock front, the spectral energy distribution of turbulence after the shock passage, and the observing frequencies (Markevitch 2010). It is noted that the SE edge of the SE extended emission is not spatially coincident with the entire shock front (see Fig. 5.1, right), although the location and orientation of the SE extended emission along the merger axis seems to imply its shock-related origin.

According to scenario (ii) the SE extended emission (Fig 5.1) should consist of two components. To assess this we make surface brightness profiles along the merger axis in Fig. 5.4. To take into account the size of the synthesis beam, each data point is estimated in a region that encompasses a beam (15 arcsec or 30 arcsec). The brightness peaks in the SE extended radio emission are clearest in the 15 arcsec-resolution profile as in the 30 arcsec-resolution profile they are smoothed out. We note that the extended emission maps are obtained by subtracting compact sources (i.e.

cyan circles in Fig. 5.1, right) which will leave some residual flux which contaminates the profiles. However, if there are two separate sources (i.e. halo and relic) in the SE region, the width of the relic can be approximated as the distance from the SE  $2.5\sigma$  contour to the local minimum brightness in the 15 arcsec profile, which is about 170 kpc (Fig. 5.4). With this approximation we are able to estimate the halo flux, where estimates here should be considered as the lower limits for the halo flux density. To have consistent flux measurements at both frequencies, we measure the halo flux densities at 144 MHz and 1.5 GHz using the 30 arcsec images within the regions shown in Fig. 5.5. Only pixels that are detected at  $> 2.5\sigma$ , where  $\sigma = 340$  and  $27 \mu\text{Jy beam}^{-1}$  for the LOFAR 144 MHz and VLA 1.5 GHz images, respectively, are used in the calculation. The integrated flux densities at 144 MHz for the relic and halo regions are 9.0 and 15.3 mJy, respectively. At 1.5 GHz, they are 0.53 and 0.78 mJy, respectively. With these measurements, we find the integrated spectral index to be  $-1.2$  for the tentative relic and  $-1.3$  for the halo. Since the separation of the relic and halo will need verification with high-resolution observations, the flux density estimated here should be considered as a rough estimate. The true value for the flux density of the halo at 144 MHz should lie in between 15.3 mJy (i.e. the SE extended emission consists of a relic and a halo) and 24.3 mJy (i.e. the SE extended emission is a single halo). At 1.5 GHz, it is between 0.78 mJy and 1.31 mJy. If the bridge emission is part of the SE extended emission, the upper limit for the flux density of the halo is 25.4 mJy at 144 MHz and 1.38 mJy at 1.5 GHz. The 1.4 GHz power for radio haloes, which is proportional to the amount of turbulence energy that is converted into the relativistic electrons, is known to correlate with the masses of their host clusters (e.g. Cassano et al. 2013). Using the flux density estimates above for the radio halo, we calculate the power of the A2146 halo at 1.4 GHz is within a range of  $(1.5 - 2.5) \times 10^{23} \text{ W Hz}^{-1}$  (k-corrected). The power of the A2146 halo is consistent with the  $P - M$  scaling relation with a cluster mass of  $M_{500} = (4.04 \pm 0.27) \times 10^{14} M_{\odot}$  (Planck Collaboration et al. 2016) that we present in Fig. 5.6.

Another key observational feature to distinguish whether the extended emission is a single halo (i.e. the case i) or a composition of a halo and a relic (i.e. the case ii) is the distribution of the spectral index of the radio emission along the axis of shock propagation. In case (ii), we expect the spectral index of the radio emission is flat immediately behind the shock front (i.e. due to shock (re-)acceleration or compression), steepening further in the post-shock region (i.e. because of synchrotron and IC losses) and might flatten

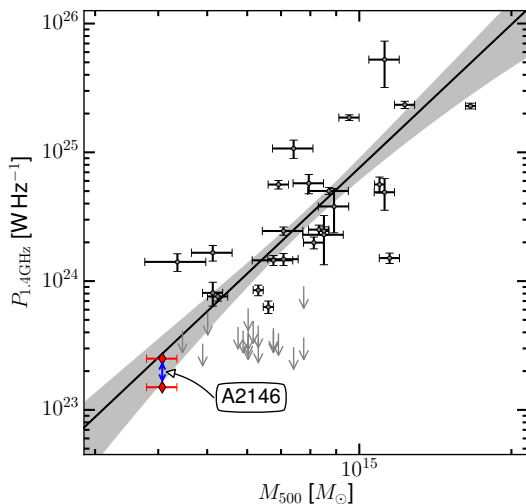


Figure 5.6: The  $P - M$  correlation. The estimated range for the power of the radio halo in A2146 (red points) is roughly consistent with the  $P - M$  scaling relation (i.e. black line). The gray shadow is the 95% confidence region. The downward arrows show upper limits for undetected haloes. For the list of the haloes in the plot, we refer to Cassano et al. (2013).

again in the halo region depending on the amount of turbulent energy induced by the passage of a merger shock available in the ICM. On the other hand, in case (i) whether or not we might see a similar spectral trend across the extended source behind the shock, depending on the physical conditions at the post-shock region. The spectral index of the halo emission might slightly steepen behind the shock and then become uniform across the halo region. These scenarios (i) and (ii) have been recently used to explain the spatial distribution of the spectral index in some clusters. Examples for the case (i) are the SW radio edge in Abell 520 (Hoang et al. 2018b, submitted) and, perhaps, the southern region of the radio halo in the Toothbrush cluster (van Weeren et al. 2016c; Rajpurohit et al. 2018). For case (ii), examples are the northern relics and the haloes in the Toothbrush and Sausage clusters (e.g. van Weeren et al. 2016c; Hoang et al. 2017). Whilst our spectral index maps are too low resolution to make firm conclusions, in the SE extended emission of A2146, there might be a spectral gradient from  $-1.13 \pm 0.06$  to  $-1.25 \pm 0.06$  behind the shock. This tentative trend is in line with that expected for a relic-halo superposition. If the SE extended radio emission is shock (re-)accelerated, the radio spectral index of  $-1.13 \pm 0.06$  in the SE edge implies a shock Mach number of  $\mathcal{M}_{\text{SE}} = 2.0 \pm 0.1$ . This is in line the

value estimated from the X-ray data (i.e.  $\mathcal{M}_{\text{SE}}^{\text{X}} = 2.3 \pm 0.2$ ; Russell et al. 2012), which makes the argument for a connection between the bow shock and the SE edge of the extended radio emission (i.e. the relic) in the SE region of the cluster more compelling.

## 5.5 Conclusions

In this paper, we present the results of deep LOFAR 120 – 168 MHz observations of the binary merging galaxy cluster A2146. We map the extended continuum emission at 144 MHz and the spectral energy distribution in the cluster in more detail than in previous studies. We summarize the results below.

- The LOFAR 144 MHz observations confirm the presence of the NW extended emission that was detected with the deep VLA 1.5 GHz observations (Hlavacek-Larrondo et al. 2018). The radio emission extends behind the upstream shock front and have a flux density of  $13.1 \pm 2.0$  mJy at 144 MHz and  $0.89 \pm 0.08$  mJy at 1.5 GHz. The integrated spectral index is  $\alpha = -1.14 \pm 0.08$ . The spectral index flattens to  $-1.06 \pm 0.06$  in the outer region and steepens to  $-1.29 \pm 0.09$  in the inner region. The morphological and spectral properties of the NW extended emission are consistent with the hypothesis that the NW extended emission is a relic associated with the NW upstream merger shock.
- The DSA model predicts an injection spectral index of  $-1.78_{-0.32}^{+0.22}$  for the  $\mathcal{M}_{\text{NW}} = 1.6 \pm 0.1$  NW shock. However, we measure a spectral index in the outer region of the NW relic to be  $-1.06 \pm 0.09$  (taken into account flux scale errors), which is inconsistent with the DSA prediction. The mismatching of the injection spectrum indices could be explained if the shock re-accelerates a pre-existing population of fossil electrons rather than those in the thermal pool.
- With the LOFAR 144 MHz observations, we detect a faint emission (bridge) connecting the NW and SE regions. The integrated flux density of the radio emission in the bridge is 1.1 mJy at 144 MHz. The non-detection of the bridge with the VLA 1.5 GHz observations implies that the spectral index of the bridge emission is steeper than  $-1.3$ .

- The SE extended emission has an integrated flux density of  $24.3 \pm 3.8$  mJy at 144 MHz and  $1.3 \pm 0.1$  mJy at 1.5 GHz, resulting in  $\alpha = -1.25 \pm 0.07$ . Further analysis of the brightness suggests that the SE extended emission may consist of a halo in the central region and a relic in the SE edge. The power for the radio halo is constrained within  $(1.5-2.5) \times 10^{23} \text{ W Hz}^{-1}$ , which is roughly consistent with the expected power for the cluster mass (i.e.  $M_{500} = (4.04 \pm 0.27) \times 10^{14} M_{\odot}$ ; Planck Collaboration et al. 2016), according to the  $P - M$  scaling relation (Cassano et al. 2013).

## Acknowledgments

DNH and HR acknowledge support from the ERC Advanced Investigator programme NewClusters 321271. RJvW acknowledges support from the VIDI research programme with project number 639.042.729, which is financed by the Netherlands Organisation for Scientific Research (NWO). The LOFAR group in Leiden is supported by the ERC Advanced Investigator programme New-Clusters 321271. This paper is based (in part) on data obtained with the International LOFAR Telescope (ILT) under project code LC7\_024 and DDT9\_001. LOFAR (van Haarlem et al. 2013) is the Low Frequency Array designed and constructed by ASTRON. It has observing, data processing, and data storage facilities in several countries, which are owned by various parties (each with their own funding sources), and are collectively operated by the ILT foundation under a joint scientific policy. The ILT resources have benefitted from the following recent major funding sources: CNRS-INSU, Observatoire de Paris and Université d'Orléans, France; BMBF, MIWF-NRW, MPG, Germany; Science Foundation Ireland (SFI), Department of Business, Enterprise and Innovation (DBEI), Ireland; NWO, The Netherlands; The Science and Technology Facilities Council, UK; Ministry of Science and Higher Education, Poland. Part of this work was carried out on the Dutch national e-infrastructure with the support of the SURF Cooperative through grant e-infra 160022 & 160152. The LOFAR software and dedicated reduction packages on [https://github.com/apmechev/GRID\\_LRT](https://github.com/apmechev/GRID_LRT) were deployed on the e-infrastructure by the LOFAR e-infragroup, consisting of J. B. R. Oonk (ASTRON & Leiden Observatory), A. P. Mechev (Leiden Observatory) and T. Shimwell (ASTRON) with support from N. Danezi (SURFsara) and C. Schrijvers (SURFsara). We thank the staff of the GMRT that made these observations possible. GMRT is run by the National Centre for Radio Astrophysics

of the Tata Institute of Fundamental Research. The National Radio Astronomy Observatory is a facility of the National Science Foundation operated under cooperative agreement by Associated Universities, Inc. The scientific results reported in this article are based in part on data obtained from the Chandra Data Archive, observations made by the Chandra X-ray Observatory and published previously in cited articles. We thank Helen Russell for providing the Chandra X-ray image of Abell 2146 and commenting on the manuscript.





---

## Bibliography

- Ackermann M., et al., 2010, *ApJ*, 717, L71  
Ackermann M., et al., 2016, *ApJ*, 819, 149  
Akamatsu H., Kawahara H., 2013, *PASJ*, 65, 16  
Akamatsu H., et al., 2015, *A&A*, 582, A87  
Akamatsu H., et al., 2017, *A&A*, 600, A100  
Andrade-Santos F., Bogdán Á., Romani R. W., Forman W. R., Jones C., Murray S. S., Taylor G. B., Zavala R. T., 2016, *ApJ*, 826, 91  
Andrade-Santos F., et al., 2017, *ApJ*, 843, 76  
Baars J. W. M., Genzel R., Pauliny-Toth I. I. K., Witzel A., 1977, *A&A*, 61, 99  
Bagchi J., Enßlin T. A., Miniati F., Stalin C., Singh M., Raychaudhury S., Humeshkar N., 2002, *New Astron.*, 7, 249  
Balogh M. L., Couch W. J., Smail I., Bower R. G., Glazebrook K., 2002, *MNRAS*, 335, 10  
Barrena R., Girardi M., Boschini W., Dasi M., 2009, *A&A*, 503, 357  
Bell A. R., R. A., 1978, *MNRAS*, 182, 147  
Bhatnagar S., Cornwell T. J., Golap K., Uson J. M., 2008, *A&A*, 487, 419  
Blandford R., Eichler D., 1987, *Phys. Rep.*, 154, 1  
Blasi P., Colafrancesco S., 1999, *Astropart. Phys.*, 12, 169  
Bonafede A., Giovannini G., Feretti L., Govoni F., Murgia M., 2009, *A&A*, 494, 429  
Bonafede A., et al., 2012, *MNRAS*, 426, 40  
Bonafede A., et al., 2014, *ApJ*, 785, 1  
Bonafede A., et al., 2017, *MNRAS*, 470, 3465  
Botteon A., Gastaldello F., Brunetti G., Dallacasa D., 2016a, *Mon. Not. R. Astron. Soc. Lett.*, 460, L84  
Botteon A., Gastaldello F., Brunetti G., Kale R., 2016b, *MNRAS*, 463, 1534  
Botteon A., Gastaldello F., Brunetti G., 2018, *MNRAS*, 476, 5591  
Brentjens M. a., de Bruyn a. G., 2005, *A&A*, 441, 1217  
Briggs D., 1995, PhD thesis, The New Mexico Institute of Mining and Technology, [www.atnf.csiro.au/people/tim.cornwell/research/danthesis.pdf](http://www.atnf.csiro.au/people/tim.cornwell/research/danthesis.pdf)  
Brown S., Rudnick L., 2011, *MNRAS*, 412, 2

- Brown S., Duesterhoeft J., Rudnick L., 2011a, *ApJ*, 727, L25
- Brown S., Emerick A., Rudnick L., Brunetti G., 2011b, *Astrophys. J. Lett.*, 740, 1
- Bruggen M., Bykov A., Ryu D., Rottgering H., Brügger M., Bykov A., Ryu D., Röttgering H., 2012, *Space Sci. Rev.*, 166, 187
- Brunetti G., 2004, *J. Korean Astron. Soc.*, 37, 493
- Brunetti G., Blasi P., 2005, *MNRAS*, 363, 1173
- Brunetti G., Jones T. W., 2014, *Int. J. Mod. Phys. D*, 23, 1430007
- Brunetti G., Lazarian A., 2007, *MNRAS*, 378, 245
- Brunetti G., Lazarian a., 2011a, *MNRAS*, 410, 127
- Brunetti G., Lazarian A., 2011b, *MNRAS*, 412, 817
- Brunetti G., Lazarian A., 2016, *MNRAS*, 458, 2584
- Brunetti G., Setti G., Feretti L., Giovannini G., 2001, *MNRAS*, 320, 365
- Brunetti G., Blasi P., Cassano R., Gabici S., 2004, *MNRAS*, 350, 1174
- Brunetti G., Venturi T., Dallacasa D., Cassano R., Dolag K., Giacintucci S., Setti G., 2007, *ApJ*, 670, L5
- Brunetti G., et al., 2008, *Nature*, 455, 944
- Brunetti G., Cassano R., Dolag K., Setti G., 2009, *A&A*, 669, 661
- Brunetti G., Blasi P., Reimer O., Rudnick L., Bonafede A., Brown S., 2012, *MNRAS*, 426, 956
- Brunetti G., Zimmer S., Zandanel F., 2017, *MNRAS*, 472, 1506
- Canning R. E. A., et al., 2012, *MNRAS*, 420, 2956
- Cassano R., Brunetti G., 2005, *MNRAS*, 357, 1313
- Cassano R., Brunetti G., Setti G., 2006, *MNRAS*, 369, 1577
- Cassano R., Brunetti G., Setti G., Govoni F., Dolag K., 2007, *MNRAS*, 378, 1565
- Cassano R., Gitti M., Brunetti G., 2008, *A&A*, 486, L31
- Cassano R., Brunetti G., Rottgering H. J. A., Bruggen M., 2010, *A&A*, 509, 68
- Cassano R., et al., 2013, *ApJ*, 777, 141
- Cayatte V., Balkowski C., van Gorkom J. H., Kotanyi C., 1990, *Astron. J.*, 100, 604
- Chandra P., Ray A., Bhatnagar S., 2004, *ApJ*, 612, 974
- Clarke T. E., Kronberg P. P., Böhringer H., 2001, *ApJ*, 547, L111
- Coleman J. E., et al., 2017, *MNRAS*, 464, 2469
- Cornwell T. J., 2008, *IEEE J. Sel. Top. Signal Process.*, 2, 793
- Cornwell T., Golap K., Bhatnagar S., 2005, in Shopbell P., Britton M., Ebert R., eds, *Astronomical Society of the Pacific Conference Series Vol. 347, Astron. Data Anal. Softw. Syst. XIV*. p. 86
- Cornwell T. J., Golap K., Bhatnagar S., 2008, *IEEE J. Sel. Top. Signal Process.*, 2, 647
- Cotton W. D., Condon J. J., Perley R. A., Kassim N., Lazio J., Cohen A., Lane W., Erickson W. C., 2004, in Oschmann, Jr. J. M., ed., *\procspie Vol. 5489, Ground-based Telesc.. International Society for Optics and Photonics*, p. 180, doi:10.1117/12.551298, <http://proceedings.spiedigitallibrary.org/>

- proceeding.aspx?doi=10.1117/12.551298
- Cuciti V., Cassano R., Brunetti G., Dallacasa D., Kale R., Etori S., Venturi T., 2015, *A&A*, 580, A97
- Dasadia S., et al., 2016, *ApJ*, 820, L20
- Dawson W. a. W., et al., 2015, *ApJ*, 805, 143
- Dennison B., 1980, *ApJ*, 239, L93
- Dolag K., Ensslin T. A., 2000, *A&A*, 157, 151
- Donnert J., Dolag K., Brunetti G., Cassano R., 2013, *MNRAS*, 429, 3564
- Donnert J. M. F., Stroe A., Brunetti G., Hoang D., Roettgering H., 2016, *MNRAS*, 462, 2014
- Dressler A., 1980, *ApJ*, 236, 351
- Drury L. O., O'C Drury L., 1983, *Reports Prog. Phys.*, 46, 973
- Eckert D., Molendi S., Paltani S., 2011, *A&A*, 526, A79
- Eckert D., Jauzac M., Vazza F., Owers M. S., Kneib J.-P. P., Tchernin C., Intema H., Knowles K., 2016, *MNRAS*, 461, 1302
- Enßlin T. A., Gopal-Krishna 2001, *A&A*, 366, 26
- Enßlin T. A., Biermann P. L. P., Klein U., Kohle S., Ensslin T. T. A., Biermann P. L. P., Klein U., Kohle S., 1998, *A&A*, 409, 395
- Enßlin T., Pfrommer C., Miniati F., Subramanian K., 2011, *A&A*, 527, A99
- Feretti L., Fusco-Femiano R., Giovannini G., Govoni F., 2001, *A&A*, 373, 106
- Feretti L., Orru E., Brunetti G., Giovannini G., Kassim N., Setti G., 2004, *A&A*, 423, 111
- Feretti L., Giovannini G., Govoni F., Murgia M., 2012, *Astron. Astrophys. Rev.*, 20, 54
- Ferrari C., Govoni F., Schindler S., Bykov a. M., Rephaeli Y., 2008, *Space Sci. Rev.*, 134, 93
- Finner K., et al., 2017, *ApJ*, 851, 46
- Finoguenov A., Sarazin C. L., Nakazawa K., Wik D. R., Clarke T. E., 2010, *ApJ*, 715, 1143
- Fixsen D. J., Wilkinson T., Anisotropy M., Wmap P., 2009, *ApJ*, 707, 916
- Fujita Y., Takizawa M., Sarazin C. L., 2003, *ApJ*, 584, 190
- Fujita Y., Matsumoto T., Wada K., 2004, *ApJ*, 612, L9
- Fumagalli M., Fossati M., Hau G. K., Gavazzi G., Bower R., Sun M., Boselli A., 2014, *MNRAS*, 445, 4335
- Gavazzi G., Boselli A., Mayer L., Iglesias-Paramo J., Vílchez J. M., Carrasco L., 2001, *ApJ*, 563, L23
- Giacintucci S., et al., 2008, *A&A*, 486, 347
- Ginzburg V., Syrovatskii S., 1969, *The origin of cosmic rays*. New York: Gordon and Breach
- Giovannini G., Tordi M., Feretti L., 1999, *New Astron.*, 4, 141
- Giovannini G., Bonafede A., Feretti L., Govoni F., Murgia M., 2010, *A&A*, 511, L5

- Girardi M., Barrena R., Boschin W., Ellingson E., 2008, *A&A*, 491, 379
- Gitti M., Brunetti G., Setti G., 2002, *A&A*, 386, 456
- Gizani N. A. B., Cohen A., Kassim N. E., 2005, *MNRAS*, 358, 1061
- Golovich N., et al., 2017a, arXiv:1711.01347v1
- Golovich N., et al., 2017b, *ApJ*, 838, 110
- Goto T., Yamauchi C., Fujita Y., Okamura S., Sekiguchi M., Smail I., Bernardi M., Gomez P. L., 2003, *MNRAS*, 346, 601
- Govoni F., Feretti L., 2004, *Int. J. Mod. Phys. D*, 13, 1549
- Govoni F., Enßlin T. A., Feretti L., Giovannini G., 2001a, *A&A*, 369, 441
- Govoni F., Feretti L., Giovannini G., Böhringer H., Reiprich T. H., Murgia M., 2001b, *A&A*, 819, 803
- Gunn J. E., Gott, J. Richard I., 1972, *ApJ*, 176, 1
- Guth A. H., 1981, *Phys. Rev. D*, 23, 347
- Ha J.-h., Ryu D., Kang H., 2018, *ApJ*, 857, 26
- Haarlem M. P. V., et al., 2013, *A&A*, 2, 1
- Harwood J. J., Hardcastle M. J., Croston J. H., Goodger J. L., 2013, *MNRAS*, 435, 3353
- Harwood J. J., Hardcastle M. J., Croston J. H., 2015, *MNRAS*, 454, 3403
- Hindson L., et al., 2014, *MNRAS*, 445, 330
- Hlavacek-Larrondo J., et al., 2018, *MNRAS*, 475, 2743
- Hoang D. N., et al., 2017, *MNRAS*, 471, 1107
- Hoang D. N., et al., 2018a, *MNRAS*, 478, 2218
- Hoang D. N., Shimwell T. W., van Weeren R. J., Brunetti G., Röttgering H. J. A., Andrade-Santos F., 2018b, *A&A*, 500, 1
- Hoang D. N., et al., 2018c, *A&A*, 600, 0
- Hoefl M., Brüggen M., Brügger M., 2007, *MNRAS*, 375, 77
- Hoefl M., Brügger M., Yepes G., Gottlöber S., Schwobe A., 2008, *MNRAS*, 391, 1511
- Hoefl M., et al., 2011, *J. Astrophys. Astron.*, 32, 509
- Hogan M. T., et al., 2015, *MNRAS*, 453, 1201
- Hong S. E., Kang H., Ryu D., 2015, *ApJ*, 812, 49
- Iapichino L., Niemeyer J. C., 2008, *MNRAS*, 388, 1089
- Iapichino L., Adamek J., Schmidt W., Niemeyer J. C., 2008, *MNRAS*, 388, 1079
- Iapichino L., Schmidt W., Niemeyer J. C., Merklein J., 2011, *MNRAS*, 414, 2297
- Intema H. T., van der Tol S., Cotton W. D., Cohen A. S., van Bemmell I. M., Röttgering H. J. A., Röttgering H. J. A., 2009, *A&A*, 501, 1185
- Intema H. T., Jagannathan P., Mooley K. P., Frail D. A., 2017, *A&A*, 598, A78
- Itahana M., Takizawa M., Akamatsu H., Ohashi T., Ishisaki Y., Kawahara H., van Weeren R. J., 2015, *Publ. Astron. Soc. Japan*, 67, 113
- Jaffe W. J., 1977, *ApJ*, 212, 1
- Jee M. J., Mahdavi A., Hoekstra H., Babul A., Dalcanton J. J., Carroll P., Capak P., 2012, *ApJ*, 747, 96

- Jee M. J., et al., 2015, *ApJ*, 802, 46
- Jee M. J., Dawson W. W. A., Stroe A., Wittman D., van Weeren R. J. R., Brüggem M., Bradač M., Röttgering H., 2016, *ApJ*, 817, 179
- Jeltema T. E., Profumo S., 2011, *ApJ*, 728, 53
- Jeltema T. E., Kehayias J., Profumo S., 2009, *Phys. Rev. D - Part. Fields, Gravit. Cosmol.*, 80, 1
- Johnston S., 2007, *Publ. Astron. Soc. Aust.*, pp 1–14
- Kale R., Dwarakanath K. S., Bagchi J., Paul S., 2012, *MNRAS*, 426, 1204
- Kang H., 2015a, *J. Korean Astron. Soc.*, 48, 9
- Kang H., 2015b, *J. Korean Astron. Soc.*, 48, 155
- Kang H., Ryu D., 2011, *ApJ*, 734, 18
- Kang H., Ryu D., 2016, *ApJ*, 823, 13
- Kang H., Ryu D., Jones T. W., 2012, *ApJ*, 756, 97
- Kazemi S., Yatawatta S., Zaroubi S., Lampropoulos P., de Bruyn A. G., Koopmans L. V., Noordam J., 2011, *MNRAS*, 414, 1656
- Kempner J. C., Sarazin C. L., 2001, *ApJ*, 548, 639
- Kempner J., Blanton E., Clarke T., Enßlin T., Johnston-Hollitt M., Rudnick L., 2004, in Reiprich T., Kempner J., Soker N., eds, *Riddle Cool. Flows Galaxies Clust. galaxies*.
- Keshet U., Loeb A., 2010, *ApJ*, 722, 737
- Kierdorf M., Beck R., Hoeft M., Klein U., van Weeren R., Forman W., Jones C., 2017, *A&A*, 600, A18
- King L. J., et al., 2016, *MNRAS*, 459, 517
- Kocevski D. D., Ebeling H., Mullis C. R., Tully R. B., 2007, *ApJ*, 662, 224
- Kodama T., Balogh M. L., Smail I., Bower R. G., Nakata F., 2004, A panoramic  $H\alpha$  imaging survey of the  $z = 0.4$  cluster C10024.0+1652 with Subaru (arXiv:0408037), doi:10.1111/j.1365-2966.2004.08271.x, <https://academic.oup.com/mnras/article-lookup/doi/10.1111/j.1365-2966.2004.08271.x>
- Kolb E. W., Turner M. S., Silk J., 1991, *Phys. Today*, 44, 106
- Landau L., Lifshitz E., 1959, *Fluid mechanics*. London: Pergamon Press
- Lane W. M., Kassim N. E., Ensslin T. A., Harris D. E., Perley R. A., 2002, *ApJ*, 123, 2985
- Larson R. B., Tinsley B. M., Caldwell C. N., 1980, *ApJ*, 237, 692
- Liang H., Hunstead R. W., Birkinshaw M., Andreani P., 2000, *ApJ*, 544, 686
- Lonsdale C., et al., 2009, *Proc. IEEE*, 97, 1497
- Macario G., Markevitch M., Giacintucci S., Brunetti G., Venturi T., Murray S. S., 2011, *ApJ*, 728, 82
- Mahdavi A., Hoekstra H., Babul A., Balam D. D., Capak P. L., 2007, *ApJ*, 668, 806
- Markevitch M., 2010, Twelfth Marcel Grossmann Meet. *Gen. Relativ.*, p. 14
- Markevitch M., Vikhlinin A., 2007, *Phys. Rep.*, 443, 1
- Markevitch M., Gonzalez A. H., David L., Vikhlinin A., Murray S., Forman W.,

- Jones C., Tucker W., 2002, *ApJ*, 567, L27
- Markevitch M., Govoni F., Brunetti G., Jerius D., 2005, *ApJ*, 627, 733
- McMullin J., Waters B., Schiebel D., Young W., Golap K., 2007, in Shaw R., Hill F., Bell D., eds, *Astronomical Society of the Pacific Conference Series Vol. 376*, *Astron. Data Anal. Softw. Syst. XVI*. p. 127
- Miley G., 1980, *Annu. Rev. Astron. Astrophys.*, 18, 165
- Miley G., Perola G., van der Kruit P., van der Laan H., 1972, *Nature*, 237, 269
- Miniati F., 2014, *ApJ*, 782, 21
- Miniati F., 2015, *ApJ*, 800, 60
- Miniati F., Jones T. W., Kang H., Ryu D., 2001, *ApJ*, 562, 233
- Moore B., Katz N., Lake G., Dressler A., Oemler A., 1996, *Nature*, 379, 613
- Moore B., Lake G., Katz N., 1998, *ApJ*, 495, 139
- Murgia M., Govoni F., Markevitch M., Feretti L., Giovannini G., Taylor G. B., Carretti E., 2009, *A&A*, 499, 679
- Norris R. P., et al., 2017, *Publ. Astron. Soc. Aust.*, 28, 215
- Nuza S. E., Gelszinnis J., Hoeft M., Yepes G., 2017, *MNRAS*, 470, 240
- Offringa R., Smirnov O., 2017, *MNRAS*, 16, 1
- Offringa A. R., van de Gronde J. J., Roerdink J. B. T. M., 2012, *A&A*, 539, A95
- Offringa A. R., et al., 2014, *MNRAS*, 444, 606
- Ogrean G. a., et al., 2013a, *MNRAS*, 429, 2617
- Ogrean G. A., Brüggem M., van Weeren R. J., Röttgering H., Croston J. H., Hoeft M., 2013b, *MNRAS*, 433, 812
- Ogrean G. a., et al., 2014a, *MNRAS*, 440, 3416
- Ogrean G. A., et al., 2014b, *MNRAS*, 443, 2463
- Okabe N., Akamatsu H., Kakuwa J., Fujita Y., Zhang Y. Y.-Y., Tanaka M., Umetsu K., 2015, *Publ. Astron. Soc. Japan*, 67, 1
- Oosterloo T., van Gorkom J., 2005, *A&A*, 437, L19
- Oppermann N., et al., 2012, *A&A*, 542, A93
- Orrù E., Murgia M., Feretti L., Govoni F., Brunetti G., Giovannini G., Girardi M., Setti G., 2007, *A&A*, 467, 943
- Pandey V. N., Zwieten J. E. V., Bruyn A. G. D., Nijboer R., 2009, "The Low-Frequency Radio Universe", *ASP Conf. Ser.*, 407, 384
- Pearce C. J. J., et al., 2017, *ApJ*, 845, 81
- Pearson T. J., Readhead A. C. S., 1984, *Annu. Rev. Astron. Astrophys.*, 22, 97
- Perley R. A., Butler B. J., 2013, *Astrophys. J. Suppl. Ser.*, 204, 19
- Petrosian V., 2001, *ApJ*, 557, 560
- Pfrommer C., 2008, *MNRAS*, 385, 1242
- Pfrommer C., Enßlin T. A., 2004, *MNRAS*, 352, 76
- Pfrommer C., Springel V., Ensslin T. A., Jubelgas M., 2006, *MNRAS*, 367, 113
- Pinzke A., Oh S. P., Pfrommer C., 2013, *MNRAS*, 435, 1061
- Pinzke A., Oh S. P., Pfrommer C., 2017, *MNRAS*, 465, 4800
- Planck Collaboration et al., 2016, *A&A*, 594, A27

- Planck Collaboration et al., 2018, *Astron. Astrophys. Suppl. Ser.*, pp 1–71
- Proust D., Cuevas H., Capelato H. V., Sodréjr L., Omé Lehodey B. T., Le Evre O., Mazure A., 2000, *A&A*, 355, 443
- Rajpurohit K., et al., 2018, *ApJ*, 852, 65
- Rau U., Cornwell T. J., 2011, *A&A*, 532, A71
- Rich J. W., de Blok W. J. G., Cornwell T. J., Brinks E., Walter F., Bagetakos I., Kennicutt R. C., 2008, *ApJ*, 136, 2897
- Rodríguez-Gonzálvez C., et al., 2011, *MNRAS*, 414, 3751
- Roettiger K., Burns J. O., Stone J. M., 1999, *ApJ*, 518, 603
- Rossetti M., Eckert D., Cavalleri B. M., Molendi S., Gastaldello F., Ghizzardi S., 2011, *A&A*, 532, A123
- Röttgering H., et al., 2011, *J. Astrophys. Astron.*, 32, 557
- Russell H. R., Sanders J. S., Fabian A. C., Baum S. A., Donahue M., Edge A. C., McNamara B. R., O’Dea C. P., 2010, *MNRAS*, 406, 1721
- Russell H. R., et al., 2011, *Mon. Not. R. Astron. Soc. Lett.*, 417, L1
- Russell H. R., et al., 2012, *MNRAS*, 423, 236
- Ryu D., Kang H., Hallman E., Jones T., 2003, *ApJ*, 593, 599
- Sarazin C. C. L., 2002, in Feretti L., Gioia I., Giovannini G., eds, *Astrophysics and Space Science Library Vol. 272, Merging Process. Galaxy Clust.* Springer Netherlands, Dordrecht, pp 1–38
- Scaife A. M. M., Heald G. H., 2012, *Mon. Not. R. Astron. Soc. Lett.*, 423, 30
- Schilizzi R. T., 2005, in Gurvits L., Frey S., Rawlings S., eds, *EAS Publications Series Vol. 15, EAS Publ. Ser.* pp 445–463, doi:10.1051/eas:2005170, <http://www.eas-journal.org/10.1051/eas:2005170>
- Shimwell T. W., Brown S., Feain I. J., Feretti L., Gaensler B. M., Lage C., 2014, *MNRAS*, 440, 2901
- Shimwell T. W., Markevitch M., Brown S., Feretti L., Gaensler B. M., Johnston-Hollitt M., Lage C., Srinivasan R., 2015, *MNRAS*, 449, 1486
- Shimwell T. W., et al., 2016, *MNRAS*, 459, 277
- Shimwell T. W., et al., 2017, *A&A*, 598, A104
- Skillman S. W., Hallman E. J., O’Shea B. W., Burns J. O., Smith B. D., Turk M. J., 2011, *ApJ*, 735, 96
- Skillman S. W., Xu H., Hallman E. J., O’Shea B. W., Burns J. O., Li H., Collins D. C., Norman M. L., 2013, *ApJ*, 765, 21
- Smoot G. F., et al., 1992, *ApJ*, 396, L1
- Steinhauser D., Haider M., Kapferer W., Schindler S., 2012, *A&A*, 544, A54
- Stroe A., van Weeren R. J., Intema H. T., Röttgering H. J. A., Brügggen M., Hoeft M., J V. W. R., 2013, *A&A*, 555, A110
- Stroe A., Harwood J. J., Hardcastle M. J., Röttgering H. J. A., 2014, *MNRAS*, 445, 1213
- Stroe A., et al., 2015a, *MNRAS*, 450, 646
- Stroe A., et al., 2015b, *MNRAS*, 455, 2402



- Swarup G., Ananthkrishnan S., Kapahi V., Rao A., Subrahmanya C., Kulkarni V., 1991, *Curr. Sci.*, 60, 95
- Takizawa M., 2005, *ApJ*, 629, 791
- Tasse C., et al., 2012, *A&A*, 553, 13
- Taylor G. B., 2006, *Proc. Int. Astron. Union*, 2, 388
- Thierbach M., Klein U., Wielebinski R., 2003, *A&A*, 397, 53
- Trasatti M., Akamatsu H., Lovisari L., Klein U., Bonafede A., Bruggen M., Dallacasa D., Clarke T., 2015, *A&A*, 575, A45
- Urdampilleta I., Akamatsu H., Mernier F., Kaastra J. S., de Plaa J., Ohashi T., Ishisaki Y., Kawahara H., 2018, *A&A*, 5301, 1
- Vacca V., Feretti L., Giovannini G., Govoni F., Murgia M., Perley R. A., Clarke T. E., 2014, *A&A*, 52, A52
- Vazza F., Brunetti G., Kritsuk A., Wagner R., Gheller C., Norman M., 2009, *A&A*, 504, 33
- Vazza F., Brüggen M., van Weeren R., Bonafede A., Dolag K., Brunetti G., 2012, *MNRAS*, 421, 1868
- Vazza F., Eckert D., Brüggen M., Huber B., Bruggen M., Huber B., 2015, *MNRAS*, 451, 2198
- Vazza F., Jones T. W., Brüggen M., Brunetti G., Gheller C., Porter D., Ryu D., 2017, *MNRAS*, 464, 210
- Venturi T., Giacintucci S., Dallacasa D., Cassano R., Brunetti G., Bardelli S., Setti G., 2008, *A&A*, 484, 327
- Venturi T., Giacintucci S., Dallacasa D., Cassano R., Brunetti G., Macario G., Athreya R., 2013, *A&A*, 551, A24
- Vikhlinin A., Markevitch M., Murray S., Jones C., Forman W., Van Speybroeck L., 2005, *ApJ*, 628, 655
- Wang Q. H. S., Markevitch M., Giacintucci S., Wang Q. H. S., Markevitch M., Giacintucci S., 2016, *ApJ*, 833, 99
- Wang Q. H. S., Giacintucci S., Markevitch M., 2018, *ApJ*, 856, 162
- White J. A., et al., 2015, *MNRAS*, 453, 2718
- Williams W. L., et al., 2016, *MNRAS*, 460, 2385
- Yatawatta S., et al., 2013, *A&A*, 550, A136
- Yuan Z. S., et al., 2015, *ApJ*, 813, 77
- Zandanel F., Ando S., 2014, *MNRAS*, 440, 663
- Zandanel F., Pfrommer C., Prada F., 2014, *MNRAS*, 438, 124
- ZuHone J. a., Markevitch M., Brunetti G., Giacintucci S., 2013, *ApJ*, 762, 78
- de Gasperin F., van Weeren R. J., Bruggen M., Vazza F., Bonafede A., Intema H. T., 2014, *MNRAS*, 444, 3130
- de Gasperin F., Intema H. T., van Weeren R. J., Dawson W. A., Golovich N., Wittman D., Bonafede A., Brüggen M., 2015, *MNRAS*, 453, 3484
- de Gasperin F., et al., 2018, *A&A*
- van Weeren R. J., Rottgering H. J. A., Bruggen M., Cohen A., Röttgering H. J. A.,

- Brüggen M., Cohen A., 2009, *A&A*, 505, 991
- van Weeren R. J., Rottgering H. J. A., Brüggen M., Hoeft M., 2010, *Science*, 330, 347
- van Weeren R. J., Brüggen M., Röttgering H. J. A., Hoeft M., 2011a, *MNRAS*, 418, 230
- van Weeren R. J., Hoeft M., Rottgering H. J. A., Brüggen M., Intema H. T., van Velzen S., 2011b, *A&A*, 528, A38
- van Weeren R. J., et al., 2013, *ApJ*, 769, 101
- van Weeren R. J., et al., 2016a, *Astrophys. J. Suppl. Ser.*, 223, 2
- van Weeren R. J., et al., 2016b, *ApJ*, 817, 98
- van Weeren R. J., et al., 2016c, *ApJ*, 818, 204
- van Weeren R. J., et al., 2017, *Nat. Astron.*, 1, 5
- van der Tol S., Jeffs B., van der Veen A.-J., 2007, *IEEE Trans. Signal Process.*, 55, 4497



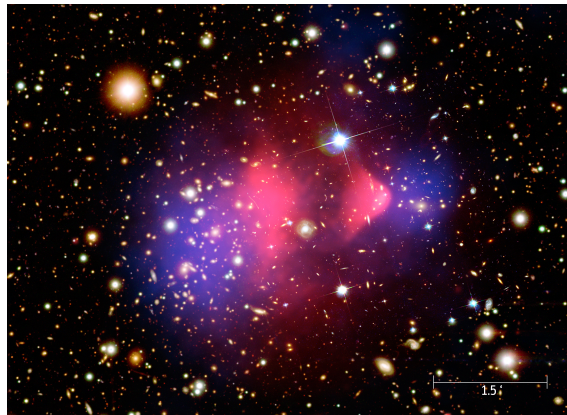
## Nederlandse samenvatting

Clusters van sterrenstelsels zijn de grootste structuren in het heelal die door zwaartekracht bijeen worden gehouden. Zij bestaan uit honderden tot duizenden sterrenstelsels binnen een volume van maximaal  $\sim 100 \text{ Mpc}^3$  (zie bv. figuur 5.7). Clusters bestaan uit donkere materie ( $\sim 80 \%$  van de totale massa), uit zeer heet plasma ( $\sim 16 \%$ ) van het zogenaamde intra-cluster medium (ICM), en uit baryonisch materiaal in sterren, koud gas en stof ( $\sim 4 \%$ ). Binnen het raamwerk van hiërarchische vorming van structuur in het heelal groeien clusters middels een opeenvolging van samensmeltingen van kleinere clusters en groepen (zie bv. Sarazin 2002) of door continue inval van materie langs intergalactische filamenten (zie bv. Bagchi et al. 2002; Giovannini et al. 2010). Samensmeltingen van massieve clusters zijn de meest energetische gebeurtenissen in het heelal sinds de oerknal, waarbij tot  $\sim 10^{64}$  ergs aan energie in het ICM wordt gedeponneerd op tijdschalen van enkele miljarden jaren. Deze energie verhit het ICM tot dusdanig hoge temperaturen ( $\sim 10 \text{ keV}$ ) dat het Röntgenstraling gaat uitzenden. Het samensmelten genereert schokgolven en turbulentie in het ICM, wat leidt tot de (hernieuwde) versnelling van deeltjes tot relativistische snelheden. In de aanwezigheid van magneetvelden ( $\sim \mu\text{G}$ ) zenden deze relativistische deeltjes synchrotronstraling uit die kan worden gedetecteerd met radio telescopen.

Via waarnemingen zijn inmiddels vele uitgestrekte radiobronnen gedetecteerd in het centrum en in de buitenste regio's van clusters van sterrenstelsels (zie bv. recente reviews van Govoni & Feretti 2004; Feretti et al. 2012; Brunetti & Jones 2014). Deze uitgestrekte bronnen vertonen geen duidelijke samenhang met individuele sterrenstelsels, maar zijn gerelateerd aan de niet-thermische componenten (de relativistische deeltjes en het magneetveld) in het ICM. De uitgestrekte synchrotron-bronnen vertonen een lage oppervlakte-helderheid ( $\sim \mu\text{Jy arcsec}^{-2}$  op 1.4 GHz) en een steil spectrum<sup>4</sup>

---

<sup>4</sup> $S \propto \nu^\alpha$



Figuur 5.7: Samengestelde afbeelding van de zogenaamde Bullet cluster: optische HST (Hubble Space Telescope) afbeelding met Röntgenstraling in roze (Chandra) en de massaverdeling afgeleid uit zogenaamde weak-lensing waarnemingen in blauw (Image credit: NASA/CXC/M. Weiss)

( $\alpha \lesssim -1$ ). Afhankelijk van hun eigenschappen (morphologie, locatie ten opzichte van het cluster centrum, polarisatie, spectrum) zijn de uitgestrekte bronnen geclassificeerd als radio halo's, mini-halo's of relics.

### Radio halo's

Radio halo's zijn uitgestrekte ( $\sim$  Mpc), niet-gepolariseerde steil-spectrum bronnen die worden waargenomen in het centrum van samensmelgende clusters van sterrenstelsels. De belangrijkste huidige modellen zijn:

- het primaire model welke stelt dat relativistische elektronen worden opgewekt door Fermi-II turbulente her-acceleratie gedurende de samsmsmelting (zie bv. Brunetti et al. 2001; Petrosian 2001; Fujita et al. 2003; Cassano & Brunetti 2005; Brunetti & Lazarian 2007, 2016; Pinzke et al. 2017)
- het secundaire model welke stelt dat relativistische elektronen in radio halo's een secundair product zijn van hadronische botsingen tussen relativistische protonen en thermische protonen in het ICM (zie bv. Dennison 1980; Blasi & Colafrancesco 1999; Dolag & Ensslin 2000; Miniati et al. 2001; Pfrommer & Enßlin 2004; Pfrommer 2008; Keshet & Loeb 2010; Enßlin et al. 2011).

## Radio relics

Radio relics zijn uitgestrekte ( $\sim$  Mpc), langwerpige, sterk-gepolariseerde steil-spectrum bronnen die normaliter worden waargenomen in de buitenste regio's van clusters van sterrenstelsels. Voor radio relics wordt aangenomen dat zij gekoppeld zijn aan schokgolven die worden opgewekt door samensmeltingen van clusters, of door invallend gas langs intergalactische filamenten (zie bv. Enßlin et al. 1998; Brown & Rudnick 2011).

## Dit proefschrift

De doelstellingen van dit proefschrift zijn (i) het karakteriseren van de eigenschappen van radio halo's en relics in samensmeltende clusters van sterrenstelsels, (ii) het beter begrijpen van de processen die verantwoordelijk zijn voor het versnellen van deeltjes in deze bronnen, en (iii) het verkrijgen van een gedetailleerd beeld van de dynamische toestand van de clusters van sterrenstelsels waarin deze bronnen voorkomen. De bestudeerde clusters zijn CIZA J2242.8+5301 (de zogenoemde 'Sausage' cluster), Abell 1240, Abell 520 en Abell 2146.

In hoofdstuk 2 worden nieuwe LOFAR waarnemingen op 145 MHz gepresenteerd van de prominente 'Sausage' cluster (roodverschuiving  $z = 0.192$ ). Er wordt ook gebruik gemaakt van gearchiveerde radio telescoop-waarnemingen van GMRT, WSRT, VLA, Chandra en Suzaku. Deze studie toont aan dat (i) de vorm en spectrale eigenschappen van de noordelijke en zuidelijke relics consistent zijn met het paradigma dat relics geassocieerd zijn met schokgolven door samensmeltingen, wat in overeenstemming is met andere studies (van Weeren et al. 2010; Stroe et al. 2013); (ii) de onder de aanname van diffuse schok-versnelling (DSA) afgeleide Mach-getallen uit de radiowaarnemingen consistent zijn met Mach-getallen afgeleid uit Röntgen-waarnemingen (Akamatsu et al. 2015), wat pleit voor het schok-versnelling scenario van relics; (iii) de oppervlakte-helderheid van radio-emissie in de noordelijke relic kan worden verklaard door DSA van fossiele elektronen middels het Fermi-I proces, maar directe versnelling van thermische elektronen kan op basis van de gevoeligheid van de huidige data niet worden uitgesloten; (iv) het radiospectrum van de halo constant is over de gehele regio tussen noordelijke en zuidelijke relic, wat de aanwezigheid impliceert van een groot turbulent gebied veroorzaakt door de samensmelting.

Hoofdstuk 3 presenteert een radio-studie van het cluster Abell 1240 ( $z = 0.1948$ ) met twee relics, gebruikmakend van LOFAR 143 MHz, GMRT

612 MHz en VLA 3 GHz waarnemingen. Deze studie bevestigt dat het spectrum van de relics steiler wordt richting het cluster centrum, en dat de uit de polarisatie afgeleide richting van het magneet veld in de relics grotendeels haaks staat op de lengte-as van de relics, wat beide in overeenstemming is met de studie van Bonafede et al. (2009). De spectrale- en polarisatie-eigenschappen van de relics zijn consistent met het scenario waarin deeltjes die radiostraling afgeven in de relics worden versneld door schokgolven die slechts marginaal worden gedetecteerd in Chandra Röntgenwaarnemingen.

In hoofdstuk 4 worden de versnellings-mechanismes bestudeerd die aanleiding geven tot de vorming van uitgestrekte radiobronnen in samensmelend cluster Abell 520 ( $z = 0.201$ ) middels waarnemingen van LOFAR op 145 MHz, GMRT op 323 MHz en VLA op 1.5 GHz. Het zuidwestelijke deel van de uitgestrekte radiobronnen valt ongeveer samen met een boeg-schok waargenomen in Röntgenstraling, en lijkt daardoor met de schok samen te hangen. Er is ook een toename in de steilheid van het radiospectrum achter de schok. Dit impliceert dat de uitgestrekte radiobronnen een superpositie zijn van een centrale radio halo en een radio relic in het zuidwesten. DSA zou het mechanisme kunnen zijn waarmee relativistische elektronen worden versneld bij de schok. Omdat er geen uitgestrekte radiobron aan de voorkant van de schok is gevonden, is het onwaarschijnlijk dat compressie van het magneetveld verantwoordelijk is voor deeltjesversnelling.

Hoofdstuk 5 beschrijft een studie van de samensmelende cluster Abell 2146 ( $z = 0.232$ ), gebruikmakend van nieuwe radiowaarnemingen met LOFAR op 144 MHz, aangevuld met bestaande VLA 1.5 GHz waarnemingen. Deze waarnemingen bevestigen het bestaan van uitgestrekte radiobronnen ten noordwesten en zuidoosten van het cluster, gepositioneerd achter de schokgolven die zichtbaar zijn middels Röntgenstraling. LOFAR detecteert een brug van zwakke radiostraling tussen de eerder-genoemde radiobronnen die niet zichtbaar is met de VLA. Het spectrum van de radio-emissie in het noordwesten wordt steiler in de richting van het cluster centrum, maar is inconsistent met de waarden die het DSA model voorspelt. Dit verschil kan mogelijk worden verklaard door aan te nemen dat de versnelde elektronen reeds bestaande fossiele elektronen zijn in plaats van thermische elektronen. De zuidoostelijke rand van de daar gelegen radiobron volgt bij benadering de zuidoostelijke (Röntgen) boeg-schok, wat een verband tussen de twee impliceert. Onder aanname van DSA komen de Mach-getallen afgeleid uit radio- en Röntgenwaarnemingen overeen, wat het mogelijke verband nog versterkt. Toch is het nog onduidelijk of de uitgestrekte bron in het zuidoosten een radio halo is, of wellicht een superpositie van een halo en een

relic. In beide gevallen ligt de waarde van het totale vermogen van de radiostraling van de halo dichtbij de verwachte waarde voor een cluster met een massa gelijk aan dat van Abell 2146. Afsluitend, de aanwezigheid van de uitgestrekte radiobronnen in het noordwesten en zuidoosten van Abell 2146 kan het beste worden verklaard door de versnelling van fossiele elektronen (voor het gebied in het noordwesten) en thermische elektronen (voor het gebied in het zuidoosten) door schokgolven en turbulentie in een smelting van clusters.





## Curriculum Vitae

I was born on June 3, 1981 in Vietnam. When I was at high school, I realized that I was interested in doing a career in scientific research.

In 2003, I received my bachelor degree in chemistry from the University of Science - HoChiMinh City (US-HCMC). After graduation, I worked as a teaching assistant for laboratory courses on physical/computational chemistry at US-HCMC. I very much enjoyed doing chemistry experiments in the laboratory.

However, I was then more interested in physics and astronomy. In 2008, I decided to learn more about physics by attending a master program in physics at Stockholm University where I did my graduation thesis on theoretical quantum physics with my supervisor Prof. Hoshang Heydari. The thesis was about “geometrically controlled evolution of four-qubit states”.

After a short period of time working at International University - HoChiMinh City (VNU-HCMC-IU), I went to the Institute of Astronomy & Astrophysics, Academia Sinica (ASIAA) in Taiwan to learn about radio astronomy in 2012. At ASIAA, I joined the YTLA (Yuan-Tseh Lee Array, formerly AMiBA) group of Prof. Paul Ho. YTLA is a radio interferometer operating at 86 – 102 GHz and is built to observe the cosmic microwave background (CMB) radiation and the Sunyaev-Zel’dovich effect in galaxy clusters. In combination with radio observations at low frequency, the aim of my project was to search for the spatial correlation between the non-thermal (i.e. relativistic electrons, magnetic field) and thermal components in the intra-cluster medium (ICM).

In 2014, I was offered a PhD position in the group of Prof. Huub Röttgering at Leiden Observatory, Netherlands. My research focused on the particle acceleration mechanisms by large-scale shocks and turbulence in merging clusters of galaxies. To study the non-thermal components (i.e. relativistic electrons, magnetic field) in the ICM of merging galaxy clusters, I mainly used multi-frequency radio observations that were performed with the Low

Frequency Array (LOFAR), Karl G. Jansky Very Large Array (JVLA), Giant Metrewave Radio Telescope (GMRT), and Westerbork Synthesis Radio Telescope (WSRT). In addition, I also used X-ray data that were observed with X-ray satellites (i.e. Chandra, Suzaku). The results of my PhD research projects are presented in this thesis and are also published in international journals (i.e. Monthly Notices of the Royal Astronomical Society, *Astronomy & Astrophysics*). During my PhD study, I also attended/presented my research results at conferences in Beijing (China), Hamburg, Munich (Germany), Bologna (Italy), Assen, Dwingeloo, Leiden, Noordwijkerhout (Netherlands), Manchester (UK), California (US), and HoChiMinh (Vietnam).

After finishing my PhD study, I will move to Hamburg Observatory for a postdoctoral position in radio astronomy.

# List of publications

## First-author publications

1. Hoang, D. N. et al. Deep LOFAR observations of the merging galaxy cluster CIZA J2242.8+5301. 2017, MNRAS, 471, 1107 (Chapter 2)
2. Hoang, D. N. et al. Radio observations of the double-relic galaxy cluster Abell 1240. 2018, MNRAS, 478, 2218 (Chapter 3)
3. Hoang, D. N. et al. Radio observations of the merging galaxy cluster Abell 520. 2019, A&A, 622, A20 (Chapter 4)
4. Hoang, D. N. et al. Characterizing the radio emission from the binary galaxy cluster merger Abell 2146. 2019, A&A, 622, A21 (Chapter 5)

## Co-author publications

1. Shimwell, T. W. et al. (including Hoang, D. N.) The LOFAR Two-metre Sky Survey – II. First Data Release. 2019, A&A, 622, A1
2. Mandal, S. et al. (including Hoang, D. N.) Ultra steep spectrum emission in the merging galaxy cluster Abell 1914. 2019, A&A, 622, A22
3. Di Gennaro, G. et al. (including Hoang, D. N.) Deep Very Large Array observations of the merging cluster CIZA J2242.8+5301: Continuum and spectral imaging. 2018, ApJ, 865, 24
4. Botteon, A. et al. (including Hoang, D. N.) The spectacular cluster chain Abell 781 as observed with LOFAR, GMRT and XMM-Newton. 2019, ApJ, 622, A19

5. Botteon, A. et al. (including Hoang, D. N.) LOFAR discovery of a double radio halo system in Abell 1758 and radio/X-ray study of the cluster pair. 2018, MNRAS, 478, 885
6. Donnert, J. M. F. et al. (including Hoang, D.) Magnetic field Evolution in Giant Radio Relics using the example of CIZA J2242.8+530. 2016, MNRAS, 462, 204
7. Kai-Yang, L. et al. (including Hoang, D. N.) AMiBA: Cluster Sunyaev-Zel'dovich Effect Observations with the Expanded 13-element Array. 2016, ApJ, 830, 91
8. Shimwell, T. W. et al. (including Hoang, D. N.) The LOFAR Two-metre Sky Survey I. Survey description and preliminary data release. 2016, A&A, 598, A04
9. Shimwell, T. W. et al. (including Hoang, D. N.) A plethora of diffuse steep spectrum objects in Abell 204. 2015, MNRAS, 459, 277

## Acknowledgements

It has been wonderful years of my life working as a PhD student at Leiden Observatory in the little city of Leiden, Netherlands. I would not have become who I am today without the help and support of many people.

Special thanks to my supervisors Huub Röttgering, Timothy Shimwell, and Reinout van Weeren. Huub: Thank you for accepting me as one of your students, for giving me the freedom to choose my own research and for providing support/guidance during my PhD study. Tim: Thank you for being my daily supervisor and a friend of mine. You are always very nice and helpful. Reinout: Thank you very much for helping me from the beginning to the end of my PhD study. Working with you is always prolific and fun.

I would also like to thank former/current members of the Huub's group who I have been closely work with and learn a lot from. Many thanks to Andra (CfA), Julius (INAF-IRA), Huib (CIRA), Francesco (Universität Hamburg), Wendy, Jit, Josh, Gabriella, Raymond (ASTRON), Leah (University of Oxford), Edwin, and Pedro.

It was a great opportunity for me to work with people in the LOFAR collaboration as well as collaborators of collaborators. Thank you Gianfranco (INAF-IRA), Marcus (Universität Hamburg), Matthias (Thüringer Landessternwarte), Annalisa (INAF-IRA), Rossella (INAF-IRA), David (University of Manchester), David (Universität Hamburg), Andrea (INAF-IRA), Gabriella (CfA), Emanuela (ASTRON), Roberto (ASTRON), Glenn (The Open University), George, Chiara (CNRS), Krzysztof (Jagiellonian University), Torsten (Max Planck Institute for Astrophysics), Julie (Université de Montréal), and Marie-Lou (Université de Montréal).

Many thanks to the X-ray people (i) who helped me with X-ray aspects of the galaxy clusters: Hiroki (SRON), Liyi (SRON), and Felipe (CfA) and (ii) who organized regular seminars on cluster studies: Francois (MTA-Eötvös University) and Igone (SRON).

My PhD time would not be easy and pleasant without the help from the Sterrewacht and Leiden University staff. I would like to thank Alexandra, Els, Evelijn, Caroline, Marjan, Monica, Anita, Debbie, Liesbeth, David, Evdkraan, Erik, Kelly, Saskia, and Yvonne.

I would like to take this opportunity to thank my pre-doctoral supervisors for helping/guiding me through the initial steps of radio astronomy: Patrick (ASIAA) and Paul (ASIAA). Also thanks to anh Ngoc (a colleague of mine at VNU-HCMC-IU) for supporting me during this period of time.

This thesis is dedicated to my family, my father, my father-in-law, my mother, my mother-in-law, my brothers, my brother-in-law, my sisters, my sisters-in-law, and my beloved wife. Thank you very much for loving me unconditionally, always being supportive and believing in me. I always feel warm in my heart when thinking of you. Last but not least, lovely thanks to my wife, Ly, for always being by my side and being the best soulmate of mine in the Universe.

Propositions accompanying the thesis:

Cosmic particle acceleration by shocks and turbulence  
in merging galaxy clusters

1. The radio-emitting relativistic electrons in radio relics are accelerated by large-scale shocks that are generated during cluster mergers. (Chapter 2, 3, and 5)
2. The efficiency of particle acceleration by low-Mach-number shocks is still poorly known. (Chapter 2 and 3)
3. Radio haloes in merging galaxy clusters are associated with the turbulence that evolves after the passage of merger shocks. (Chapter 2, 4, and 5)
4. Shock compression alone of fossil electrons in the intra-cluster medium (ICM) is not sufficient to generate the observed brightness of extended radio emission in merging clusters of galaxies. (Chapter 4)
5. Double shocks on the opposite sides of the cluster centre may be common in major merging galaxy clusters. (Chapter 2, 3, 4, and 5)
6. High-resolution, multi-frequency observations including polarization measurements will significantly improve our understanding of particle acceleration mechanisms in extended radio emission from clusters of galaxies. (Chapter 4 and 5)
7. To unveil the truth, one needs to look through the object at the correct angle.
8. Re-observing to obtain high quality data is often a better strategy than continuing to work on low-quality data.
9. Multi-wavelength (e.g. radio, optical, X-ray) observations continue to be vital in unveiling the nature of astronomical phenomena.
10. Deeper observations sometimes require more detailed theoretical models to explain discrepancies.
11. “If you want to go fast, go alone. If you want to go far, go together” (African proverb). This is especially true in the present day field of radio astronomy.



12. Coffee breaks are important to generate research ideas.
13. It is mysterious that, despite the tremendous success of science in explaining nature, a large fraction of the world population is still religious.